



Thèse

2021

Open Access

This version of the publication is provided by the author(s) and made available in accordance with the copyright holder(s).

An optical study of the physics of the rare earth nickelates

Ardizzone, Ivan

How to cite

ARDIZZONE, Ivan. An optical study of the physics of the rare earth nickelates. Doctoral Thesis, 2021.
doi: [10.13097/archive-ouverte/unige:154219](https://doi.org/10.13097/archive-ouverte/unige:154219)

This publication URL: <https://archive-ouverte.unige.ch/unige:154219>

Publication DOI: [10.13097/archive-ouverte/unige:154219](https://doi.org/10.13097/archive-ouverte/unige:154219)

An optical study of the physics of the rare earth nickelates

THÈSE

*présentée à la Faculté des Sciences de l'Université de Genève
pour obtenir le grade de docteur ès Sciences, mention Physique*

par

Ivan Ardizzone
de
Chêne-Bourg (Genève)

Thèse n° 5577



**UNIVERSITÉ
DE GENÈVE**

FACULTÉ DES SCIENCES

DOCTORAT ÈS SCIENCES, MENTION PHYSIQUE

Thèse de Monsieur Ivan ARDIZZONE

intitulée :

«An Optical Study of the Physics of the Rare Earth Nickelates»

La Faculté des sciences, sur le préavis de Monsieur D. VAN DER MAREL, professeur ordinaire et directeur de thèse (Département de physique de la matière quantique), Monsieur J.-M. TRISCONE, professeur ordinaire (Département de physique de la matière quantique), Monsieur A. GEORGES, professeur (Département de la Physique de la matière condensée, Collège de France, Paris, France), Madame M. L. MEDARDE, docteure (Department of Physical Properties of Materials, Paul Scherrer Institut, Villigen, Switzerland), autorise l'impression de la présente thèse, sans exprimer d'opinion sur les propositions qui y sont énoncées.

Genève, le 29 juin 2021

Thèse - 5577 -

Le Doyen

"Le temps met tout en
lumière." Thalès

Résumé

Français: La recherche en physique de la matière quantique est basée sur la synthèse et l'étude de matériaux innovants qui ont un potentiel d'application dans l'ingénierie et l'industrie. Parmi ces matériaux, les systèmes aux électrons fortement corrélés dévoilent des comportements électroniques et magnétiques exotiques comme de la multiferroïcité, de la magnétorésistance géante ou colossale, ou encore de la supraconductivité. Cette dernière est au centre de la recherche en physique du solide depuis sa découverte en 1911 par Kamerlingh Onnes. La découverte d'un supraconducteur à température et pression ambiante serait une révolution scientifique.

Dans ma thèse, je m'intéresse aux nickelates de terre rares $RNiO_3$ qui présentent une transition métal-isolant et magnétique due à de fortes corrélations électroniques. Les propriétés structurales, électroniques et magnétiques sont intimement liées. Ainsi, changer la structure cristalline d'un nickelate par substitution de la terre rare, par croissance épitaxiale induisant une contrainte ou par application d'une pression, conduit directement à des changements de sa structure électronique et magnétique. J'étudie ces propriétés par deux différents types de spectroscopie optique: la conductivité optique et la susceptibilité Raman ; deux techniques complémentaires qui ensemble fournissent une description optique complète du matériau.

Le premier chapitre est une introduction générale sur les perovskites, les nickelates et leurs possibles applications.

Dans le deuxième chapitre, je présente une description de toutes les structures cristallines que les nickelates peuvent adopter, de la plus haute symétrie à la plus basse, en spécifiant les éléments de symétrie qui sont brisés pour chaque transition. Je discute ensuite la structure de bandes des nickelates et les corrélations électroniques. Je m'intéresse aussi aux structures magnétiques

et je montre les différents groupes d'espaces possible en fonction de l'ordre antiferromagnétique.

Le troisième chapitre est focalisé sur le nickelate de lanthane (LaNiO_3) qui est le seul nickelate à rester métallique même à basse température. Nous avons étudié les propriétés électroniques de fines couches de LaNiO_3 contrainte compressivement et extensivement par déposition épitaxiale sur des substrats. Je décris en détails les différents instruments qui m'ont permis d'obtenir la conductivité optique des matériaux dans un large intervalle de fréquences ainsi que l'analyse par des modèles de Drude-Lorentz. Nous avons observé une tendance contre-intuitive: une augmentation du poids spectral des charges libres dans le plan pour des contraintes extensives. Cette tendance est capturée par des calculs DFT qui dévoilent également un changement topologique de la surface de Fermi (transition de Lifshitz). La différence systématique entre les calculs et les résultats expérimentaux est due aux corrélations électroniques qui renforce la masse des électrons.

Dans le quatrième et dernier chapitre, je m'intéresse aux plus petites terres rares du diagramme de phase en mesurant par spectroscopie Raman les tout premiers monocristaux de RNiO_3 (avec $\text{R}=\text{La, Nd, Sm, Dy, Ho, Er, Y}$) jamais reportés. Notre installation nous permet de mesurer à basse température et jusqu'à des températures proches du point de fusion des matériaux. En effet, le laser nous permet de chauffer les échantillons et leur température est directement déduite du rapport Stokes/antiStokes du signal. Nous observons lors de la transition métal-isolant une importante diminution du fond électronique ainsi qu'un rétrécissement de tous les phonons et un déplacement vers les hautes fréquences qui met en évidence le fort couplage électron-phonon. En dessous de la température de Néel, nous observons l'apparition du mode mou ainsi que de nouveaux phonons. Ces nouveaux phonons indiquent une brisure de la centrosymétrie et confirme les hypothèses de plusieurs études, qu'une polarisation électrique apparait spontanément dans le matériau, faisant des nickelates des matériaux multiferroïques de type II. Pour compléter cette étude, j'ai appliqué de la pression sur les monocristaux de SmNiO_3 et NdNiO_3 à température ambiante, révélant une transition métal-isolant et une transition orthorhombique-rhomboédrale, respectivement.

English: The research in quantum matter physics is based on the synthesis and on the study of innovative materials which have potential application in engineering and industry. Among these materials, the systems with strong electronic correlations reveal electronic and magnetic exotic behaviours such as multiferroicity, giant or colossal magnetoresistance, and superconductivity. The latter is at the center of solid state physics research since its discovery in 1911 by Kamerlingh Onnes. The discovery of a superconductor at ambient temperature and pressure would be a scientific revolution.

In my thesis, I concentrate on rare earth nickelates RNiO_3 which have metal-insulator and magnetic transition due to strong electronic correlations. Structural, electronic and magnetic properties are deeply related. Therefore, the change of the crystal structure of a nickelate by rare earth substitution, epitaxial strain or pressure, leads to direct changes in the electronic and magnetic properties. I study these properties with two different types of optical spectroscopy: optical conductivity and Raman susceptibility; two complementary techniques which provide a complete optical description of the material.

The first chapter is a general introduction about perovskites, nickelates and their possible applications.

In the second chapter, I present all the crystal structures that nickelates can adopt, from the highest to the lowest symmetry, specifying symmetry elements that are broken at each transition. Then, I discuss the band structure of nickelates and the electronic correlations. I show also the nickelate magnetic structures and the different possible space groups as a function of antiferromagnetic order.

The third chapter is focused on lanthanum nickelate (LaNiO_3) which is the only nickelate to remain metallic even at low temperature. We study the electronic properties of compressive and tensile epitaxial strain LaNiO_3 thin films deposited on various substrates. We describe in detail the different instruments which allow to obtain the optical conductivity of the materials in a wide energy range as well as the Drude-Lorentz models used for the analysis. We observe a counter-intuitive behaviour: an increase of the free carriers spectral weight for tensile strains. This trend is captured by DFT calculations which reveal also a topological change of the Fermi surface (Lifshitz transition). The systematic difference between theoretical and experimental results is due to electronic correlations which reinforce the electrons mass.

In the fourth and last chapter, I concentrate on the smaller rare earth ions by measuring with Raman spectroscopy the first ever reported RNiO_3 single crystals ($\text{R}=\text{La}, \text{Nd}, \text{Sm}, \text{Dy}, \text{Ho}, \text{Er}, \text{Y}$). Our setup allows to measure at low temperature and up to temperature close to the melting point of the material. Indeed, the laser allows to heat the samples and their temperature is directly deduced from the Stokes/antiStokes ratio of the signal. We observe at the metal-insulator transition a huge reduction of the electronic background, as well as a red-shift and a narrowing of all phonons modes which gives evidence of strong electron-phonon coupling of these materials. Below the Neel temperature, we observe the appearance of the soft mode and a large number of new phonons. These new phonons indicate a breaking of the centrosymmetry and confirm the assumption of several studies that an electric polarization appears spontaneously in the material, making the nickelates type-II multiferroics. To complete this study, I applied

pressure on SmNiO_3 and NdNiO_3 single crystals at room temperature and observe a metal-insulator transition and an orthorhombic-rhombohedral phase transition, respectively.

Contents

1	Introduction and motivation	1
2	The physics of rare earth nickelates	7
2.1	The materials: Powders, films, and single crystals	7
2.2	Crystal structure and lattice engineering	10
2.2.1	Tolerance factor, deformation and Glazer notation	10
2.2.2	From high to low symmetry	15
2.3	Electronic structure	32
2.3.1	Band structure	32
2.3.2	Electron-electron correlations	34
2.3.3	Metallic phase of LaNiO_3 thin films and metal-insulator transition of the other nickelates	39
2.4	Antiferromagnetic phase	41
3	Optical properties of LaNiO_3 films tuned from compressive to tensile strain.	51
3.1	Introduction	52
3.2	Optical spectroscopy theory	52
3.2.1	Maxwell equations, dielectric function ϵ and optical conductivity σ	54
3.2.2	General expression for the optical conductivity of a many-body correlated electron system	55
3.2.3	Specific expression for optical conductivity of inter-band transitions	56
3.2.4	Optical selection rules	57
3.2.5	Drude-Lorentz and extended Drude models	58

CONTENTS

3.2.6	Analytical inversion and Kramers-Kronig relations . . .	62
3.2.7	Drude-Lorentz fitting of optical measurements with "Reffit"	63
3.2.8	General expressions of Fresnel equations	65
3.2.9	Fresnel equations of thin film on a substrate	67
3.2.10	Fresnel equations relating thin film ellipsometry to dielectric function ϵ	68
3.3	Experimental methods	69
3.3.1	Samples preparation	69
3.3.2	DC conductivity	70
3.3.3	UHV cryostat	71
3.3.4	Time domain Terahertz transmission	72
3.3.5	Ellipsometry	74
3.3.6	Time domain terahertz ellipsometry	75
3.3.7	Near-infrared/Visible/Ultraviolet light ellipsometry . .	77
3.3.8	Infrared microscope	79
3.4	Strain dependence of the optical conductivity	80
3.5	Spectral weight and mass enhancement	86
3.6	Strain dependence of the electronic structure	88
3.7	Conclusions	94
4	Raman spectroscopic evidence for multiferroicity in rare earth nickelate single crystals	95
4.1	Introduction	96
4.2	Raman spectroscopy	97
4.2.1	Raman process	99
4.2.2	Raman selection rules	100
4.2.3	Geometry of incoming and outgoing light	101
4.2.4	Raman experimental setup	102
4.2.5	Data analysis and methods for controlling and deter- mining the temperature of the sample	104
4.2.6	Sample preparation	106
4.3	Results for the paramagnetic phase	107
4.4	Results for the antiferromagnetic phase	110
4.5	Discussion	114
4.6	Raman measurement at very high temperature or under high pressure	116
4.7	Conclusion	122
	Remerciements	125

CHAPTER 1

Introduction and motivation

Materials with strong electronic correlations have been at the center of research in quantum matter physics since the second half of the 20th century. While the superconductivity of lead was discovered in 1922 without any physical interpretation, Mott, in 1937 was already discussing [1] the likely strong repulsion between electrons in certain metals which may induce a charge localization and therefore a metal-insulator transition upon decreasing temperature. Later, a dramatic drop of the electrical resistivity in the presence of a magnetic field is evidenced in 1950 by Jonker and Van Santen [2] in manganite $\text{La}_{1-x}\text{C}_x\text{MnO}_3$ (with "La" the trivalent lanthanide lanthanum (La) cation and "C" a divalent cation like Ca, Sr or Ba) which is now known as colossal magnetoresistance. Forty years later, Helmolt et al. [3] made great progress in this field and achieved more than 60% of colossal magnetoresistance in thin magnetic films of $\text{La}_{0.67}\text{Ca}_{0.33}\text{MnO}_3$. At the same time, giant magnetoresistance (GMR) was discovered by two different research groups (groups of A. Fert and P. Grunberg) in thin-film superlattices of iron and non-magnetic Chromium [4, 5] which earned them the Nobel Prize in 2007. GMR is now widely used for hard disk drives and magnetic RAM. The comprehension of these exotic phenomena remains a major challenge until today.

All of these remarkable properties can be found in the members of the perovskite family, making them very relevant for current technologies. Initially, the term perovskite designated only the mineral calcium titanate (CaTiO_3) discovered in 1839 by Gustav Rose in the hercynian mountain range, the

1. Introduction and motivation

ourals. The denomination "perovskite structure", or simply "perovskite", is by now extended to describe the crystal structure of all ABO_3 type oxides with a "A" cation commonly an alkali metal, an alkali earth metal, or a rare earth lanthanoid and a "B" cation a post-transition metal or more commonly a transition metal. The B cation is surrounded by six oxygen atoms O forming an octahedron and the A cation seats at the center of eight octahedra. The final compound belongs to the family of transition metal oxides (TMOs) [6]. While cuprates are considered as the "unconventional superconductor", perovskite structures have much wider applications and are the subject of intensive research in quantum matter physics.

In recent years, research has particularly focused on the field of battery engineering, cancer therapy (using harmonic nanoparticles and pulsed laser irradiation), and photovoltaic cells [7–9]. The latter is currently at the center of the international political debates and may provide a potential answer to the energy crisis and global warming. The first solar cell was manufactured 130 years ago by Charles Fritts with an efficiency of around 1% [10]. From that point, increasing cell efficiency was the main motivation for scientists and now ranges between 14 and 25% depending on the material and its monocrystalline or polycrystalline nature [11–15]. Halide perovskites are good candidates for the next generation of solar cells due to their low cost, high absorption coefficients and easy manufacturing [16]. Perovskite-silicon tandem solar cells show for the moment the higher performance with efficiency up to 27.7% [17]. The new report of "ReTHINK Energy"[18] envisages that perovskite solar cells have the potential to reduce the traditional solar generation costs by 50% and constitute 29% of the global energy market by 2030. Fundamental research on these kind of materials thus remains an important task.

Perovskite rare earth nickelates are good candidates for these applications and open new horizons to design novel photovoltaic materials. Indeed, oxygen vacancies introduced in $NdNiO_3$ thin film of $Au/NdNiO_3/Nb:SrTiO_3$ heterojunctions shown increase of photovoltaic performance due to the adjustment of the bandgap and suggest that nickelate films have a possible application in photovoltaic cells with $NdNiO_3$ playing the role of the p-type semiconductor [19]. Moreover, lanthanum nickelate $LaNiO_3$ was introduced into a polymer solar cell (PSC) device, replacing the polymer mixture PEDOT:PSS hole transport layer, and reveals improvement of stability, charge transport and power conversion efficiency [20]. A recent study shows that the photovoltaic performance of nickelate heterostructures can also be tuned by changing the A-site rare earth element [21]. Harnessing and controlling these effects offer new opportunities to face future environmental difficulties. Moreover, compared to other perovskites, layered nickelates,

including Ruddlesden-Popper type layered nickelates, have high chemical stability, mechanical compatibility, improved oxygen transport, and hydration ability, making them excellent cathode materials for solid oxide fuel cells (SOFC) [22–25]. The range of nickelate applications is even wider, for example in electronics with thermoelectric thermistor temperature reading [26], high frequency giant dielectric constant materials [27] as well as novel electronic and iontronic devices [28] where they even may replace silicon [29]. The low-cost manufacture of nickelates [30–32] together with all the rich exotic behaviours and large possible applications make perovskite nickelates very interesting materials for research and engineering. Unlike their name, the abundance of rare earth elements [33, 34] on the Earth’s crust is almost similar to copper. However, their extraction remains a central problem due to the chemical products used to sort them which produce highly toxic and radioactive thorium, titanium and zirconium as well as hydrofluoric acid fume.

In general, nickelate compounds show paramagnetic metallic behaviour at high temperature and an antiferromagnetic insulating phase at low temperature due to electronic correlations. Their physical properties such as lattice structure, structural deformation and charge disproportionation at the metal-insulator transition were already observed several decades ago on powders or ceramics by X-ray diffraction [35–41], while neutron diffraction measurements revealed the antiferromagnetic spin density wave of these materials [42–44] which was unprecedented in a perovskite structure. In general, magnetism rarely occurs in the same phase with ferroelectricity. Indeed, in 2000, Hill discussed these rare compounds, known as multiferroic materials, in his article ”Why are there so few magnetic ferroelectrics?”[45]. However, many studies based on calculations predict multiferroicity in rare earth nickelates [46–53]. This topic is by the way a new surge of interest in quantum matter physics for their application to control magnetism by electric field or high-sensitivity ac magnetic field sensors.

Key advances have been made over the past 20 years through lattice and strain engineering in nickelate thin films and heterostructures which allow to tune their physical properties such as the metal-insulator transition by biaxial epitaxial strain [54–71], oxygen off-stoichiometry [72–74] or rare earth substitution [6, 75]. The latter allowed to reveal superconductivity in infinite-layer samples of $\text{Nd}_{0.8}\text{Sr}_{0.2}\text{NiO}_2$ [76, 77] below $T_c = 14\text{K}$ which suggests that a family of nickelates is a potential superconductor analogous to copper oxides or pnictides. Moreover, theoretical studies on thin-film $\text{LaNiO}_3/\text{LaAlO}_3$ heterostructure and $\text{LaNiO}_3/\text{LaMO}_3$ superlattices (with M a trivalent cation such as Al, Ga or Ti) show similar orbital configurations than cuprate superconductors which suggest for both favorable conditions

1. Introduction and motivation

to host high- T_c superconductivity [78, 79]. Single crystal measurements remain however the best access to probe directly the structural, electronic and magnetic properties of bulk materials. Nickelates were almost impossible to grow as single crystals up to less than 10 years ago [80, 81]. However, thanks to technological progress and collaboration with Paul Scherrer institut, I am fortunate to show the optical results of the very first RNiO₃ single crystals reported with R covering (almost) the full 4f series.

In this thesis, I report the evolution of the lattice, electronic and magnetic structure of nickelates along all the series using various optical spectroscopy techniques on thin films and unique single crystals as a function of temperature. The work is divided in three main parts:

- A chapter presenting the physics of rare earth nickelates, which includes a discussion of the samples (powders, films, and single crystals), the crystal structures from the highest to the lowest symmetry present in the phase diagram of nickelates, the electronic structure through density functional theory (DFT) and electronic correlations, the different probable magnetic orders below the Neel temperature and finally the properties of the metallic phase.
- A study of the optical properties of LaNiO₃ films tuned from compressive to tensile strain, which shows the evolution of free carrier spectral weight and mass enhancement as a function of epitaxial strain. A general introduction on optical spectroscopy and descriptions of different optical measurement techniques are presented.
- A study of the Raman spectroscopic evidence for multiferroicity in rare earth nickelate single crystals, which shows the change of the phonons in the Raman spectra as a function of temperature and the appearance of new optical modes below the Neel temperature for RNiO₃ with R=Y, Er, Ho, Dy, Sm and Nd. We show also the impact of pressure on SmNiO₃ and NdNiO₃ single crystals. Raman spectroscopy technique is discussed in detail.

Part of the work described in this thesis has been published in scientific journals: "I.Ardizzone et al, Physical Review B 102, 155148 (2020)" [82], and "I.Ardizzone et al, Physical Review Research 3, 033007 (2021)" [83].

Concerning the chapter on "optical properties of LaNiO₃ films tuned from compressive to tensile strain", we thank a lot Jean-Marc Triscone's group and especially Marta Gibert and Jennifer Fowlie who prepared five epitaxial strained LaNiO₃ thin films with very high qualities. They measured also the Direct Current (DC) conductivity of the films which were used in

the Drude-Lorentz analysis procedure and characterized the lattice structure properties by X-ray diffraction. To support our observations, theoretical calculations were used to compute the optical response of thin LaNiO_3 film as a function of epitaxial strain. These calculations were done by the group of Antoine Georges composed of Manuel Zingl, Hugo Strand, Oleg Peil, Alexandru Georgescu and Antoine Georges himself who used Density functional Theory (DFT) to deduce the electronic properties such as evolution of band structure and then the optical properties from high compressive to moderate tensile strain. The calculated orbital hybridization of the $2p$ oxygen and $3d$ bands (which change considerably as a function of strain due to the competition between Ni-O bond lengths and oxygen octaetra rotation) allowed to understand the counter intuitive increase of free carrier spectral weight for tensile strain observed experimentally. The calculations show also a significant reconstruction of the Fermi surface which is discussed in the corresponding chapter. We warmly thank this great collaboration and the excellent work of Antoine Georges team to theoretically characterized the strain dependence of these films.

Concerning the chapter "Raman spectroscopic evidence for multiferroicity in rare earth nickelate", our big thanks goes out to Marisa Medarde and Dariusz Gawryluk from Paul Scherrer Institut (PSI) who grown the first and unique nickelate single crystals with very high quality which allowed to demonstrate the inversion symmetry breaking of nickelates below the Neel temperature and therefore supports the possible existence of multiferroicity of these compounds.

The physics of rare earth nickelates

2.1 The materials: Powders, films, and single crystals

Probing physical properties of materials requires not only the suitable instruments, but also high quality samples of adequate size of the compound under investigation. Optical spectroscopy and diffraction measurements are performed on three main types of samples: Powders, single crystals and films. The advantages and disadvantages of using each of these three different crystalline forms will be discussed in this section.

Powder samples consist of a large number of randomly oriented crystallites of the same composition and can be compacted to obtain samples of the size necessary for a given instrument. Heavily compressed and sintered powders are a particular crystalline form called ceramics. They have been used for over a century and, for example in 1950, Goetzel was already writing about them his second volume encyclopedia of "Treatise on powder metallurgy". A particular advantage of ceramics compared to single crystals is that almost every material can be synthesized in this form. Hugo Rietveld, who created the Rietveld refinement method in 1967 [84] (an analysis technique for neutron and X-ray diffraction of powder samples), mentioned that "The powder method has gained a new importance in neutron diffraction owing to the general lack of large specimens for single-crystal methods". While large crystals can be found in nature for some compounds such as

2. The physics of rare earth nickelates

quartz SiO_2 , they often contain a lot of impurities. On the other hand many materials of interest are very difficult or even impossible to grow with high crystalline quality and reasonable size in a laboratory. This was the case for nickelates less than 10 years ago where, with the exception of NdNiO_3 for which crystals of 50-100 microns were grown [81], the typical size of a nickelate microcrystal was on the order of 3 microns ($\text{DyNiO}_3 \sim 3 \mu\text{m}$ [85]).

The first RNiO_3 powders (with $\text{R}=\text{Lu}, \text{Y}, \text{Er}, \text{Ho}, \text{Dy}, \text{Gd}, \text{Eu}, \text{Sm}, \text{Nd}, \text{La}, \text{Tm}, \text{Yb}$) were synthesized by Demazeau in 1971 [35] and allowed him to deduce the rhombohedral structure with space group $R\bar{3}C$ of LaNiO_3 and the orthorhombic $Pbnm$ structure for the rest of the series with X-ray diffraction measurements. In the last 50 years, powders, but primarily ceramics, allowed the physical properties of nickelates to be probed. X-ray and neutron diffraction measurements confirmed several times the structure of the high temperature metallic phase mentioned above, and later revealed the small monoclinic distortion with space group $P2_1/c$ of the insulating phase [37–39, 41, 86]. Many more reports followed, revealing, for example, the anomaly of the unit cell volume and of the cell parameters at the metal-insulator transition [36, 39], the decrease of the Ni-O-Ni γ angle for smaller rare earth elements [38, 44], as well as the checkboard configuration of short and long Ni-O bonds (called bond disproportionation or breathing distortion) that appears in the insulating phase [38–41, 86]. These properties will be discussed in the following sections. The first order phase transition of NdNiO_3 and PrNiO_3 was demonstrated by the comparison between the electrical resistivity measurements on powders during warming up and cooling down, which revealed a hysteretic behaviour [44, 87–90]. The Seebeck coefficient shows similar hysteresis curves for these two nickelates and reveals electron-like particles as charge carriers [44]. The absence of a hysteretic behaviour for the other compounds suggests a second order metal-insulator transition [91, 92]. The magnetic structure was also probed on powders by polarized neutron diffraction, revealing the low spin nickel state as well as unusual $\uparrow\uparrow\downarrow$ antiferromagnetic order with a propagation vector $(1/4, 1/4, 1/4)_{pc}$ in the pseudocubic representation [42–44]. Three neighbouring nickel sites are indeed coupled ferromagnetically while three other nickel sites are coupled antiferromagnetically. Susceptibility measurements show a magnetic moment of about $0.9 \mu_B$ for PrNiO_3 , NdNiO_3 and SmNiO_3 [42, 44].

The availability of powders has therefore made it possible to probe the structural, electrical and magnetic properties of nickelates as described above, but they are not entirely suitable for certain analyses, especially optical measurements. While it is possible to do reflectivity, transmittivity or ellipsometry measurements on powders [86, 93, 94], it was noticed that a low ceramic density may cause changes in the reflective and scattering signals,

2.1 The materials: Powders, films, and single crystals

some relevant edge effects are observable [95] and the penetration length of the incident light depends on the grains volume. To avoid these issues, it is more convenient to use only larger single crystals for such measurement. Powders can either be amorphous, but they can also consist of many tiny single crystals which could be measured one by one if their size is large enough. However, if the size of the crystal is of the order of a micrometer, the measurement is impossible.

For crystals with an area of around $100\text{-}200\ \mu\text{m}^2$, Raman scattering microscope measurements can be performed as well as usual X-ray. Single crystal measurements are the best way to directly probe the structural, electronic and magnetic properties of bulk materials. Indeed, no perturbation such as strain which may modify the intrinsic properties of the sample, is expected in this case. It is also possible to adjust the orientation of the crystal in order to probe the three different crystallographic axis. The latter is impossible with powders due to the random orientation of each single crystalline grain. External perturbations such as temperature or pressure can also be applied to single crystals.

Measurements on large-sized single crystals give precious information about the lattice structure (X-ray diffraction) and collective excitations (Raman scattering and neutron spectroscopies) but the optical measurements are very restricted. Indeed, even with a microscope, it is impossible to perform far-field infrared or visible reflectivity measurements (below $10\ \mu\text{m}$) due to the diffraction limit. To perform optical measurements, samples larger than micrometer-sized single crystals are required. Sufficiently large crystals cannot be produced by the usual high pressure powder method. In 1958, Jan Anthony Lely patented a new crystal growth process and manufactured silicon carbide (SiC) crystals by sublimation. This was the starting point of a new crystal format called epitaxial films, which are now grown by chemical vapour deposition or physical vapour deposition. The latter consists of three different techniques: Pulsed laser deposition, molecular beam epitaxy and sputtering [6], which are widely used to grow perovskite oxides. These films are simply single crystals grown on single crystal substrates whose orientation and size can be controlled by varying the orientation and diameter of the substrate. Nickelates in thin film form are very convenient for Direct Current (DC) conductivity, spectroscopic ellipsometry, reflectivity, transmittivity, Raman scattering or even Scanning Near-Field optical microscope (SNOM) measurements. The thickness of the sample varies from a few unit cells to several nanometers. The main differences compared to single crystals is the quasi two-dimensionality of the sample and the biaxial epitaxial strain induced by the substrate. This latter property can be taken advantage of to probe the evolution of the lattice and

2. The physics of rare earth nickelates

the electronic structure as a function of both compressive and tensile strain, by tuning the lattice mismatch between the substrate and the film material. The downside is that 0% of strain is never exactly achieved and the lattice mismatch between thin film and substrate induces a natural expansion or contraction of the lattice parameters in the three crystallographic directions. Deformations of the internal structure appear to accommodate the strain, resulting in a different crystal symmetry compared to bulk crystals [6, 58, 66]. Thickness may have a huge impact on the electronic properties too [6]. Many studies [55, 57, 58, 61, 63, 64, 67, 96] have demonstrated the impact of biaxial epitaxial strain on the lattice and electronic properties of nickelate thin films. For example, oxygen octahedra rotation and Ni-O bond lengths evolve considerably, and in extreme cases, being the main parameters of the orbital overlap and therefore may induce a metal-insulator transition. The complex mechanisms of these crystal structure adjustments are developed in the following sections. Reduction of the film thickness improves the insulating state while the metallicity is reinforced for oxygen off-stoichiometry [6, 63, 65, 69, 72, 74, 97]. All these parameters have to be taken into account in the interpretation of the experimental results and the growth of high quality thin films is therefore the main challenge in disentangling the change in electrical properties due to lattice distortion rather than unexpected effects.

2.2 Crystal structure and lattice engineering

2.2.1 Tolerance factor, deformation and Glazer notation

The highest symmetric ABO_3 perovskite crystal structure is cubic. Decreasing the size of the A cation induces a tilting of the BO_6 octahedra to fill the extra interstices and reduce the unit cell volume inducing a distortion of the cubic structure. The metal-insulator temperatures T_{MI} and the magnetic transition Neel temperature T_N of nickelates, depend on this deformation which is quantified by the Goldschmidt tolerance factor t defined:

$$t = \frac{(r_{RE} + r_O)}{\sqrt{2}(r_{Ni} + r_O)} \quad (2.1)$$

where r_{RE} , r_{Ni} and r_O are the ionic radii of the rare earth, the nickel and the oxygen atoms, respectively. The tolerance factor t , Ni-O-Ni γ angle, as well as metal-insulator transition temperature T_{MI} and Neel temperature T_N [47] for nickelates from R=lanthanum (La) to Lutetium (Lu) including the solid solution $Sm_{1/2}Nd_{1/2}NiO_3$ are summarized in table 2.1 and figure 2.1. Table 2.1 shows that a decrease of the tolerance factor t means a reduction of the Ni-O-Ni γ angle, an increase of the deformation of the structure and a stronger stability of the insulating phase (Fig. 2.1).

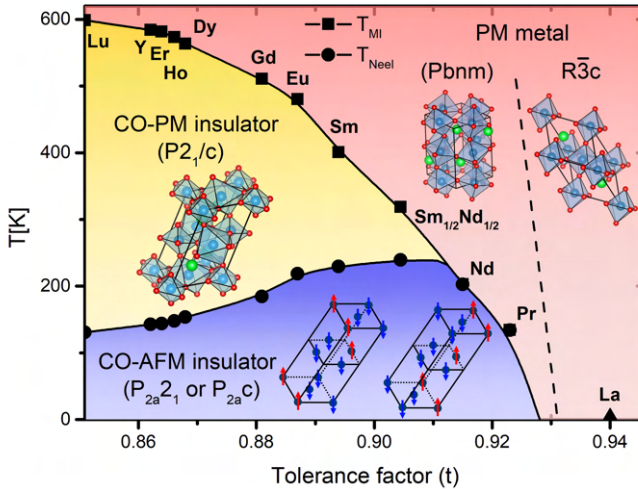


Figure 2.1: Phase diagram of Rare-Earth nickelates RNiO₃. Tolerance factor (t), which indicates the deformation of the structure, as a function of temperature T . At high temperatures, nickelates are paramagnetic metals indicated by red shading with rhombohedral $R\bar{3}c$ crystal symmetry for R=La and orthorhombic $Pbnm$ crystal symmetry for the rest of the family. For R=Sm to Lu, the nickelates have a paramagnetic insulator phase indicated by yellow shading and characterized by a lowering of the symmetry to $P2_1/c$. At low temperatures, nickelates become antiferromagnetic, illustrated by blue shading. Here, theoretical prediction together with our Raman measurements suggest a lowering of the crystal symmetry to $P_{2a}2_1$ or $P_{2a}c$ space groups.

The phase diagram can be separated into four main parts:

- The ideal cubic perovskite structure, which would correspond to a Ni-O-Ni angle of 180° has $t=1$.
- The least distorted member of the rare earth nickelates family is LaNiO₃. The lanthanum (La) rare earth nickelate gives $t=0.94$, has $\gamma=165.2^\circ$, and has a rhombohedral crystal structure $R\bar{3}c$ space group. It remains a paramagnetic metal even at low temperature. Indeed, the deformation is insufficient to induce an insulating phase due to the strong overlap of the $3d$ nickel and $2p$ oxygen orbitals.
- Praseodymium (Pr) and neodymium (Nd) rare earth nickelates have $t=0.925$ ($\gamma=158.7^\circ$) and $t=0.915$ ($\gamma=157.2^\circ$), respectively. PrNiO₃ and NdNiO₃ are both paramagnetic metals at high temperature with an orthorhombic crystal symmetry ($Pbnm$) and become antiferromagnetic insulators below 131 K and 202 K, respectively. Note that the metal-insulator temperature T_{MI} and the Neel temperature T_N coincide for

2. The physics of rare earth nickelates

both compounds. It has been reported that the crystal structure adopts a monoclinic $P2_1/c$ (or $P2_1/n$ which is an alternative setting of the same structure and is closer to $Pbnm$) distortion in the insulating phase [37–39, 41, 86]. However, as will be shown in chapter 4 our Raman measurements rather suggest a lowering of the crystal symmetry to $P2_a2_1$ or $P2_ac$ space groups, in agreement with group theory arguments.

- All other members of the family from samarium (Sm) to the smallest rare earth lutetium (Lu) lie in the range $0.894 (\gamma=152.6^\circ) < t < 0.851 (\gamma=143.4^\circ)$. They are paramagnetic metals at high temperature and share the orthorhombic $Pbnm$ structure of PrNiO_3 and NdNiO_3 . They undergo a metal-insulator transition below T_{MI} with a monoclinic $P2_1/c$ distortion and remain paramagnetic until the antiferromagnetic transition at the Neel temperature $T_N < T_{MI}$.

External or internal perturbations such as epitaxial strain, pressure, or rare earth substitution cause deformation of the structure and affect the electronic or magnetic properties of nickelates. As we mentioned in the last section, epitaxial strain has a dramatic impact on the electronic properties of nickelates. Many studies report a decrease of the metal-insulator transition temperature in NdNiO_3 thin films compared to the value observed in bulk measurement on powders and single crystals, for both compressive (negative) and tensile (positive) strain. Some reports even demonstrate a vanishing of the low temperature insulating phase for compressive strain with NdNiO_3 grown on YAlO_3 (-3.1%), on NdAlO_3 (-1.3%) and even on LaAlO_3 (-0.5%) [55, 57, 58, 63, 64, 98]. The c axis parameter increases while the a and b axis parameters as well as the Ni-O-Ni γ rotation angle decrease from tensile to compressive strains [58, 61, 96]. This competition between Ni-O bonds lengths and octahedral rotation leads to a complex and non-intuitive hybridization of orbitals [58, 96]. These results suggest that compressive strain promotes orbital overlap and broadens the d -band thereby favouring metallicity. Note also that tensile strain broadens the metal insulator transition in NdNiO_3 [57, 58, 63]. Similar behaviour was observed for SmNiO_3 thin films [67], but it is not the case for all the nickelates. Indeed, in our own experiments which will be presented in the chapter 3, we observe the opposite trend for LaNiO_3 thin films. Our experimental observations are further supported by DFT calculations. Fowlie [6] argues in her thesis that this metallic behaviour, even at low temperature for compressively strained NdNiO_3 thin films, can be caused by oxygen off-stoichiometry. Indeed, nickelates are highly sensitive to the oxygen concentration and their resistivity can be tuned in this manner [69, 72, 74, 97]. Dimensionality also has an important impact on the electronic properties and several studies have shown that reducing the thickness of nickelate films favors the insulating phase [6, 63, 65]. In the case of LaNiO_3 , Fowlie et al. show that the evolution

2.2 Crystal structure and lattice engineering

Nickelates	Tolerance factor t	Ni-O-Ni β angle (degrees)	T_{MI} (K)	T_N (K)
LaNiO ₃	0.94	162.5		
PrNiO ₃	0.925	158.7	136.7	136.7
NdNiO ₃	0.915	157.0	203.0	203.0
Sm _{1/2} Nd _{1/2} NiO ₃	0.905	153.8	321.0	240.8
SmNiO ₃	0.894	152.6	403.0	230.8
EuNiO ₃	0.887	151.6	482.1	220.8
GdNiO ₃	0.881	150.6	511.6	185.4
DyNiO ₃	0.868	147.8	566.5	154.1
HoNiO ₃	0.866	147.4	574.0	148.4
ErNiO ₃	0.864	147.3	583.3	145.5
YNiO ₃	0.862	146.7	584.7	144.1
LuNiO ₃	0.851	143.4	600.1	131.2

Table 2.1: Tolerance factor t , Ni-O-Ni in-plane γ angle, metal-insulator transition temperature T_{MI} (K) and Neel temperature T_N (K) for rare earth nickelates with R = La, Pr, Nd, $Sm_{1/2}Nd_{1/2}$, Sm, Eu, Gd, Dy, Ho, Er, Y, Lu. [47]

of the conductivity is due to three distinct types of local structure [68]. There are several propositions for the origin of the stabilization of the insulating phase in thin films. On one hand it may be caused by surface polar distortions coupled with octahedral rotations, which in turn decrease the Ni-O-Ni γ angle. On the other hand, dimensional crossover may play a role [65, 99, 100]. In both situations, the reduction of the bandwidth W induces the increase of T_{MI} .

Applying pressure is another way to induce structural and therefore electronic change in these materials. Unlike biaxial strain which is strongly anisotropic, hydrostatic pressure induces a uniform stress along the three crystallographic directions. For example, several studies show a pressure-induced metal-insulator transition at room temperature on powders of SmNiO₃, EuNiO₃ and YNiO₃ at about 2.5, 6 and 14 GPa, respectively [92, 101–106]. The metallic behaviour is explained by a gradual increase of the electronic bandwidth with increasing pressure and is accompanied by the $P2_1/c$ to $Pbnm$ structural transition. For PrNiO₃ and NdNiO₃, a decrease of the metal-insulator temperature T_{MI} and even a complete suppression of the metal-insulator transition ($T_{MI} \rightarrow 0$) were observed at high pressure [91, 107–110]. It was also observed that pressure induces orthorhombic-rhombohedral phase coexistence followed by a pure rhombohedral $R\bar{3}c$ phase for pressures above 4 GPa for PrNiO₃ [107, 111] and

2. The physics of rare earth nickelates

NdNiO₃ [112] and above 30 GPa for SmNiO₃ [105].

Finally rare earth substitution also permits tuning of the metal insulator transition by inducing structural deformations. In her thesis, Fowlie presents DC transport and Raman spectroscopy studies [6] on thin films of the mixture Nd_{1-x}La_xNiO₃ which reveal the decrease of the metal-insulator temperature T_{MI} with the increase of x and the complete suppression of the metal-insulator transition for $x > 0.2$. She explains that a structural crossover between the $Pnma$ (orthorhombic for $x=0$, NdNiO₃) and $R\bar{3}c$ (rhombohedral for $x=1$, LaNiO₃) space groups takes place. More precisely, between $Pnma$ and $C2/c$ because LaNiO₃ adopts a monoclinic deformation with $C2/c$ space group under biaxial strain, which is a subgroup of $R\bar{3}c$. Raman measurements at room temperature do not show any phase coexistence, implying total samples homogeneity without any phase segregation and a rather gradual parameter evolution from the orthorhombic to the monoclinic structure as a function of the x composition parameter. She argues that a structural transition occurs for $x = 0.35$ and can be driven by the allowed intermediate orthorhombic structure of space group $Imma$. She finally supposes that all compositions with $x > 0.2$ are blocked in a metastable $C2/c$ structure and bond disproportionation cannot occur, and thus it remains metallic.

To describe the deformation of the lattice and more precisely the rotation and tilt of the octahedra, it is useful to adopt the Glazer notation. The octahedra inclination can be decomposed by their rotation around the three crystallographic axis a , b and c with the corresponding rotations α , β and γ respectively (Fig.2.2a). A letter is repeated if the rotations are equal in magnitude for more than one axis. The octahedra rotate either in-phase (octahedra rotate in the same direction from layer to layer along the given rotation axis a , b or c) which is marked by a " + " sign exponent on the top of the letter, or out-of-phase (octahedra rotate in opposite direction from layer to layer along the given rotation axis) which is marked by a " - " sign exponent. If there is no rotation the exponent is "0". The simplest example is illustrated by the octahedra in figure 2.2b which do not undergo any rotation ($a^0a^0a^0$). While an octahedron on the top layer of figure 2.2c rotates around the three crystallographic axis with the same magnitude, the corner sharing octahedron on the bottom layer rotates in opposite directions around a , b and c . The Glazer notation is therefore $a^-a^-a^-$. In figure 2.2d, the top layer octahedron rotates around the three crystallographic axis, however, while the corner sharing octahedron on bottom layer rotates in opposite direction around a and b , it rotates in phase (and with different magnitude) along c . The Glazer notation is $a^-a^-c^+$.

Of course, the rotation of one octahedron induces opposite rotation of the four adjacent octahedra in the same layer.

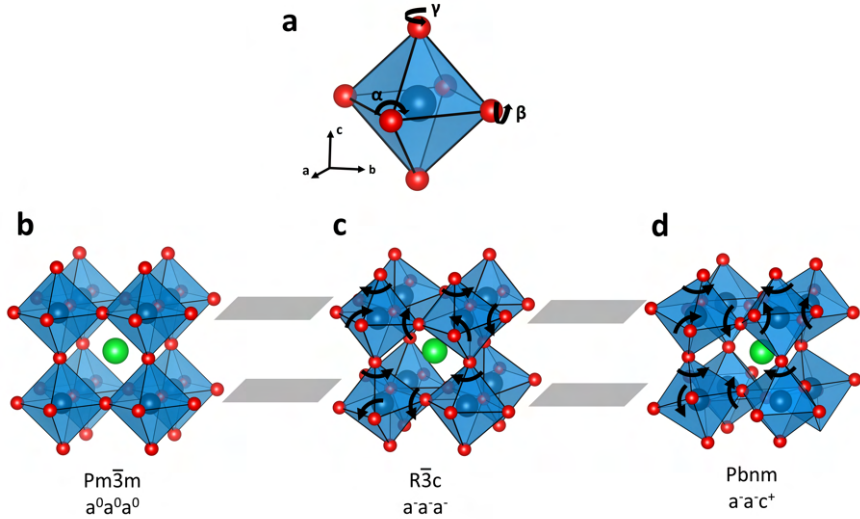


Figure 2.2: Schematic view of the octahedral rotation. **a**, Characteristic octahedron and illustration of the tilt axis. **b**, Illustration of $a^0 a^0 a^0$ Glazer notation. The octahedra undergo no rotation. **c**, Illustration of $a^- a^- a^-$ Glazer notation. While a top layer octahedron rotates with the same magnitude around the three crystallographic axis, the corner sharing bottom layer octahedron rotates in opposite directions around the three axes. **d**, Illustration of $a^- a^- c^+$ Glazer notation. While a top layer octahedron rotates around the three crystallographic axis (around a and b with the same magnitude), the corner sharing bottom layer octahedron rotates in opposite directions around a and b and in phase around c .

2.2.2 From high to low symmetry

To study the impact of the structural deformation on the magnetic and electronic properties, it is essential to know in detail all the crystal structures that nickelates can adopt across the phase diagram as well as the relation between them. This section presents all the possible nickelate crystal structures, from the highest to the lowest symmetry, specifying symmetry elements that are broken at each transition. Possible magnetic space groups are also discussed. Table 2.2 summarizes the possible symmetry operations of the magnetic and non-magnetic space groups presented in this section as defined in Ref [113]. The group elements indicated in the Hermann Mauguin notation are the generators of the group. Inversion is in many cases generated

2. The physics of rare earth nickelates

by two or more generators and for that reason usually not itself indicated as a generator.

Symmetry operation	symbol	Description
η -fold rotation	" η " (a number)	" η " order counter-clock rotation around an axis (for example 4 order = 90°).
η -fold inversion rotation	$\bar{\eta}$	" η " order counter-clock rotation around an axis followed by an inversion symmetry through the center of the structure.
Mirror plane reflection	m	Mirror reflection through a plane.
c -glide plane	c	Reflection through a plane followed by a translation of $c/2$ along axis \mathbf{c} . In this example, the axis is \mathbf{c} but could be axis \mathbf{a} or \mathbf{b} .
n -glide plane	n	Reflection through a plane followed by a translation of half the diagonal $(a+c)/2$ along $\mathbf{n} = \mathbf{a} + \mathbf{c}$ or $(a+b+c)/2$ along $\mathbf{n} = \mathbf{a} + \mathbf{b} + \mathbf{c}$.
2_1 screw axis	2_1	Second order rotation (180°) around an axis followed by a translation of $b/2$ along \mathbf{b} . \mathbf{b} is defined here as the unique axis.
Parallel to	/	Symbol indicating that the preceding and following element have the same axis.
Time reversal symmetry	'	Symbol indicating that the transformation respects the time reversal symmetry.

Table 2.2: Summary of symmetry operations under which the structure is invariant used in this section.

Cubic $Pm\bar{3}m$

We start with the highest crystal symmetry, the cubic structure with space group $Pm\bar{3}m1'$, a so-called supergroup. Strontium titanate SrTiO_3 , which is a famous wide-gap semiconductor, adopts this $Pm\bar{3}m1'$ cubic structure at room temperature and reveals quantum paraelectricity [114]. LaNiO_3 and PrNiO_3 get closer to the cubic crystal structure at very high temperature (up to thousand degrees) but there is for the moment no experimental observation of this transition [44, 115].

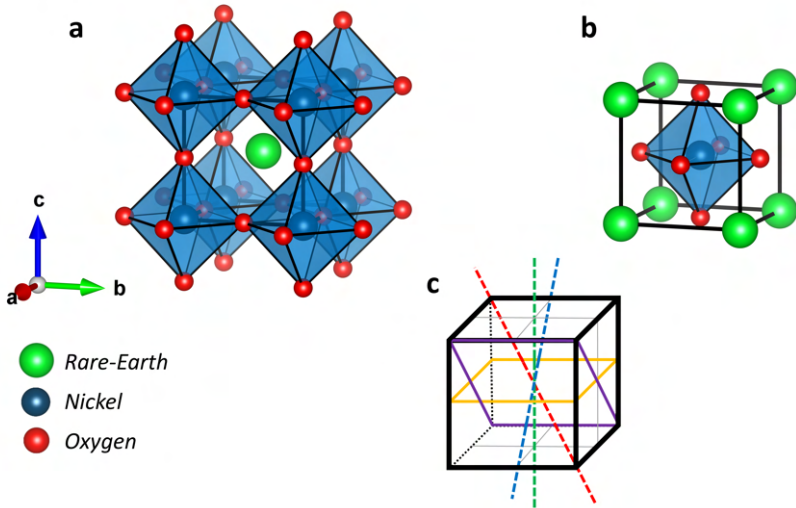


Figure 2.3: Cubic $Pm\bar{3}m1'$ crystal structure. Green, blue and red balls are rare earth, nickel and oxygen atoms, respectively. The three crystallographic axis lengths are equivalent and orthogonal to each other. The octahedra do not undergo any rotation ($a^0a^0a^0$). **a**, Representation of $Pm\bar{3}m1'$ crystal structure centred on the rare earth ion **b**, Primitive unit cell $Pm\bar{3}m1'$ centred on the nickel ion equivalent to pseudocubic representation. Only one formula unit is required to describe the primitive unit cell. **c**, Symmetries of the $Pm\bar{3}m = P4/m\bar{3}2/m$ crystal structure. $4/m$ = four order rotation (4-fold = 90°) around the dash green axis $[0,0,1]$ and symmetry mirror perpendicular to this axis delimited by orange line. $\bar{3}$ = three order rotation (3-fold = 120°) around the dash red axis $[1,1,1]$ followed by an inversion symmetry through the center of the cube. $2/m$ = Two order rotation (2-fold = 180°) around the dash blue axis $[0,1,1]$ and symmetry mirror perpendicular to $[1,1,0]$ delimited by purple line.

The $Pm\bar{3}m1'$ cubic structure is shown in figure 2.3 with the oxygen, nickel and rare earth atoms illustrated by red, blue and green spheres respectively. Figure 2.3a illustrates the crystal structure representation centred on the rare earth ion with eight oxygen octahedra surrounding the nickel atoms

2. The physics of rare earth nickelates

while figure 2.3b represents the primitive unit cell centred on the nickel ion and composed of only one octahedron. Only one formula unit is required to describe the primitive unit cell. The cubic structure has no octahedral rotation as shown in figure 2.3a. The Glazer notation is therefore $a^0a^0a^0$ and the Ni-O-Ni γ angle, which describes the angle between two nickel sites, is 180° . The equal length of the primitive cell axes ensures an equal distance between all nickel and oxygen sites, meaning equal Ni-O bond lengths, in all three crystallographic directions (Fig. 2.3b). Table 2.3 summarizes the notation $Pm\bar{3}m1'$ which is explicitly $P4/m\bar{3}2/m1'$.

P	primitive
$4/m$	4-fold rotation (90°) around the dash green axis $[0,0,1]$ in Fig. 2.3c and mirror reflection m through a plane delimited by orange line perpendicular to the previous axis.
$\bar{3}$	Rotation of order 3 (120°) around an axis (dash red axis $[1,1,-1]$) followed by inversion symmetry through the center of the cube.
$2/m$	2-fold rotation (180°) around an axis (dash blue axis $[1,0,-1]$) and planar reflection m through the plane perpendicular to the previous axis (delimited by purple line).
$1'$	Time reversal symmetry.

Table 2.3: Summary of $Pm\bar{3}m1'$ (explicitly $P4/m\bar{3}2/m1'$) space group notation.

Implicitly present, but usually not explicitly indicated, the three trivial translations T_a , T_b and T_c along \mathbf{a} , \mathbf{b} , and \mathbf{c} crystallographic axis respectively as well as $\bar{1}$ center inversion symmetry are among the symmetry operations.

The following subsections present the structures resulting from distortions of highly symmetric $Pm\bar{3}m1'$ space group. To compare similarities and differences of various distorted structures, it is useful to introduce the pseudocubic unit cell which is an alternative representation of the same structure, but with the unit cell centred on one nickel site.

The pseudocubic representation is convenient for comparing octahedra rotation or axis parameters \mathbf{a}_{pc} , \mathbf{b}_{pc} and \mathbf{c}_{pc} (\mathbf{a} , \mathbf{b} and \mathbf{c} axis respectively in the pseudocubic representation). For example, the primitive unit cell of $Pm\bar{3}m1'$ (Fig.2.3b) is its own pseudocubic representation. As another example, the construction of the pseudocubic axis (a_{pc} , b_{pc} , c_{pc}) from the orthorhombic unit cell coordinates (a_0 , b_0 , c_0) is shown in figure 2.4a and involves a 45° rotation of the ab plane. The usual pseudocubic unit cell is depicted in figure 2.4b, and is composed of only one octahedron. The transformation from orthorhombic to pseudocubic axis is fairly well approximated by [116]:

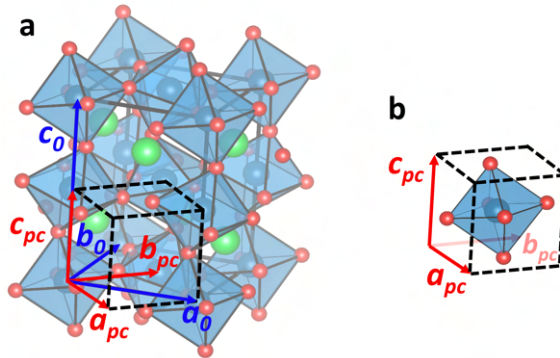


Figure 2.4: $Pbnm1'$ orthorhombic crystal structure and corresponding pseudocubic representation. **a**, Construction of the pseudocubic unit cell from $Pbnm$ orthorhombic crystal structure with initial crystallographic axis a_0 , b_0 and c_0 . The ab plane is rotated by 45° and the new pseudocubic axis (a_{pc} , b_{pc} , c_{pc}) are approximated by equation 2.2. **b**, Illustration of the pseudocubic unit cell centered on the nickel ion which are surrounded by the oxygen octahedron. This representation facilitates the comparison of the different octahedral rotations and different axis lengths between different distorted structures.

$$a_{pc} = b_{pc} = \frac{\sqrt{a_0^2 + b_0^2}}{2} \quad c_{pc} = \frac{c_0}{2} \quad (2.2)$$

Tetragonal $P4/mmm1'$

The first step to lower the symmetry from the cubic crystal structure (Fig. 2.5a) is to lengthen (or shorten) one of the primitive cell axis, let's take the c axis, as shown in figure 2.5b (top for the elongation and bottom for the contraction).

It leads to a tetragonal structure with space group $P4/mmm1'$ ($P4/m2/m2/m1'$). Left panels of figure 2.5b are the $Pm\bar{3}m1'$ crystal structure representations centred on the rare earth ion while right panels are the primitive unit cells. Only one formula unit is required to describe the primitive unit cell. The difference between the lengths of the in-plane and out-of-plane axes breaks the $\bar{3}$ inversion rotation symmetry (dash red axis Fig. 2.3c). The 4-fold rotation (90°) around the dash green axis (Fig. 2.3c) with a mirror plane reflection m through a plane perpendicular (\perp) to the previous, remains. Two 2-fold (2) rotation symmetries are also present with their respective mirror plane reflection m (denoted by $2/m$). For example, SrTiO_3 , which is cubic at room temperature as mentioned above, undergoes a structural transition below 105 K to a tetragonal structure with $P4/mmm1'$ space group. Below 40 K it is even close to a symmetry

2. The physics of rare earth nickelates

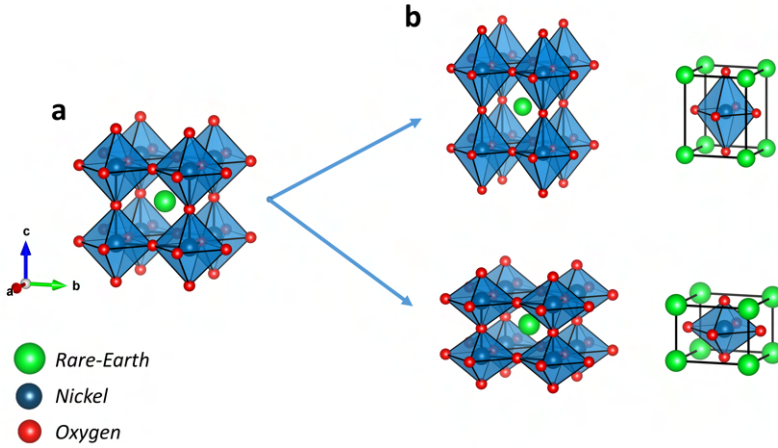


Figure 2.5: From cubic $Pm\bar{3}m1'$ to tetragonal $P4/mmm1'$ crystal structure. Green, blue and red balls are rare earth, nickel and oxygen atoms, respectively. **a**, Higher symmetric $Pm\bar{3}m1'$ cubic structure. **b**, Elongation (top) or contraction (bottom) of the c axis of the $Pm\bar{3}m1'$ cubic structure bringing to a tetragonal $P4/mmm1'$ crystal structure with an elongated or contracted octahedron. In-plane and out-of-plane Ni-O bond lengths are now different. Representation of $Pm\bar{3}m1'$ crystal structure centred on the rare earth ion (left) and primitive unit cell centred on the nickel site (right). Only one formula unit is required to describe the primitive unit cell.

breaking and a ferroelectric state [114]. Considering a primitive cell with an elongated (contracted) c axis, the octahedra have a similar stretching (contraction) in this direction and therefore the Ni-O bond length have different in-plane and out-of-plane values.

The rotation or tilt of the octahedra of this distorted structure depend on the compounds and the situation. Indeed, for SrTiO_3 the octahedra undergo a small out-of-phase rotation of about 1.4° [114] around the c axis described by $a^0a^0a^-$ in the Glazer notation, while theoretical studies, for example calculations on epitaxial strained SrRuO_3 , use tetragonal deformation without any octahedral rotation [117] giving $a^0a^0a^0$ Glazer notation. This crystal structure (with $a^0a^0a^0$) is used as a first approximation in our DFT calculation of strained LaNiO_3 thin films in chapter 3. It is compared with a calculation using a monoclinic $C2/c1'$ distortion. As will be shown, our DFT calculations don't show any interband transition when the tetragonal structure is taken into account. However, the $C2/c1'$ monoclinic distortion which is the real structure of strained LaNiO_3 films [6, 96] reveals interband transitions similar to experimental results, demonstrating the huge impact of octahedral rotation on the electronic properties. Table 2.4 summarizes

the notation $P4/mmm1'$ which is explicitly $P4/m2/m2/m1'$.

P	primitive
$4/m$	4-fold rotation (90°) around an axis (dash green axis in Fig. 2.3c) and mirror plane reflection through a plane perpendicular to the previous axis (delimited by orange line in Fig. 2.3c). / indicates that the 4-fold axis and the mirror plane are orthogonal.
$2/m$	2-fold rotation (180°) symmetry and mirror reflection m through a plane orthogonal to the 2-fold axis.
$2/m$	Similar to the previous point but differently oriented
$1'$	Time reversal symmetry.

Table 2.4: Summary of $P4/mmm1'$ (explicitly $P4/m2/m2/m1'$) space group notation.

Trigonal (rhombohedral) $R\bar{3}c1'$

From the cubic structure $Pm\bar{3}m1'$, it is also possible to lower the symmetry by maintaining equivalent crystallographic axis lengths but tilting them towards each other by a constant angle which leads to the trigonal crystal structure with space group $R\bar{3}c1'$ ($R\bar{3}2/c1'$). Note that the transition is indirect and several intermediate space groups are required (more details in Ref. [118]). While the structure appears to be completely deformed, as shown on the primitive unit cell in the rhombohedral setting (figure 2.6a), due to the fact that the three crystallographic axes have the same lengths and the three tilt angles have changed by the same amount, many symmetry elements are preserved. Two formula units are now required to describe the primitive unit cell but only one oxygen position is used to generate the crystal structure. The m mirror reflection symmetries from the $Pm\bar{3}m1'$ are broken due to the tilt of the three crystallographic axis. Remaining intact are the 3-fold inversion rotation $\bar{3}$ symmetry due to equivalent axis lengths, a 2-fold rotation symmetry around an axis oriented $[1,-1,0]$ shown in red in figure 2.6b, and a c -glide plane which is oriented orthogonally to the 2-fold axis $[1,-1,0]$ ($2/c$) and delimited by orange line in figure 2.6b. One check is shown in figure 2.6b: The top right dark blue nickel site is first displaced on the light blue circle after mirror reflection (double brown arrow) and then translated by $(a+b+c)/2$ along $\mathbf{a} + \mathbf{b} + \mathbf{c}$ (purple arrow) to the nickel site which takes place at the center of another primitive cell. Note that the translation of the c -glide operation is $(a+b+c)/2$ along $\mathbf{a} + \mathbf{b} + \mathbf{c}$. Indeed, two Bravais lattices can describe this trigonal structure: The rhombohedral setting (Fig.2.6a and b) and the hexagonal setting (Fig.2.6c and d). The notation $R\bar{3}c1'$ is based on the hexagonal setting which has a c -glide plane defined by a reflection through the mirror delimited by orange line (double

2. The physics of rare earth nickelates

brown arrow Fig. 2.6d) followed by a translation of $c/2$ along \mathbf{c} (purple arrow). In the rhombohedral setting, the same notation is used, but the c -glide plane is described in that case by a translation of $(a+b+c)/2$ along $\mathbf{a}+\mathbf{b}+\mathbf{c}$. While the rhombohedral setting has equivalent axis lengths and equivalent angles, the hexagonal setting has equivalent \mathbf{a} and \mathbf{b} axis lengths but a longer \mathbf{c} axis, two angles = 90° and one angle = 120° as shown in figure 2.6c. The hexagonal setting is tripled compared to the rhombohedral one. Note that the green dash line corresponding to the \mathbf{c} axis in the hexagonal setting (Fig. 2.6d), corresponds to the $\mathbf{a}+\mathbf{b}+\mathbf{c}$ direction in the rhombohedral setting (green dashed line in figure 2.6b).

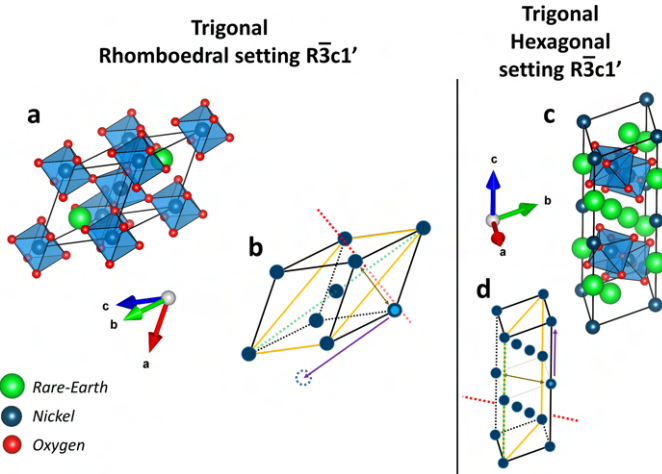


Figure 2.6: Trigonal crystal structure. Green, blue and red balls are rare earth, nickel and oxygen atoms, respectively. The three crystallographic axis have the same length and are tilted with respect to each other by the same angle. **a**, Primitive unit cell of the trigonal crystal structure with space group $R\bar{3}c1'$ in the rhombohedral setting. Two formula units are required to describe the primitive unit cell. **b**, Illustration of the c -glide plane symmetry. Check for one site: First the right bottom dark blue nickel site is moved to the light blue circle by the mirror reflection (double brown arrow) through the plane delimited by orange line and perpendicular to the 2-fold axis $[1,-1,0]$ red dash line, and is then translated by $(a+b+c)/2$ along $\mathbf{a}+\mathbf{b}+\mathbf{c}$ (simple purple arrow) to the nickel site located in the center of another primitive cell. It is called c -glide plane because the translation is along \mathbf{c} in the hexagonal setting. Green dashed line corresponds to the \mathbf{c} axis in the hexagonal setting. **c**, Hexagonal setting of the trigonal crystal structure with space group $R\bar{3}c1'$. **d**, Illustration of the c -glide plane symmetry. Check for one site: First the left middle dark blue nickel site is sent on the light blue circle by the mirror reflection (double brown arrow) through the plane delimited by the orange line and perpendicular to the 2-fold axis $[1,1,0]$ red dash line, and is then translated by $c/2$ along \mathbf{c} (simple purple arrow) to the nickel site at the top of the structure. The green dashed line corresponds to the $\mathbf{a}+\mathbf{b}+\mathbf{c}$ direction in the rhombohedral setting.

Bulk lanthanum nickelate LaNiO_3 adopts this rhombohedral $R\bar{3}c1'$ configuration. Related to the inclination of the rhombohedral edges, the octahedra rotate out-of-phase in the three crystallographic directions with the same magnitude (Fig. 2.6a) giving a Glazer notation $a^-a^-a^-$. The Ni-O-Ni γ angle is 165.2° in the case of bulk LaNiO_3 . Table 2.5 summarizes the notation $R\bar{3}1'$ which is explicitly $R\bar{3}2/n1'$.

R	Primitive with rhombohedral axis representation.
$\bar{3}$	3-fold rotation (120°) around an axis (dashed red axis in Fig. 2.3d) followed by inversion through the center of the rhombohedron.
$2/n$	2-fold rotation around an axis (red dashed line $[1,-1,0]$ in figure 2.6 c) and n -glide plane orthogonal to the 2-fold axis and delimited by orange line in figure 2.6c.
$1'$	Time reversal symmetry.

Table 2.5: Summary of $R\bar{3}1'$ (explicitly $R\bar{3}2/n1'$) space group notation.

Monoclinic $C2/c1'$

While bulk LaNiO_3 adopts a trigonal symmetry with space group $R\bar{3}c1'$, the epitaxial LaNiO_3 strained thin films reveal a lower symmetry. They have a monoclinic distortion with space group $C2/c1'$ whose face-centered primitive unit cell is shown in figure 2.7a.

Two formula units are required to describe the primitive unit cell and two lanthanum, two nickel and six oxygen atoms positions are used to generate the crystal structure. This monoclinic distortion is caused by different in-plane and out-of-plane bond lengths induced by strain. Note that in the case of LaNiO_3 thin films, the in-plane axes (parallel to the substrate) are **b** and **c**. This structure is used in the calculation of Peil et al. of LaNiO_3 thin film orbital polarization under tensile strain [61] and in our calculation in the chapter 3. The inequivalent axis lengths break the 3-fold inversion rotation $\bar{3}$ symmetry as for the tetragonal $P4/mmm1'$ structure. However, the 2-fold rotation symmetry (represented by a dashed red line in figure 2.7b) as well as the perpendicular c -glide plane (delimited by orange lines and perpendicular to 2-fold axis) remain. One example to check the c -glide plane symmetry is shown in figure 2.7b : The left top dark green rare earth is first moved on the light green circle after mirror reflection (double brown arrow) and is then translated by $c/2$ along **c** (purple arrow) to the green rare earth site. This structure can be reached either from the tetragonal $P4/mmm1'$ structure by breaking the 4-fold rotation symmetry (tilting one axis in relation to the other two axes) or from rhombohedral $R\bar{3}c1'$ by breaking the 3-fold inversion rotation $\bar{3}$ (changing the length of one axis relative to the other two axes).

2. The physics of rare earth nickelates

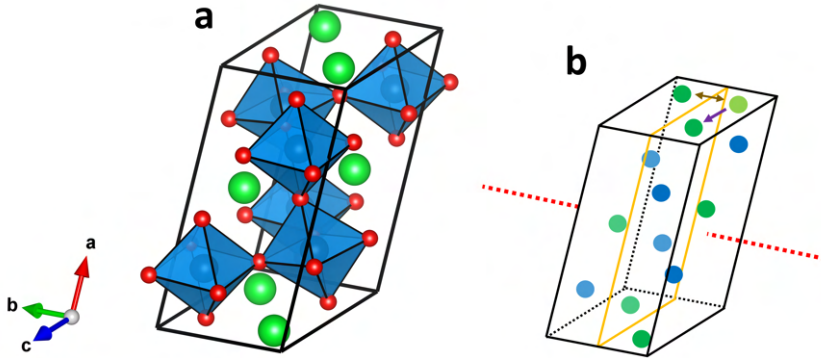


Figure 2.7: Monoclinic crystal structure with space group $C2/c1'$. Green, blue and red balls represent rare earth, nickel and oxygen atoms, respectively. The in-plane **b** and **c** axis lengths are equal unlike the out-of-plane axis **a** which is elongated (or contracted) and tilt by a monoclinic angle θ . The octahedra rotate out-of-phase in the three crystallographic directions and with the same magnitude around **b** and **c**. Note that LaNiO_3 thin films adopt this structure. **a**, Primitive unit cell of $C2/c1'$ crystal structure. Two formula units are required to describe the primitive unit cell. **b**, Illustration of the 2-fold axis $[0,1,0]$ (dashed red line) and c -glide plane delimited by the orange lines and perpendicular to the 2-fold axis. After mirror reflection through the plane, the top left dark green sphere is moved to the light green sphere (double brown arrow) and is then translated by $c/2$ along **c** (purple arrow).

In this structure, the octahedra rotate out-of-phase in the three crystallographic directions as in the rhombohedral $R\bar{3}c1'$ structure but only two directions (**b** and **c**) rotate with the same magnitude as seen in figure 2.7a, leading to the Glazer notation $a^-b^-b^-$. Note that for extreme compressive strain (-4%), the in-plane rotation increases and out-of-plane rotations go to zero ($a^-b^0b^0$), while for extreme tensile strain (+4%) the inverse occurs ($a^0b^-b^-$). Table 2.6 summarizes the notation $C2/c1'$.

C	Primitive c-face centred.
$2/c$	2-fold rotation around an axis $[0,0,1]$ and c -glide plane orthogonal to the previous axis.
$1'$	Time reversal symmetry.

Table 2.6: Summary of $C2/c$ space group notation.

Orthorhombic $Pbnm1'$

We now investigate the orthorhombic crystal structure with space group $Pbnm1'$ which is found in the metallic phase of nickelates $RNiO_3$ with $R = \text{Pr to Lu}$. To lower symmetry from the previous crystal structures, we have to start from the tetragonal $P4/mmm1'$ space group. Indeed, according to group theory, the transitions from space group $R\bar{3}c1'$ to $Pbnm1'$ or from $C2/c1'$ to $Pbnm1'$ are not allowed [6]. From the tetragonal $P4/mmm1'$ space group it is sufficient to change the **a** or **b** axis length (such that all the three **a**, **b** and **c** axis lengths are inequivalent) to get the orthorhombic structure with space group $Pbnm1'$. Note that the transition is indirect and several intermediate space groups are required (more details in Ref. [118]). The orthorhombic $Pbnm1'$ primitive unit cell is presented in figure 2.8. Four formula units are now required to describe the primitive unit

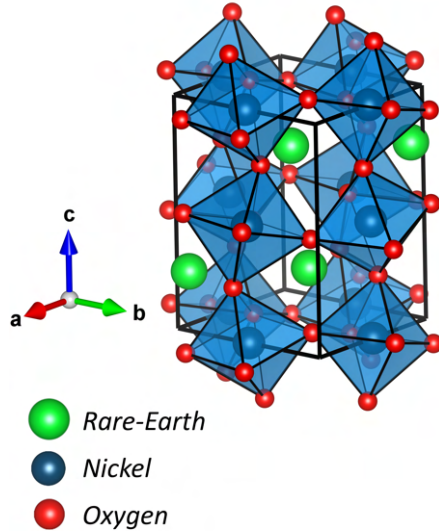


Figure 2.8: Orthorhombic $Pbnm1'$ primitive unit cell. Four formula units are required to describe the primitive unit cell. Green, blue and red balls are rare earth, nickel and oxygen atoms, respectively. The three crystallographic axis are inequivalent. The octahedra rotate out-of-phase with same magnitude along **a** and **b** and in-phase with a different magnitude along **c**, giving $a^- a^- c^+$ Glazer notation.

cell and two oxygen positions are necessary to construct the symmetry. Of course, the 4-fold rotation symmetry is broken due to the different axis lengths. However, the structure respects many symmetries such as mirror reflections or 2-fold rotations but can be described by only three symmetry

2. The physics of rare earth nickelates

operations: One mirror reflection m , one b -glide plane (mirror reflection + translation $\mathbf{b}/2$) and one n -glide plane (mirror reflection + translation along half a face diagonal). Note that three different notations of the same orthorhombic structure are found in the literature, $Pbnm$, $Pmcn$ and $Pnma$, corresponding to different permutations of the crystallographic axis. We observe that the mirror reflection m and the n -glide plane appear in the three notations and only the axis linked to the a , b or c -glide plane changes.

The b -glide plane is comparable to the c -glide plane of the $C2/c1'$ space group. It is a reflection through a plane perpendicular to $[1,0,1]$ then a translation of $b/2$ along \mathbf{b} . The n -glide plane is a reflection through the plane perpendicular to $[0,0,1]$ followed by a translation of $(a+b)/2$ in the $[1,1,0]$ direction ($=\mathbf{a}+\mathbf{b}$). A planar reflection m with plane perpendicular to $[1,1,0]$ completes the description of the structure. The Ni-O bond lengths are now inequivalent in the three crystallographic directions. The octaedra are out-of-phase rotated around the \mathbf{a} and \mathbf{b} axis with the same magnitude while they are in-phase rotated around the \mathbf{c} axis with a different magnitude which corresponds to the Glazer notation $a^-a^-c^+$. As seen above, decreasing the size of the rare earth decreases the Ni-O-Ni γ angle. For example, the γ angle is 157° for neodymium nickelate and 146.7° for yttrium nickelate. Table 2.7 summarizes the notation $Pbnm1'$.

P	Primitive.
b	b -glide plane composed of a mirror reflection through a plane \perp $[1,0,1]$ followed by a translation $b/2$ along \mathbf{b} .
n	n -glide plane composed of a mirror reflection through a plane \perp $[0,0,1]$ followed by a translation along half a face diagonal, i.e. $(a+b)/2$ in $[1,1,0]$ direction ($\mathbf{a}+\mathbf{b}$).
m	Mirror reflection.
$1'$	Time reversal symmetry.

Table 2.7: Summary of $Pbnm$ space group notation.

Monoclinic $P2_1/c1'$

The insulating phase of nickelates is characterized by the emergence of an octahedral breathing mode which induces an alternation between long and short Ni-O bond lengths in a 3D checkboard configuration as shown in figure 2.9. This is also called bond disproportionation or breathing distortion. The smaller the rare earth radius, the stronger is the bond disproportionation [119]. Two different Ni sites are thus required to describe the structure and this new configuration leads to a ground state with monoclinic distortion of space group $P2_1/c1'$. The $P2_1/c1'$ primitive unit cell is presented in figure 2.9.

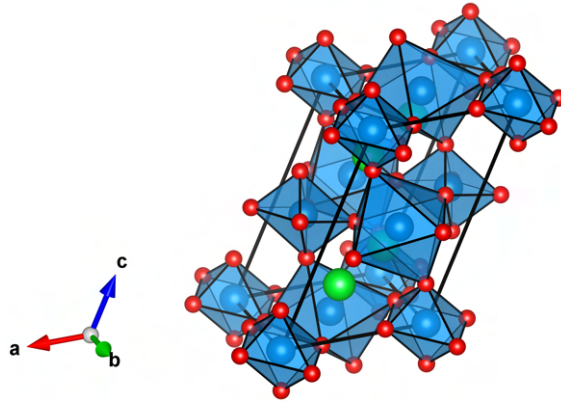


Figure 2.9: Monoclinic structure with space group $P2_1/c1'$ of the nickelates insulating phase. Primitive unit cell. Four formula units are required to describe the unit cell. The structure is characterised by an octahedral breathing mode inducing an alternation between long and short Ni-O bond lengths in a checkboard configuration of so-called bond disproportionation or breathing distortion. The structure is similar to the orthorhombic structure with three different axis lengths but is characterized by the inclination between the c axis and the ab plane at an angle θ . The inclination is very small and the monoclinic angle θ is around 90.1° for YNiO_3 , which is exaggerated here for clarity.

Four formula units are required to describe the primitive unit cell (taking into account the the two different Ni sites). Two nickel and three oxygen inequivalent atom positions are necessary to construct the crystal symmetry. The crystal structure is similar to the orthorhombic one, except the inclination between the c axis and the ab plane at an angle θ . The inclination is very small and the monoclinic angle θ is around 90.1° [39] which was exaggerated

2. The physics of rare earth nickelates

($\sim 120^\circ$) in figure 2.9 for clarity. The structure is now described by a 2_1 screw axis (2-fold rotation around an axis followed by a translation along the unique axis \mathbf{b}) and a c -glide plane symmetry whose plane is orthogonal to the screw axis. These symmetry operations are fully used and detailed in the section 2.4. The bond disproportionation is accompanied by a charge disproportionation explained in the section 2.3. The octahedral rotation has different magnitude around the three crystallographic axis but there are still two out-of-phase rotations (around the \mathbf{b} and \mathbf{c} axes) and one in-phase rotation (around the \mathbf{a} axis), leading the Glazer notation $a^+b^-c^-$.

Table 2.8 summarizes the notation $P2_1/c1'$.

P	Primitive.
2_1	Screw axis symmetry defined as a 2-fold rotation around an axis followed by a translation of $b/2$ along \mathbf{b} .
c	c -glide plane which is orthogonal to the screw axis.
$1'$	Time reversal symmetry.

Table 2.8: Summary of $P2_1/c1'$ space group notation.

Note that this structure has different notations. Indeed, as shown in figure 2.10a, the structure can be defined with two different \mathbf{c} axis. The diagonal axis, noted by \mathbf{c} , is the conventional \mathbf{c} axis of the monoclinic $P2_1/c1'$ crystal structure and belongs to the real primitive unit cell. The vertical axis, denoted by \mathbf{c}' , belongs to an alternative representation called $P2_1/n1'$. \mathbf{c}' is the sum of \mathbf{c} and \mathbf{a} ($\mathbf{c}'=\mathbf{c}+\mathbf{a}$). While the primitive cell monoclinic structure (with \mathbf{c}) has different nickel planes (five nickel atoms in the first layer, four shifted nickel atoms in the second layer, and again five nickel atoms in the third layer) as shown in figure 2.10b, the alternative representation (with \mathbf{c}') has similar crystallographic nickel planes which eases the check of symmetry operations such as glide plane and screw axis.

Note that the conversion from the real primitive cell to the alternative representation ($\mathbf{c} \rightarrow \mathbf{c}'$) does not change the symmetry operations. Therefore, the c -glide plane in the real primitive cell representation $P2_1/c1'$ becomes a n -glide plane (half a diagonal translation $\mathbf{c}' + \mathbf{a}$) in the alternative representation $P2_1/n1'$. The latter notation is used in the section 2.4 to check which symmetry operations the magnetic orders respect. Figure 2.10c shows the $P2_1/n1'$ representation whose the nickel sites with long bonds (blue circles) and short bond (orange circle) are differentiated. Due to the tilt of the octahedra, a nickel site after a mirror reflection or a 2-fold rotation has a different orientation. The same octahedron but with different orientation is illustrated by the inverted colors of the circle. One 2_1 screw axis is represented by the green line in figure 2.10c. There are in total four screw axis operations, two primed (time reversal symmetry) screw axis and

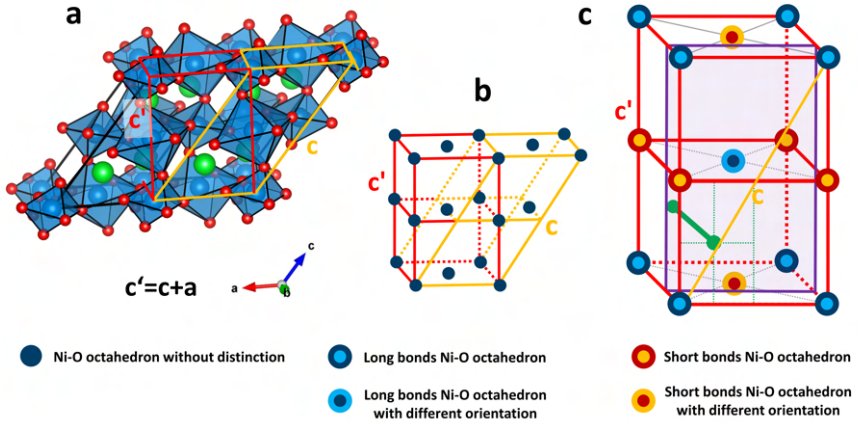


Figure 2.10: Monoclinic structure. **a**, Monoclinic crystal structure with two possible representation of c axis, c and c' . **b**, $P2_1/c1'$ representation with c axis and $P2_1/n1'$ representation with c' axis. Blue circles represent the Ni-O octahedron without distinction. **c**, $P2_1/n1'$ representation of the monoclinic crystal structure with short bonds (blue circles) and long bond (orange circle) nickel sites. After reflection or rotation, octahedra have different orientations illustrated by inverted colors of the circles.

two unprimed screw axis. One glide plane is delimited by the purple lines in figure 2.10c. There are in total four glide plane operations, two primed glide planes (mirror reflection + $(c'+a)/2$ translation) and two unprimed glide planes (mirror reflection + $(c'-a)/2$ translation). It has been reported that the antiferromagnetic propagation vector in nickelates magnetic phase is $(1/2, 0, 0)_c$ in the $P2_1/c$ space group [42–44], which is $(1/2, 0, 1/2)_n$ in the $P2_1/n$ setting and $(1/4, 1/4, 1/4)_{pc}$ in the pseudocubic representation. Doubling the a axis of the $P2_1/c$ space group allows the structure to host this antiferromagnetic order. The translation T_a is obsolete considering that two simultaneous translations of a are now required. We note this new symmetry operation T_{2a} and this symmetry operation will be used in all the studied magnetic structures of this work. The magnetic space group is $P_{2a}2_1/c$ which doubles the unit cell (eight formula units are required to describe the primitive unit cell). From the $P2_1/n$ representation, the a and c' axis have to be doubled to host the magnetic order. The magnetic space group is denoted by P_b2_1/n ($P_b = P_{2a2c}$ means that only the b axis is not doubled [113]) which describes twice the primitive cell of the magnetic structure. Note that the $1'$ no longer appears in the space group. Indeed, time reversal symmetry is now broken due to magnetic moments/spins hosted by nickel sites. Implicitly the structure still respects the inversion

2. The physics of rare earth nickelates

symmetry $\bar{1}$. For the antiferromagnetic $P_{2a}2_1/c$ space group, one half of the Ni sites have inversion symmetry, and the other half does not. Consequently, half of the nickel sites can not have a magnetic moment. Suppression of the magnetic moment of Ni has an energy cost of several eV due to the splitting between high-spin and low-spin. However, various authors [120–125] have proposed an alternation of high-spin d^8 sites and low-spin $d^8\bar{L}\bar{L}$ sites, which is compatible with this magnetic structure.

From the magnetic $P_{2a}2_1/c$ structure, it is possible to lower the symmetry by breaking the 2_1 screw axis or the c -glide plane symmetries (or both). On one hand, breaking the 2_1 screw axis leads to the $P_{2a}c$ space group which keeps the T_{2a} , T_b and T_c translation symmetries and the c -glide plane. On the other hand, breaking the c -glide plane leads to the $P_{2a}2_1$ space group which keeps the T_{2a} , T_b and T_c translation symmetries and the 2_1 screw axis. These two structures are monoclinic and lose the inversion center symmetry $\bar{1}$. Breaking simultaneously the 2_1 screw axis and c -glide plane leads to the $P_{2s}\bar{1}$ space group. s means that there is no privileged axis, and \mathbf{a} , \mathbf{b} or \mathbf{c} may be double. Indeed, \mathbf{b} is not the unique axis any more because the two directional symmetry operations are now broken. Note however that $\bar{1}$ inversion symmetry is still present. Indeed, two symmetries can be broken while their product still remains. Breaking the individual symmetries, c -glide plane for $P_{2a}c$, 2_1 screw axis for $P_{2a}2_1$, and $\bar{1}$ inversion for $P_{2s}\bar{1}$, lead to the space group $P_{2s}1$.

The lowering of the symmetry from $Pm\bar{3}m1'$ to $P_{2s}1$ is summarized in figure 2.11. All the last space groups will be useful in considering the different possible antiferromagnetic structures of nickelates which will be developed in the section 2.4.

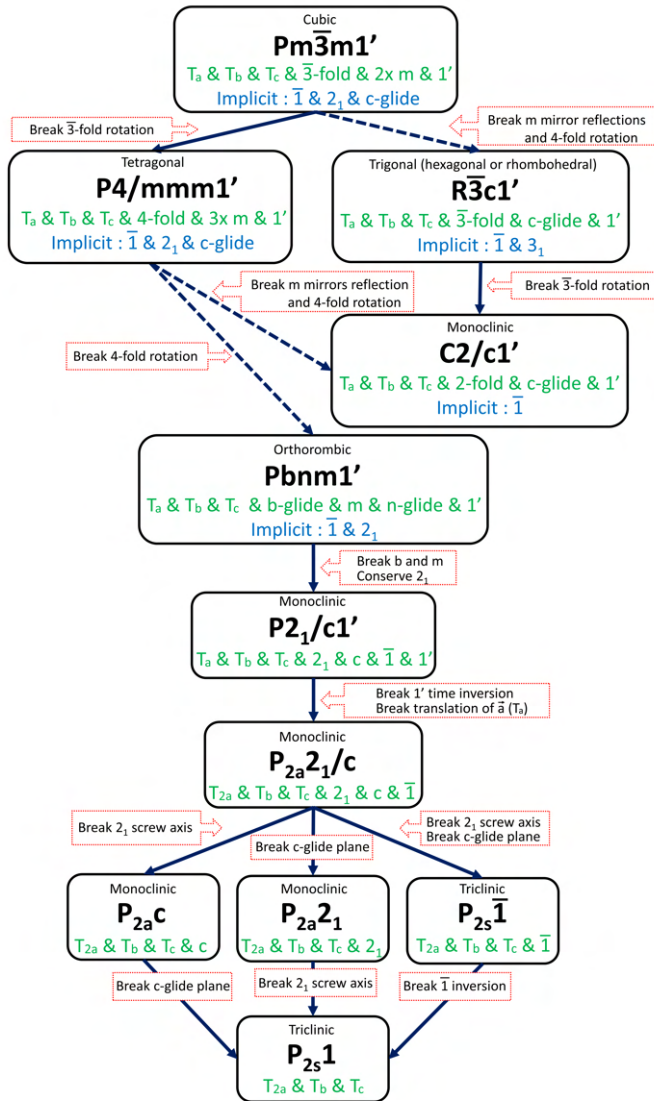


Figure 2.11: Summary of the crystal structures from the highest $Pm\bar{3}m$ to the lowest $P2_s1$ symmetry space group specifying symmetry elements that are broken from one space group to the next. Dash lines represent indirect transitions, i.e. several intermediate space groups are required (more details in Ref. [118]).

2.3 Electronic structure

2.3.1 Band structure

In most nickel compounds, nickel is divalent with a high spin $3d^8$ configuration. In RNiO_3 , nickel is formally trivalent, corresponding to a $3d^7$ configuration. However, the extra hole has most of its wave function spread on the neighbouring oxygen ligand atoms which can be written as $3d^8\bar{L}$. The first approach to understand the electronic structure of nickelates is to study the band structure without correlations. We will see that without including correlations nickelates are predicted to be metallic even in the monoclinic phase which experimentally is observed to be insulating. In this section, the bandstructure reported in several Density Functional Theory (DFT) studies [61, 126–133] on various phase and structures of RNiO_3 will be presented and discussed. DFT calculation, which take into account the potential induced by the atoms and the crystal structure (V_{ext}), as well as an effective potential that is a mean field induced by electronic interactions (V_{eff}). A numerical solution to this calculation is straightforward, however the exact form of the exchange-correlation (XC) energy functional used in this theory is not known. Several approximations to the XC exist, such as the Local-Density Approximation (LDA) which considers an uniform electron density $\rho(\mathbf{r})$, or the Generalized Gradient Approximation (GGA) which takes into account the density variation.

Figure 2.12a shows the bulk DFT LaNiO_3 band structure calculated by Nowadnick [129] for cubic (red) and rhombohedral (black) structures. A band crosses the Fermi level between Γ and M reciprocal space points for the cubic structure which is doubled in the rhombohedral distortion due to zone folding. The rhombohedral distortion reduces the Ni-O hybridization which decreases the Fermi velocity of the $\Gamma - M$ band and lowers the binding energy of the shallow band bottom at the M point.

To study the band structure evolution of LaNiO_3 thin films as a function of strain, Peil, Ferrero and Georges [61] start their study by calculating the 0% strained film as shown in figure 2.12b and characterizing the Ni $3d_{z^2}$ (red) and the Ni $3d_{x^2-y^2}$ (blue) e_g orbital contributions. Thin strained films of LaNiO_3 have a lower crystal symmetry due to monoclinic distortion (space group $C2/c$). While the e_g - $\text{O}2p$ hybridization is more favourable due to the same orbital orientation (explained in the next section), they report a clear flattening of the bands around the Fermi level and explain this behaviour by the hybridization with the t_{2g} states which are also close to the Fermi level. These results are very similar to the $R\bar{3}c$ band structure in figure 2.12a and both show a metallic behaviour for bulk LaNiO_3 and thin films. Our results of band structure calculations on strained LaNiO_3 are given in the chapter 3.

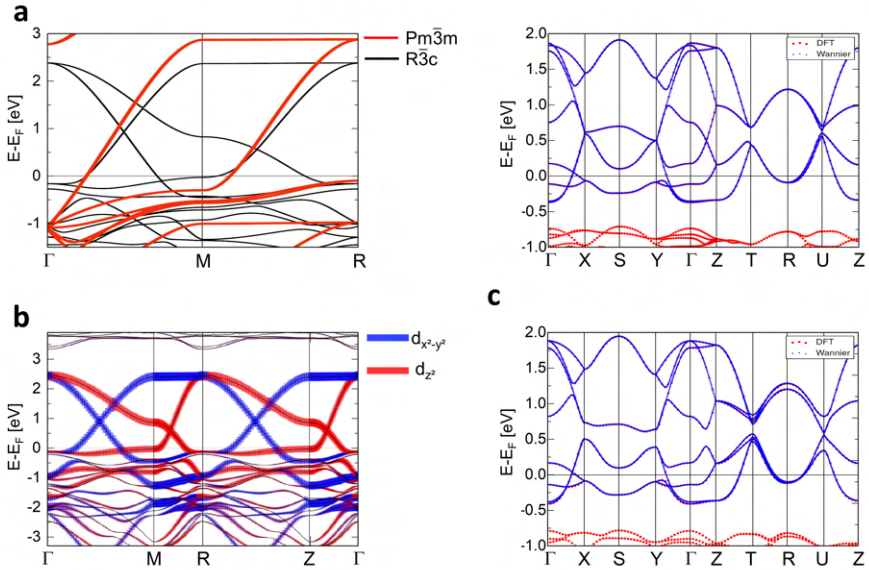


Figure 2.12: DFT band structure calculations. **a**, Bulk LaNiO_3 rhombohedral $R\bar{3}c$ [129]. **b**, Monoclinic ($C2/c$) LaNiO_3 thin films at 0% strain [61]. **c**, Orthorhombic $Pbnm$ LuNiO_3 (top), Monoclinic $P2_1/c$ LuNiO_3 (bottom) [130].

For smaller rare earth elements, from Pr to Lu, it is known that the crystal structure is orthorhombic at high temperature and monoclinic at low temperature [37–39, 41, 86] as described in section 2.2.1. Figure 2.12c shows the calculated band structure [130] of orthorhombic (top) and monoclinic (bottom) LuNiO_3 (Lu being the smallest rare earth, and therefore LuNiO_3 the most deformed structure). Eight e_g bands close to the Fermi energy are present for both structures (corresponding to four nickel sites by primitive unit cell, and two e_g bands for each site) separated by a gap from the lower energy t_{2g} bands. A small “Peierls gap” of about 0.5 eV is visible in the monoclinic phase and comes from the two types of nickel sites characterising this structure. Long bonds nickel sites are pushed down in energy compared to the more covalent short bonds nickel ones. However, no gap appears at the Fermi energy in the monoclinic structure indicating that the material is still metallic in this configuration according to DFT calculations. A metallic groundstate was similarly calculated for the less distorted structure of SmNiO_3 [62]. Early theoretical work [134] already showed the systematic reduction of the e_g bandwidths with decreasing atomic rare earth radius caused by the Ni-O-Ni distortion. However, the decrease of the bandwidth is

2. The physics of rare earth nickelates

not sufficient to drive a metal-insulator transition in nickelates and the study concludes that their insulating ground states are likely due to electronic correlations and covalency effects, which is now a generally accepted point of view [122, 123, 125, 130, 135, 136].

2.3.2 Electron-electron correlations

We start this section with a famous and controversial story that took place in the mid-20th century regarding the electronic structure of NiO. While the theoretical DFT calculation predicted a semi-conducting behaviour for NiO with a gap of 0.3 eV, the local cluster approach including configuration interaction (post-Hartree-Fock linear variational method) predicted a gap of 5 eV, which is 16 times higher. To settle this conflict, Sawatzky and Allen used photoemission and bremsstrahlung-isochromat-spectroscopy on NiO single crystals which revealed a gap of 4.3 eV [137]. The nickel d-d Coulomb repulsion is between 7 and 9 eV. However, the oxygen 2*p* states are detected inside the nickel 3*d* gap which means that they also contribute to correlations and the material cannot therefore be considered as a Mott-Hubbard insulator. This example demonstrates the impact of electronic correlations and their predominant role in the physics of nickel oxides. Indeed, all modern quantum theories of matter are now considering the electron-electron correlations and their impact on physical properties such as transport measurement or optical conductivity.

In 1900, Paul Drude proposed a theory that describes the dynamics of electrons inside a metal. This relatively simple model is based on the assumptions that the density of free carriers satisfies the kinetic gas theory, and that there is no electron-electron interaction. The only "interactions" are collisions between the conduction electrons and the impurity or defect ions. These scattering events are further considered to be instantaneous. The time between two collisions is defined as the relaxation time τ and the scattering rate is defined as $1/\tau$. Based on these assumptions, the complex and frequency dependent optical conductivity can be shown to have the form:

$$\sigma(\omega) = \frac{1}{4\pi} \frac{\omega_p^2 \tau}{1 - i\omega\tau} \quad (2.3)$$

with $\omega_p = \sqrt{\frac{4\pi n e^2}{m_e}}$ the plasma frequency, n the electronic density, e and m_e the charge and the mass of electron respectively. This equation is a good approximation of the optical conductivity of many common metals such as gold, silver, or aluminum [138, 139] but is inappropriate in systems where many body correlations play an important role. Indeed, when electrons interact with each other or with bosons, the scattering rate becomes

frequency-dependant. To model this type of interaction, Gotze and Wolfle proposed in 1972 to change the constant scattering rate $1/\tau$ by a complex and frequency dependent scattering rate $M(\omega)$ known as the Memory function $1/\tau \rightarrow -iM(\omega)$ with $M(\omega) = M_1(\omega) + iM_2(\omega) = (\frac{m^*(\omega)}{m} - 1)\omega + i\frac{1}{\tau(\omega)}$ [140], where m is the band mass and m^* the effective mass of the quasi-particle. The imaginary part of the Memory function defines the energy-dependent scattering rate while the real part is related to the effective mass $m^*(\omega)$ of the quasi-particles, which accounts for the different interactions that affect the motion of the electron inside the matter. Note that the effective mass is also frequency-dependent. Berthod et al. [141] observe that for a local Fermi liquid, the "two-body" interaction model of perturbation theory (the low energy approximation taking into account the first terms of the Hartree terms or the exchange process as it is done in the random phase approximation) always shows that the imaginary part of the self-energy $\Sigma = \Sigma_1 + i\Sigma_2$ (potential felt by the electrons) is proportional to the sum of the square of the energy ϵ and the square of the temperature T , i.e. $Im(\Sigma(k, \epsilon)) \propto \epsilon^2 + (\pi k_B T)^2$. From Kramers-Kronig relations, the real part of Σ is proportional to ϵ and they deduce the self-energy of a local Fermi liquid (at low frequency and temperature) to be:

$$\Sigma(\epsilon, T) = \left(1 - \frac{1}{Z}\right) \epsilon - \frac{i}{Z\pi k_B T_0} [\epsilon^2 + (\pi k_B T)^2] \quad (2.4)$$

with $Z = m/m^*$ and T_0 a characteristic energy scale depending on the material. In the thermal regime, the memory function of a Fermi liquid can be approximated by:

$$M(\omega) \sim \left(\frac{1}{\tilde{Z}} - 1\right) \omega + i\frac{1}{\tilde{Z}} \frac{2}{3\pi\hbar k_B T_0} [(\hbar\omega)^2 + (2\pi k_B T)^2] \quad (2.5)$$

where $\tilde{Z} = \frac{Z\Phi(0)}{\epsilon_0\omega_p^2}$.

Strongly correlated electrons show large effective mass, for example around $m^*(0)/m = 3$ for lanthanum nickelates [54, 56]. In the previous section, we saw that DFT calculations predict metallic properties for nickelates even in the monoclinic structure which suggests that correlations drive the insulating ground state. Indeed, all recent studies agree that electronic correlations are the origin of the bad metallicity of LaNiO_3 [54, 56, 68, 129, 142] and induce the low temperature insulating transition in all other nickelates [122, 123, 125, 130, 135, 136]. To understand the impact of correlations, we consider the different models which can describe the electronic behaviour of nickelates (nickel in a $3d^7$ configuration with $t_{2g}^6 e_g^1$ Fig. 2.13b). In the case of Mott-Hubbard insulators, the system is in a ground state d^7 . In the following we will use the reduced notation where for example $d^7 = \tilde{d}^7$ and $d^8 \underline{L} = \tilde{d}^7$. As shown in figure 2.13c, because of on-site electron-electron Coulomb repulsion

2. The physics of rare earth nickelates

U , the cost for intersite electron hopping corresponding to $\tilde{d}^7 + \tilde{d}^7 \rightarrow \tilde{d}^6 + \tilde{d}^8$ (hole on a nickel site and two electrons on another) is U . However, this model does not completely describe the physics of late transition metals, such as nickelates [6, 143], and Zaanen, Sawatzky and Allen (ZSA) proposed in 1985 a new theory that takes into account the ligand oxygen [144]. In charge transfer insulators, the spatial alignment and comparable energy of oxygen $2p$ and nickel $3d$ orbitals as shown in figure 2.13a promotes the transfer of an electron from oxygen $2p$ to nickel $3d$ bands. It means that this excitation is closer to the ground state \tilde{d}^7 , opening a gap $\Delta < U$ and therefore favours a $\tilde{d}^7 + \tilde{d}^7 \rightarrow d^7 \underline{L} + d^8 = \tilde{d}^6 + \tilde{d}^8$, rather than a d-d excitation as shown in figure 2.13d. Note that the $3d^7 \underline{L}$ means that the nickel has 8 electrons whose one of them comes from the ligand oxygen denoted by \underline{L} (and therefore there is a hole on the oxygen). Furthermore, considering that the e_g orbitals point in the same direction as the oxygen p orbitals (Fig. 2.13a), e_g - Op hybridization is more favourable than t_{2g} - Op . The conducting behaviour is therefore driven by the hybridization between the $2p$ oxygen and $3d$ nickel orbitals in nickelates.

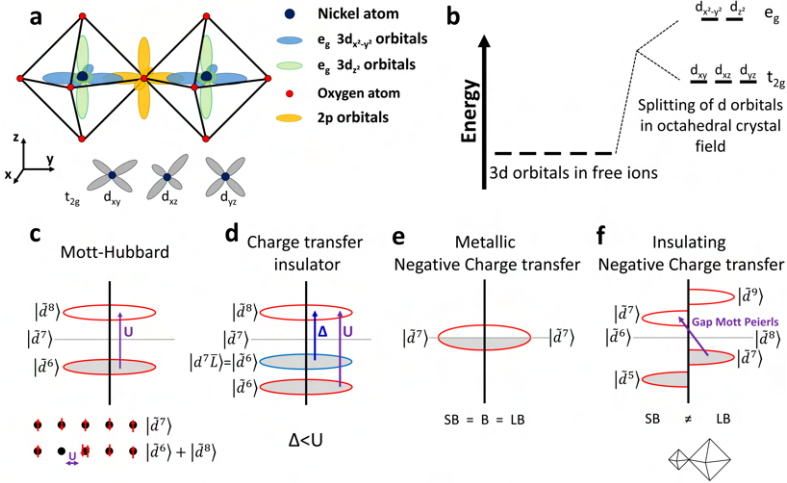


Figure 2.13: **a**, Illustration of two corner sharing octahedra and spatial representation of the $3d e_g$ nickel and $2p$ oxygen orbitals hybridization. **b**, Splitting of the nickel $3d$ orbitals in an octahedral crystal field. **c**, Mott-Hubbard insulator schematic representation of excitations. The grey middle line correspond to the \tilde{d}^7 ground state. The U site repulsion split the Fermi level band into two bands, the upper (\tilde{d}^8) band and the lower (\tilde{d}^6) band. The system needs an energy U to allow an electron from site 1 to jump on site 2 ($\tilde{d}^7 + \tilde{d}^7 \rightarrow \tilde{d}^6 + \tilde{d}^8$). **d**, Charge transfer insulator schematic representation of excitations. **e**, Metallic phase of negative charge transfer nickelates with continuous excitations around the \tilde{d}^7 ground state. **f**, Insulating phase of negative charge transfer nickelates. The system is splitted into short and long bonds octahedra.

The charge transfer gap may be very small and even negative [145] as in the case of nickelates, which are defined as negative charge transfer insulators [146]. In this case, it is rather a transfer of a hole from the nickel to the ligand oxygen sites which has to be considered but the result still remains a $3d^8\bar{L}$ configuration. Figure 2.13e shows the metallic phase of nickelates (negative charge transfer) in a $d^8\bar{L} = \tilde{d}^7$ configuration ground state, which may go in a lower or higher excitation state through the excitations continuum since there is no gap.

Below T_{MI} , the octahedra which are equivalent in the orthorhombic structure, reorganize in a checkboard configuration of compressed octahedra with short Ni-O bonds (SB) and expanded octahedra with long Ni-O bonds (LB). Note that the bond disproportionation does not necessarily involve a charge transfer because each oxygen is shared by LB and SB nickel sites, which induce the same average hole concentration for all the octahedra [124]. However, the two ligand holes of the SB octahedra acquire e_g orbital symmetry and therefore these sites are equivalent to $3d^6$. The reason for the bond disproportionation is purely energetic. To lift the degeneracy of the e_g level, and for comparable energy of U and J, Mazin et al. explain that the system favors the occupation of two electrons on one site and zero electrons on the other with $e_g^1 + e_g^1 \rightarrow e_g^0 + e_g^2$ by bond disproportionation without charge transfer. This occurs rather than a distortion of the structure by Jahn-Teller effects [143], which have never been observed in nickelates. On the other hand, charge disproportionation, as just described, was observed in the monoclinic structure in 1999 [120]. The extreme picture of the metal-insulator transition is therefore described by: $d^8\bar{L} + d^8\bar{L} \rightarrow d^8\bar{L}^2 + d^8$ (or $\tilde{d}^7 + \tilde{d}^7 \rightarrow \tilde{d}^6 + \tilde{d}^8$) assigning the $d^8\bar{L}^2 = \tilde{d}^6$ to the SB nickel sites (with spin $S = 0$) and the $d^8 = \tilde{d}^8$ to LB nickel sites (with $S = 1$). This is in agreement with DMFT calculations [122] and experimental results [62, 70]. Using this picture, Park et al. explain that the insulating phase is in fact driven by two insulating regimes and the transition named as site-selective Mott transition [122]. While the \tilde{d}^8 sites contribute to a Mott insulating phase with a pole at zero frequency in the imaginary part of the self energy, the \tilde{d}^6 sites are considered as a Kondo insulator where a singlet is formed by the strong coupling between the nickel electrons and the two holes on the oxygen sites leading to a gap (without pole) in the imaginary part of the self energy. The LB octahedra may undergo the excitation $\tilde{d}^8 + \tilde{d}^8 \rightarrow \tilde{d}^7 + \tilde{d}^9$, while SB octahedra may undergo the excitation $\tilde{d}^6 + \tilde{d}^6 \rightarrow \tilde{d}^5 + \tilde{d}^7$. Considering both LB and SB octahedra, and a large U pushing the upper (LB) Hubbard band above the unoccupied band of SB states, the more likely transition is a $\tilde{d}^7 \rightarrow \tilde{d}^7$ transition, named Mott-Peierls gap, which is supported by experimental data [62] and discussed in the next section. The schematic representation of these excitations are shown in figure 2.13f.

2. The physics of rare earth nickelates

Subedi et al. show explicitly that the simple Mott insulator interpretation is impossible [125]. They calculated the phase diagram of the low-energy model for LuNiO_3 as a function of Hund's rule coupling J and on-site repulsion U for orthorhombic and monoclinic structures shown in figures 2.14a and b, respectively.

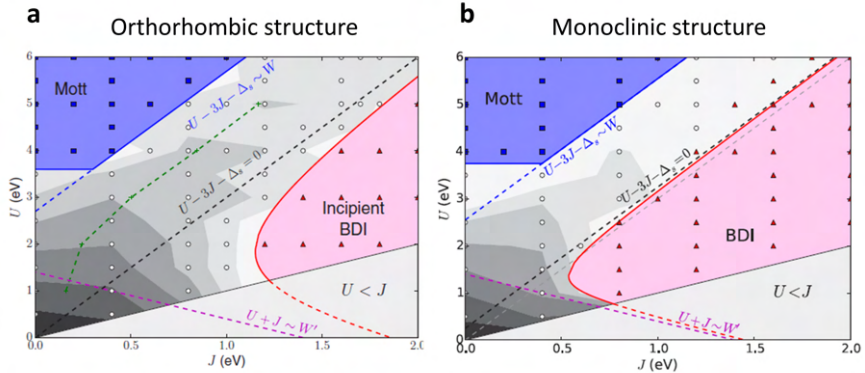


Figure 2.14: DFT+DMFT phase diagram of the low-energy model for LuNiO_3 as a function of Hund's rule coupling J and on-site repulsion U from Ref. [125]. **a**, Phase diagram for the orthorhombic structure. **b**, Phase diagram for the monoclinic structure.

The Mott insulator regime does not evolve as a function of the structure while the bond disproportionated insulator (BDI) phase spreads to lower values of J for the monoclinic distortion. Since $J \sim 0.8$ eV for nickelates, this shows that the metal-insulator transition is not induced by a Mott transition but rather by a bond disproportionation.

While the Mott insulator regime takes place at nearly the same value of U and J for both the orthorhombic and monoclinic structures, the region of the phase diagram occupied by the bond disproportionated insulator (BDI) changes dramatically between the two symmetries. Taking a value of $1 < U < 2$ (eV), the limit of J of the incipient BDI is around $J \sim 1.2$ (eV) in the orthorhombic structure but falls to a lower value of $J \sim 0.55$ (eV) in the monoclinic state. At $J \sim 0.8$ (eV) and with $1 < U < 2$ (eV), which are appropriate typical values for nickelates, the phase diagram in Fig. 2.14 suggests that LuNiO_3 is metallic in the orthorhombic structure and insulating for the monoclinic distortion. Subedi et al. conclude that the sizable Hund's coupling, the on-site repulsion U (more exactly the negative charge transfer energy) as well as the strong coupling to lattice effects through bond-length disproportionation, drive the charge disproportionation already predicted and observed since 1999 [37, 39, 119, 122, 124, 143, 147, 148] and therefore induce the metal-insulator transition in nickelates.

The charge disproportionation can be viewed as a consequence of bond disproportionation. It was proposed early on that the charge disproportionation was driving the orthorhombic-to-monoclinic transition [120]. However, a recent study [149] shows that the metallic phase of LaNiO_3 and NdNiO_3 , whose crystal structures are considered as rhombohedral and orthorhombic, respectively, already have monoclinic distortion. This observation supports the presence of two different types of nickel sites above T_{MI} when viewed locally, which are averaged by fluctuations on long length scales and therefore can be described by higher symmetry. Actually, the lattice structures undergo a dynamic and fluctuating breathing mode in the metallic phase which "freezes" in the insulating regime into a long range periodic structure. This implies a coupling between the lattice and the free carriers which can be viewed as a polaronic electron-phonon coupling. This electron-phonon coupling can also be responsible for the bad metallic state of nickelates.

2.3.3 Metallic phase of LaNiO_3 thin films and metal-insulator transition of the other nickelates

By virtue of the absence of a metal-insulator transition, lanthanum nickelate is a good candidate to probe the evolution of the band structure as a function of epitaxial strain induced on thin films. Two studies [61, 129] show the evolution of the band structure of LaNiO_3 thin films from compressive to tensile strain and analyse the impact of strain on the d_{z^2} and $d_{x^2-y^2}$ e_g bands (see Fig. 2.13b). The films are monoclinic with space group $C2/c$ [6] and remain metallic for both tensile and compressive strain. However, for tensile strain, DFT shows a higher energy shift of the d_{z^2} band center of gravity relative to the $d_{x^2-y^2}$ band with the compression of the octahedra, and a decrease of the $d_{x^2-y^2}$ bandwidth due to an increase of the in-plane lattice constant.

Moreover, tensile strain decreases the c/a bond length ratio and in-plane octahedra rotation angle, while it increases the out-of-plane rotation angle and orbital polarization ($P = \frac{n_{x^2-y^2} - n_{z^2}}{n_{x^2-y^2} + n_{z^2}}$), with n_i the orbital occupation number, which results in a greater occupation of the $d_{x^2-y^2}$ orbital. Compressive strain has the opposite effect, a decrease of the out-of-plane rotation angle and orbital polarization and an increase of the in-plane octahedral rotation angle, which results in a greater occupation of the d_{z^2} orbital. These results confirm the fact that orbital polarization can be controlled by lattice engineering.

A Lifshitz transition was also observed by angle-resolved photoemission spectroscopy on thin films of LaNiO_3 passing from compressive to the tensile strain [150]. This reconstruction of the Fermi surface has a huge impact on the spectral weight of the free carriers. It is also known that

2. The physics of rare earth nickelates

epitaxial strain can tune the electronic correlations. Indeed, two important experimental studies of Ouelette et al. and Stewart et al. [54, 56] show an increase of the effective mass for tensile strain and a huge suppression of far and mid-infrared spectral weight which is transferred to frequencies beyond 3 eV. As seen in the section 2.3.2, the Hubbard U and Hund J interactions play an important role in the physical properties of these materials and suppress the low energy spectral weight. Most of the missing free carrier spectral weight is recovered in the oxygen 2p to nickel 3d transitions which span over approximately 10 eV [151]. Therefore, the mass-enhancement is due to strong electronic correlations. The increase of the $d_{x^2-y^2}$ band effective mass for tensile strain was also reported in the theoretical work of Nowadnick et al. [129] and also shows a decrease of the effective mass for the d_{z^2} band. Our optical study of LaNiO_3 thin films from extreme compressive to tensile strain, presented in chapter 3, adds to the understanding of the physics of these systems developed in previous studies focused on tensile strain, and elucidates the interplay between the lattice structure, electronic structure and electronic correlations.

From the first studies on nickelates, more precisely on NdNiO_3 , it was not clear whether the metal-insulator transition was driven by antiferromagnetic correlations, electron-electron or electron-phonon interactions [36, 87]. The antiferromagnetic origin of the band gap was quickly discarded when the separation of T_{MI} and T_N was observed on SmNiO_3 and EuNiO_3 [152]. A model based on correlations and strong lattice coupling, as presented in the last section, was progressively developed. The validity of the site selective Mott transition scenario is supported by the optical study of Ruppen et al. which show two interband transitions at approximately 0.5 and 1 eV in the optical conductivity of NdNiO_3 [62]. Their DMFT calculations show also that the bands just below the Fermi level have dominant LB character. The unoccupied band above the gap changes from dominantly LB (and thus Mott transition) to dominantly SB ("Mott-Peierls" regime) considering $U = 1$ eV or $U = 2$ eV in the calculations, respectively. The two experimental interband transitions are well captured by their calculations which assign one of the transitions to the excitation across the insulating gap, and the second excitation to optical transitions across the Peierls pseudogap. The comparison of the intensity and separation of the two peaks between experiment and calculations suggest that NdNiO_3 does not present Mott transition but may be more in the Mott-Peierls regime or in the crossover between the two regimes. These two peaks result directly from the bond disproportionation and are therefore absent in the metallic phase. By deepening the analyzes, they observed [70] that an extra spectral weight appears in both peaks below the Neel temperature indicating a reinforcement of the bond disproportionation in the antiferromagnetic order. Using a

phenomenological Landau model, they confirmed the positive feedback between antiferromagnetic and bond disproportionation order and concluded that the bond disproportionation is a *conditio sine qua non* to host the antiferromagnetic state. Furthermore, this Landau theory approach explains why strong hysteresis in resistivity or optical measurements is observed for nickelates whose metal-insulator and magnetic transitions occur simultaneously (PrNiO₃ and NdNiO₃), while no significant hysteresis is noticeable for the others (Sm to Lu).

2.4 Antiferromagnetic phase

Cooling to low temperatures, nickelates undergo a transition from a paramagnetic phase to antiferromagnetic order. While the metal-insulator and magnetic transition temperatures coincide for the neodymium and praseodymium nickelates, the Neel temperature splits from T_{MI} to lower and lower T_N as the rare earth radius decreases and the structural distortion increases. A magnetic moment of around $0.9 \mu_B$ on the nickel sites has been measured by neutron diffraction experiments on PrNiO₃ and NdNiO₃ [42, 153] and similar values were obtained for the other nickelates [43, 143, 154, 155]. Fits of the magnetic intensities from neutron diffraction data (models shown in Ref. [153]) support the picture that in YNiO₃, LuNiO₃ and HoNiO₃ there are two different magnetic moments: $1.4 \mu_B$ on the LB sites and about $0.7 \mu_B$ on SB sites [120, 143, 154].

While Guo et al. shows a new phase where antiferromagnetism occurs with metallic behaviour in single crystal of LaNiO₃ [156], others assert that the oxygen deficiency is the cause of this behaviour [6, 157, 158]. Liu reconciles both views and shows that lanthanum nickelate is close to an antiferromagnetic quantum critical phase transition.

For the other members of the nickelate family, a first approach to understand the mechanism of the antiferromagnetic order was to consider the superexchange interaction between the partially filled d orbitals of the nickel and the oxygen p orbitals. The p orbital has two antiparallel electrons which induce no magnetism. On each side of the oxygen, the nickel spin aligns antiparallel to the closest electron of the oxygen. The spins of the nickel ions should be antiferromagnetically ordered in a $\uparrow\downarrow\uparrow\downarrow$ configuration as shown in figure 2.15a. Considering the presence of both LB and SB nickel sites, the magnetic moment can have different intensity. However, neutron diffraction experiments reveal a magnetic propagation vector $(1/2, 0, 1/2)_n$ in the insulating monoclinic $P2_1/n$ phase [43, 44, 153–155, 159–161]. This propagation vector is written as $(1/4, 1/4, 1/4)_{pc}$ in the pseudocubic back-folding representation and as $(1/2, 0, 0)_c$ in the monoclinic $P2_1/c$ space

2. The physics of rare earth nickelates

group setting (see Fig. 2.10 in section 2.2.2). We saw in section 2.2.2 that antiferromagnetic order doubles the primitive unit cell $P2_1/c$ along \mathbf{a} and therefore 8 unit formula are required to describe the primitive unit cell of the magnetic state. In the $P2_1/n$ setting, which is not a primitive unit cell, the \mathbf{a} and \mathbf{c} axes have to be doubled to host the magnetic order and therefore gives the misleading impression that the unit cell has to be quadrupled, implying the need for 16 formula units. Actually, as described above, the antiferromagnetic propagation vector is already contained in the $P2_a2_1/c$ space group.

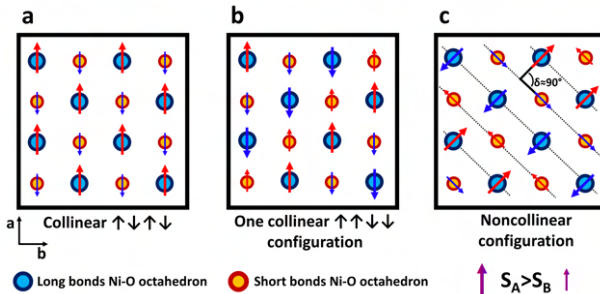


Figure 2.15: Possible antiferromagnetic configuration in the ab plane. Large blue and small red circles correspond to LB and SB nickel sites respectively. The spins are therefore unequal with $S_A > S_B$. **a**, Usual $\uparrow\downarrow\uparrow\downarrow$ antiferromagnetic order. **b**, One example of the collinear $\uparrow\uparrow\downarrow\downarrow$ antiferromagnetic structure. **c**, Noncollinear antiferromagnetic configuration. Angle between two adjacent spins is $\delta \sim 90^\circ$. Adapted from [48].

This experimentally observed magnetic propagation vector is not compatible with typical $\uparrow\downarrow\uparrow\downarrow$ antiferromagnetic configuration. The system requires that each nickel site is coupled ferromagnetically to three nearest neighbour nickel sites and coupled antiferromagnetically to the three remaining nearest neighbours. Moreover, the magnetic order is not associated with any orbital ordering, but it is a pure spin density wave [159]. The real spin configuration is still under debate between collinear arrangements $\uparrow\uparrow\downarrow\downarrow$ (one example shown in figure 2.15b) or noncollinear spin structure which consist of a $\sim 90^\circ$ spin spiral (Fig. 2.15c). Both configurations host spins of different sizes $S_A > S_B$ due to bond length disproportionation [153–155, 159–161]. Indeed, the intensity of the spin is directly correlated with the covalency of each site and therefore with the charge disproportionation.

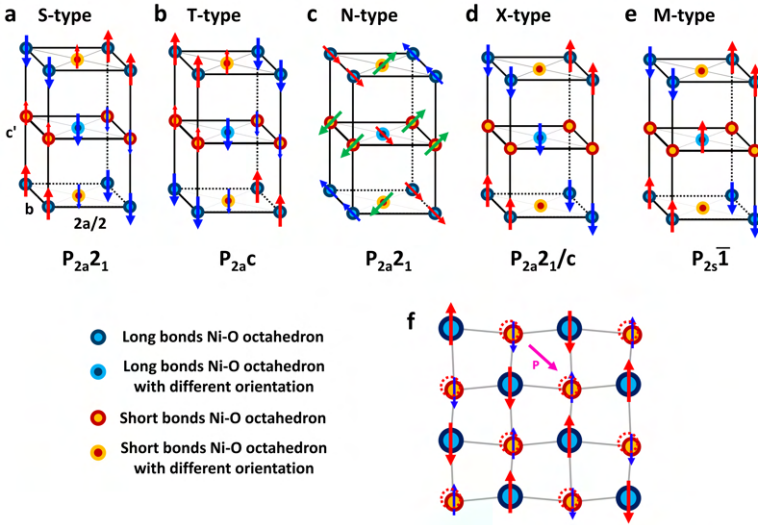


Figure 2.16: Magnetic structures for nickelates proposed by Giovannetti + less common X and M-types. Vertical axis is c' , and horizontal axes are b and $2a/2$ (which corresponds to half of the double axis a due to $T_a \rightarrow T_{2a}$ symmetry breaking in the antiferromagnetic phase). Blue and red circles are for LB and SB sites, respectively. Inverted colors of the circle correspond to the same octahedron but with different orientation (used later). **a**, Collinear S type magnetic order where the Ni spins form ferromagnetic zigzag chains within the ab plane which are pointing in the same direction for adjacent c planes. **b**, Collinear T type magnetic order where the Ni spins form ferromagnetic zigzag chains within the ab plane which are pointing in opposite directions for adjacent c planes. **c**, Noncollinear N type magnetic order where spins with same orientation are on planes perpendicular to $[1,0,1]$ and are parallel to this plane. From one plane to the other, the spins rotated $\sim 90^\circ$ forming a spin spiral as shown in figure 2.15c. **d**, $\uparrow 0 \downarrow 0$ X-type configuration. The spin in the middle of the structure is symmetrically related to the others. **e**, $\uparrow 0 \downarrow 0$ M-type configuration. The spin in the middle of the structure can have any orientation. **f**, First approach of probable ferroelectric polarization \mathbf{P} in the ab plane due to charge disproportionation and Ni-Ni bond lengths disproportionation induced by magnetic exchange-striction. Example for the collinear magnetic order from Fig. 2.15b and adapted from Ref. [47].

Giovannetti et al. propose three likely magnetic structures in their study [48]: S and T types which are collinear and N type which is noncollinear as shown in figure 2.16 **a**, **b** and **c**, respectively. While the nickel spins of the S -type form ferromagnetic zigzag chains within the ab plane (Fig. 2.16a) which are pointing in the same direction for adjacent layers, the T -type shows the same zigzag chains with the only difference that the chains point in opposite direction for adjacent layers (Fig. 2.16b). The $\uparrow\uparrow\downarrow\downarrow$ arrangement is observable along the c' axis. The N -type noncollinear antiferromagnetic order is defined as the noncollinear structure cited above. Spins with same

2. The physics of rare earth nickelates

orientation are positioned on planes perpendicular to $[1,0,1]$ and the spins are parallel to this plane. From one plane to the other, the spins rotate $\sim 90^\circ$ forming a spin spiral (Fig. 2.16c).

A possible but less common solution is the alternation between zero and finite magnetic moments in a $\uparrow 0 \downarrow 0$ configuration which would be consistent with the Park's extreme picture of $d^8 \underline{L} + d^8 \underline{L} \rightarrow d^8 + d^8 \underline{L}^2$ [122] assigning the $d^8 \underline{L}^2$ (Kondo-insulator) to the short bond nickel sites (with spin $S = 0$) and the d^8 (Mott-insulator) to the long bond nickel sites (with $S = 1$). Indeed, the two electrons from the oxygens which are very weakly spin-polarised confer a spin $S=0$ to the small nickel sites as explained in the previous section. Depending on the symmetry, the spin in the middle of the structure is symmetrically related to the others, or not, and we call them X-type (Fig.2.16d) and M-type (Fig.2.16e), respectively. From an energetic point of view, this situation is unlikely because the cost of several eV to suppress the magnetic moment for half of the Ni sites is high. However, various authors [120–125] propose this alternation of high-spin d^8 sites and low-spin $d^8 \underline{L}^2$ sites which is compatible with this picture. In figure 2.16, the space group of each magnetic arrangement is mentioned, and will be discussed in detail below.

Several theoretical studies assert that nickelates are type-II multiferroics. The first approach was to consider the inverse symmetry breaking induced by the $\uparrow\uparrow\downarrow\downarrow$ antiferromagnetic order. Indeed, two neighbouring Ni sites with antiparallel spins have longer bonds than neighbouring sites with parallel spins due to magnetic exchange-striction [46, 47, 162]. It has been proposed that the combination of bond length disproportionation between nickel sites together with their charge disproportionation could induce a ferroelectric polarization in the ab plane as shown in figure 2.16f (example for a collinear magnetic order). The three magnetic structures proposed by Giovannetti et al. are multiferroics and the polarization is oriented along \mathbf{b} for the S-type and in the ac plane for the T and N-type magnetic order. They explain the mechanism of the ferroelectric polarization as follows: Due to the Pauli exclusion principle, oxygen sites become inequivalent with different Born effective charges [48] depending on the nickel sites between which they are located. Indeed, due to Pauli principle, the regions between two nickel sites with aligned spins have a low electronic density, while the regions between two nickel sites with opposite spins have higher electronic density as illustrated in figure 2.17 by red and blue shading respectively. In other words, exchange-correlation causes electron-depletion (accumulation) between Ni-neighbors of parallel (antiparallel) spin.

Figure 2.17 illustrates four planes for the S and T-type magnetic order. LB and SB nickel sites are represented by red and blue color, respectively. \uparrow or \downarrow spins are characterized by full or empty colored circle. As explained

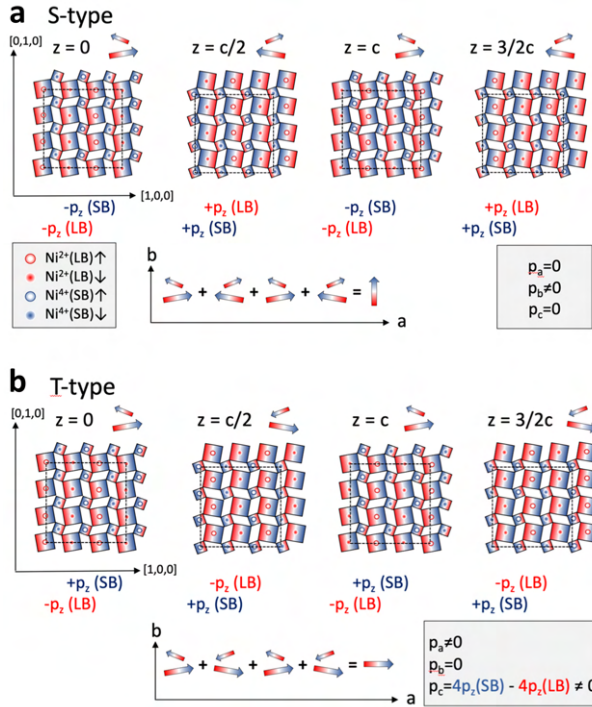


Figure 2.17: Spontaneous polarization for S and T-type magnetic order. Each plane along c is investigated to obtain the total polarization. LB and SB Nickel sites are represented by red and blue color respectively. \uparrow or \downarrow spins are characterized by full and empty colored circle. Red and blue spread color represent electron depletion and accumulation respectively, induced by exchange-correlation. Two-color arrows on the top of each plane summarize the total polar moment for the plane of interest. The polarization of each plane is summed to get the total polarization of the antiferromagnetic order. **a**, S-type antiferromagnetic order. Total polarization is along **b**. **b**, T-type antiferromagnetic order. Total polarization lies in the ac plane.

above, the region between Ni-neighbors of parallel (antiparallel) spins has lower (higher) electronic density. This results in polar moments at each nickel site due to these spatial variations in electronic density which can be summarized by the two-color arrows on the top of each plane. The two inequivalent LB and SB nickel sites host two inequivalent charges (in the extreme case Ni^{2+} and Ni^{4+} as seen in the last section). The intensity of polar moments depends therefore on the nickel sites considered, which is why the two-color arrows have different lengths. Summing up these polar moments for all the four planes (bottom part of figures 2.17a and b) reveals a spontaneous polarization for S, T and N types, even if for N-type the

2. The physics of rare earth nickelates

mechanism is different (relativistic spin-orbit coupling directly causes the polarization [48] but will not be explained in this work). While the S -type reveals a polarization along \mathbf{b} , the T and N types show a polarization along the ac plane. The polarization is large for S and T types, mostly along \mathbf{a} for the T type, weak and mostly along \mathbf{c} for the N -type.

Perez-Matoz et al. predict, also from the crystal symmetry and the magnetic propagation vector, the existence of ferroelectricity induced by magnetism [51]. In the study, they focus on the transition from $P2_1/n$ to $P2_1a2_1$ which implies a spontaneous polarization along \mathbf{b} for the collinear magnetic structure below T_N . They conclude that the polarization should act as a force on the ions, deforming the lattice and pushing the Ni-ions away from centrosymmetric positions. Therefore the displacement of the nickel atoms, having broken the inversion symmetry, may be detected by optical methods as it removes parity selection rules. More details will be given in chapter 4.

It is now instructive to determine which magnetic space group presented in the section 2.2.2 can host each mentioned magnetic configuration. We start from the $P2_1/n$ space group in figure 2.10c which is reproduced in figure 2.18a, by specifying the LB and SB nickel sites as well as their orientations, to check the symmetries. The LB and SB nickel sites are differentiated by red and blue colors, respectively, while two same octahedra but with different orientation are differentiated by inverted colors. The sites are denoted by p, q, u, v and negative letters (for example $-p$) means opposite spin. The orientation of a spin is described by $\mathbf{x} = [x_1, x_2, x_3]$ and its corresponding site is x .

To determine the possible screw axis and n -glide plane operations of each structure, examples are shown in figures 2.18b and c, respectively. For the unprimed screw axis operation, ① the site p turns 180° around one of the green axis (spin components x_1 and x_3 are invert) and reaches p' , ② it translates by $b/2$ along \mathbf{b} and reaches q . In this case, the spin does not respect the time reversal symmetry. For the primed screw axis, the structure turn around one of the blue axis, translates by $b/2$ along \mathbf{b} , and the spin respects the time reversal symmetry (spin $\mathbf{x} \rightarrow -\mathbf{x}$). For the unprimed n -glide plane, ① the site p is reflected through the purple plane (spin components x_1 and x_3 are invert) and reaches p' , and ② is translated by $(c' + a)/2$ along $\mathbf{c}' + \mathbf{a}$ represented by a purple arrow (which is $c/2$ along \mathbf{c} in the $P2_1/c$ representation) and reaches q . In the case of the primed n -glide plane, the mirror operation is the same but the translation ② is $(\mathbf{c}' - \mathbf{a})/2$ to reach $-q$ (yellow arrow Fig. 2.18b) and the spin respect the time inversion symmetry.

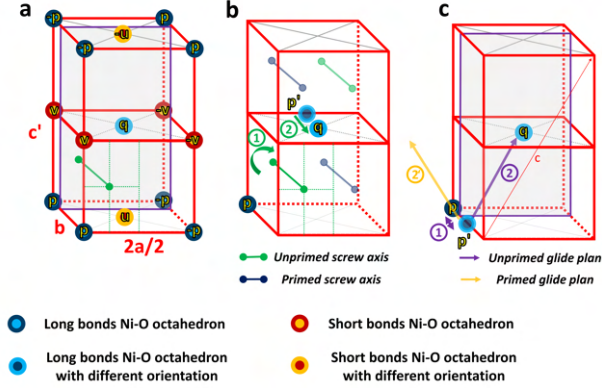


Figure 2.18: **a**, Illustration of the $P2_1/n$ space group taking into account LB and SB nickel sites differentiated by red and blue colors respectively, and different orientation for the same octahedron are differentiated by inverted colors. The sites are noted by p, q, u and v and negative letters (for example $-p$) means opposite spin. The orientation of the spin is described by $\mathbf{x} = [x_1, x_2, x_3]$. **b**, Screw axis 2_1 operation symmetry. ①, The site p rotates 180° around the green axis $[0,1,0]$. ②, it translates by $b/2$ along \mathbf{b} . There are two green unprimed 2_1 screw axis (no time reversal symmetry) and two blue primed $2'_1$ screw axis (time reversal symmetry). **c**, n -glide plane operation symmetry. Unprimed n -glide plane: ①, The site is reflected through the mirror delimited by purple lines (no time inversion symmetry). ② it is translated by $(c' + a)/2$ along $\mathbf{c}' + \mathbf{a}$ represented by purple arrow (which is $c/2$ along \mathbf{c} in the $P2_1/c$ representation). Primed n -glide plane: ① Same mirror operation symmetry. ② translation of $(c' - \mathbf{a})/2$ (yellow arrow) (time inversion symmetry).

We check one by one the possible magnetic configurations as a function of the lattice structure. We show the symmetry operation for p and u nickel sites.

- $P_{2a}2_1/c$ has $T_{2a}(= 2 \text{ times } T_a)$, screw axis 2_1 and c -glide plane symmetry operations. Spin on a p site, after unprimed screw axis or glide plane operation, has inverse x_1 and x_3 components and is located at the q site. Spin on a u site, after unprimed screw axis or glide plane operation, has inverse x_1 and x_3 components, but is located at the v or $-v$ site respectively.

Unprimed screw axis:	\Rightarrow	$\mathbf{p} = [p_1, p_2, p_3]$
$\mathbf{p} = [p_1, p_2, p_3] \rightarrow \mathbf{q} = [-p_1, p_2, -p_3]$		$\mathbf{q} = [-p_1, p_2, -p_3]$
$\mathbf{u} = [u_1, u_2, u_3] \rightarrow \mathbf{v} = [-u_1, u_2, -u_3]$		$\mathbf{u} = [0, 0, 0]$
		$\mathbf{v} = [0, 0, 0]$
Unprimed c-glide plane		
$\mathbf{p} = [p_1, p_2, p_3] \rightarrow \mathbf{q} = [-p_1, p_2, -p_3]$		Only p and q sites
$\mathbf{u} = [u_1, u_2, u_3] \rightarrow -\mathbf{v} = [-u_1, u_2, -u_3]$		have magnetic moment

2. The physics of rare earth nickelates

- $P_{2s}\bar{1}$ has T_{2s} (**a**, **b** or **c** axis are doubled, with no privileged direction) and inversion $\bar{1}$ symmetry operation. Unprimed inversion symmetry around q causes $p \rightarrow p$, $q \rightarrow q$ $v \rightarrow -v$ and $u \rightarrow -u$. Primed inversion symmetry around u results in $p \rightarrow -(-p)$, $q \rightarrow -(-q)$ $v \rightarrow -(v)$ and $u \rightarrow u$.

Unprimed inversion around q:	\Rightarrow	$\mathbf{p} = [p_1, p_2, p_3]$
$\mathbf{p} = \mathbf{p} \quad ; \quad \mathbf{q} = \mathbf{q}$		$\mathbf{q} = [q_1, q_2, q_3]$
$\mathbf{v} = -\mathbf{v} \quad ; \quad \mathbf{u} = -\mathbf{u}$		$\mathbf{u} = [0, 0, 0]$
		$\mathbf{v} = [0, 0, 0]$
Primed inversion around u		Only p and q sites
$\mathbf{p} = -(-\mathbf{p}) \quad ; \quad \mathbf{q} = -(-\mathbf{q})$		have magnetic moment
$\mathbf{u} = \mathbf{u} \quad ; \quad \mathbf{v} = -(\mathbf{v})$		

- $P_{2a}c$ has T_{2a} and c -glide plane symmetry operations. Spin on a p site, after unprimed c -glide plane operation, has inverse x_1 and x_3 components and is located at the q site. Spin on a u site, after unprimed c -glide plane operation, has inverse x_1 and x_3 components, and is located at the $-v$ site. Spin on a p site, after primed glide plane operation, has inverse x_2 component and is located at the $-q$ site. Spin on a u site, after primed glide plane symmetry, has inverse x_2 components, and is located at the v site.

Unprimed c-glide plane:	\Rightarrow	$\mathbf{p} = [p_1, p_2, p_3] \rightarrow \mathbf{q} = [-p_1, p_2, -p_3]$
$\mathbf{u} = [u_1, u_2, u_3] \rightarrow -\mathbf{v} = [-u_1, u_2, -u_3]$		$\mathbf{q} = [-p_1, p_2, -p_3]$
		$\mathbf{u} = [u_1, u_2, u_3]$
primed c-glide plane		$\mathbf{v} = [u_1, -u_2, u_3]$
$\mathbf{p} = [p_1, p_2, p_3] \rightarrow -\mathbf{q} = [p_1, -p_2, p_3]$		
$\mathbf{u} = [u_1, u_2, u_3] \rightarrow \mathbf{v} = [u_1, -u_2, u_3]$		

- $P_{2a}2_1$ has T'_a and screw axis 2_1 symmetries. Spin on a p site, after unprimed screw axis operation, has inverse x_1 and x_3 components and is located at the q site. Spin on a u site, after unprimed screw axis operation, has inverse x_1 and x_3 components, and is located at the v site. Spin on a $-p$ site, after primed screw axis, has inverse x_2 components and is located at the q site. Spin on a u site, after primed screw axis, has inverse x_2 components, and is located at the $-v$ site.

Unprimed screw axis:		\Rightarrow	$\mathbf{p} = [p_1, p_2, p_3]$ $\mathbf{q} = [-p_1, p_2, -p_3]$ $\mathbf{u} = [u_1, u_2, u_3]$ $\mathbf{v} = [-u_1, u_2, -u_3]$
$\mathbf{p} = [p_1, p_2, p_3] \rightarrow \mathbf{q} = [-p_1, p_2, -p_3]$			
$\mathbf{u} = [u_1, u_2, u_3] \rightarrow \mathbf{v} = [-u_1, u_2, -u_3]$			
primed screw axis			
$-\mathbf{p} = [-p_1, -p_2, -p_3] \rightarrow \mathbf{q} = [-p_1, p_2, -p_3]$			
$\mathbf{u} = [u_1, u_2, u_3] \rightarrow -\mathbf{v} = [u_1, -u_2, u_3]$			

The highest magnetic symmetry is for the monoclinic structure with space group $P_{2a}2_1/c$. This structure hosts only magnetic moments on p and q sites ($\uparrow 0 \downarrow 0$) with symmetry relation between p and q . This space group can host the X-type magnetic configuration. Lowering the symmetry by breaking 2_1 screw axis or c -glide plane symmetries leads to two monoclinic structure with $P_{2a}c$ and $P_{2a}2_1$ space groups, respectively. By breaking 2_1 screw axis and c -glide plane simultaneously leads to the triclinic structure with $P_{2s}\bar{1}$ space group. The $P_{2s}\bar{1}$ space group also only hosts magnetic moments on p and q sites, but there is no symmetry relation between p and q . This space group can host the M-type magnetic configuration. The symmetry conditions developed above show that $P_{2a}2_1$ space group can host S and N types antiferromagnetic order, while $P_{2a}c$ space group hosts T -type configuration. $P_{2a}2_1$ and $P_{2a}c$ space group break the inversion symmetry operation $\bar{1}$, while $P_{2a}2_1/c$ and $P_{2s}\bar{1}$ space groups preserve it. Lowering the symmetry by breaking the last symmetry operations (c -glide plane, screw axis or $\bar{1}$ from $P_{2a}c$, $P_{2a}2_1$ and $P_{2s}\bar{1}$ respectively), leads to the $P_{2s}1$ space group which can host any type of order. Table 2.9 summarizes the magnetic arrangements and their space groups.

Space group:	Magnetic configuration	Inversion $\bar{1}$	Multiferroic
$P_{2a}2_1/c$	X-type ($\uparrow 0 \downarrow 0$)	yes	no
$P_{2a}c$	T-type ($\uparrow\uparrow\downarrow\downarrow$)	no	yes
$P_{2a}2_1$	S-type ($\uparrow\uparrow\downarrow\downarrow$) and N-type (noncollinear)	no	yes
$P_{2s}\bar{1}$	M-type ($\uparrow 0 \downarrow 0$)	yes	no
$P_{2s}1$	any type	no	no

Table 2.9: Summary of the magnetic configurations and their crystal space groups.

CHAPTER 3

Optical properties of LaNiO_3 films tuned from compressive to tensile strain.

In this chapter, we report the impact of highly compressive to moderate tensile strain on the structural and electronic properties of LaNiO_3 thin films using a combination of optical measurements and DFT calculations. We connect the changes in the optical conductivity with the evolution of structure, correlation effects and fermi surface characteristics as a function of strain. This chapter has been adopted with small modifications from Physical Review B 102, 155148 (2020), I.Ardizzone, M.Zingl, J.Teyssier, H.U.R.Strand, O.Peil, J.Fowlie, A.B.Georgescu, S.Catalano, N.Bachar, A.B.Kuzmenko, M.Gibert, J.-M.Triscone, A.Georges, D.van der Marel [82]. It starts with a general introduction on optical spectroscopy. The expression of the optical conductivity as well as the different Drude-Lorentz models will be presented in the context of the data analysis used in this work. Then we describe the measured samples as well as the different optical spectroscopy techniques that were combined to obtain wide-range optical conductivity spectra. The experimentally determined optical conductivities will be compared to DFT calculations and the evolution of the free carrier spectral weight, the effective mass and the Fermi surface as a function of strain will be discussed in detail.

3.1 Introduction

As seen in the section 2.2, tensile and compressive strain decrease the metal-insulator transition temperature T_{MI} of NdNiO_3 thin films compared to bulk measurement on powders and single crystals and therefore stabilise the metallic phase. For tensile strain, the transition is broader but the hysteresis is narrow. For compressive strain, the transition is sharp but may be completely suppressed for highly compressive strain. Similar behaviour was observed for SmNiO_3 thin films. LaNiO_3 bulk is exceptional in this class of materials because it is metallic at all temperatures and motivated us to study the role of strain on the evolution of the lattice structure, electronic structure and electronic correlations of this particular compound. Two previous optical studies of strained LaNiO_3 films have revealed the impact of strain on the optical conductivity and on the enhancement of the electron mass [54, 56]. Both studies report that the films subject to tensile strain (LaNiO_3 on SrTiO_3 or on DyScO_3) are more strongly correlated than the film with moderate compressive strain (LaNiO_3 on LaAlO_3). This result is supported by high resolution angle-resolved photoemission spectroscopy and DFT+DMFT calculations [129]. However, no study reports the effect of more compressive strain on the lattice and electronic structures of LaNiO_3 thin films. In this study, we extend the range of applied strain from highly compressive (-3.34%) to moderate tensile (+1.75%) strain with several intermediate strain levels and measure the optical response of the films on a large frequency range, from around 1 meV to 4 eV. We perform DFT calculations taking into account the effect of strain on the lattice structure and we obtain values of the free carrier mass enhancement that are consistent with the aforementioned reports. We relate also changes in the Fermi surface topology of LaNiO_3 for both compressive and tensile strain, revealing strain-dependent Lifshitz transition which have been previously seen in angle resolved photoemission (ARPES) experiments [150]. We demonstrate that these transitions have a pronounced effect on the velocities of Fermi surface states that control the low-frequency conductivity.

3.2 Optical spectroscopy theory

Optical spectroscopy uses light to investigate the electronic, structural and magnetic properties of materials and can probe a very broad variety of excitations.

While the optical conductivity ($\sigma(\omega) = \sigma_1(\omega) + i\sigma_2(\omega)$) represents all the dipole active modes and can be probed from direct electronic transitions, the Raman susceptibility ($\chi(\omega) = \chi'(\omega) + i\chi''(\omega)$) expresses the excitations which change the polarizability (Raman active mode) of the material. The latter

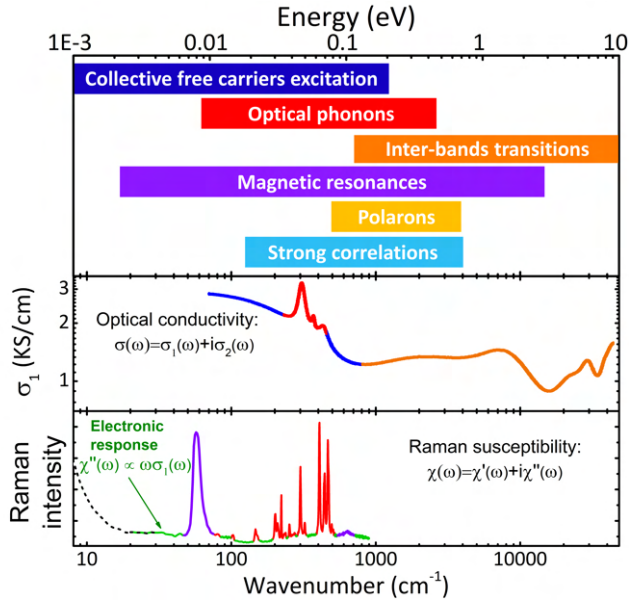


Figure 3.1: **a**, Energy scales of possible excitations in transition metal oxides and correlated metals. Adapted from [151]. **b**, Optical conductivity of LaNiO₃ thin film on SrTiO₃ [56]. **c** Raman intensity of NdNiO₃ single crystal.

is an indirect excitation process which involves the scattering of electrons over the system. These two optical quantities are therefore complementary. For transition metal oxides (TMO) and correlated metal, the following excitations are likely: Collective free carriers excitation, optical phonons (collective vibrations of the lattice), inter-bands transitions (transitions of electrons from one band to another), magnetic resonances (collective excitations of spins) and polarons (coupling between electron and lattice). The energy scale of these excitations is shown in figure 3.1a. Some of these excitations are visible in the real part of the optical conductivity $\sigma_1(\omega)$ as shown in figure 3.1b for LaNiO₃ on SrTiO₃ [56], while other excitations are visible in Raman intensity as shown in figure 3.1c for a NdNiO₃ single crystal. The colors correspond to the excitations mentioned in figure 3.1a. Optical selection rules, which are described in the section 3.2.4, indicate if an excitation is dipole active or not. For this study, we use and combine various optical spectroscopy techniques to obtain the optical conductivity of LaNiO₃ thin films. The beginning of this chapter is dedicated to define this quantity (sections 3.2.1-3.2.3), while the spectroscopic techniques are described in the section 3.3. The Raman susceptibility as well as Raman measurement are described in the chapter 4.

3. Optical properties of LaNiO_3 films tuned from compressive to tensile strain.

3.2.1 Maxwell equations, dielectric function ϵ and optical conductivity σ

The interaction between light and matter is described from a classical point of view by the Maxwell equations in matter defined as:

$$\nabla \cdot \mathbf{D}(\mathbf{r}, t) = 4\pi\rho_{ext}(\mathbf{r}, t) \quad (3.1)$$

$$\nabla \cdot \mathbf{B}(\mathbf{r}, t) = 0 \quad (3.2)$$

$$\nabla \times \mathbf{E}(\mathbf{r}, t) = -\frac{1}{c} \frac{\partial \mathbf{B}(\mathbf{r}, t)}{\partial t} \quad (3.3)$$

$$\nabla \times \mathbf{H}(\mathbf{r}, t) = -\frac{1}{c} \frac{\partial \mathbf{D}(\mathbf{r}, t)}{\partial t} + \frac{4\pi}{c} \mathbf{J}_c(\mathbf{r}, t) \quad (3.4)$$

Where \mathbf{D} , \mathbf{B} , \mathbf{E} and \mathbf{H} are the electric displacement, the magnetic induction, the electric field and the magnetic field respectively, while ρ_{ext} and \mathbf{J}_c are the additional external charge and the current induced by the electric field respectively. From linear response theory, the current \mathbf{J}_c is directly related to the electric field \mathbf{E} by the real part of the complex optical conductivity σ . Moreover, \mathbf{D} is proportional to \mathbf{E} , and \mathbf{B} is proportional to \mathbf{H} by the real part of the complex dielectric function ϵ and the real part of the permeability μ respectively.

$$\mathbf{J}_c = \sigma_1 \mathbf{E} \quad (3.5)$$

$$\mathbf{D} = \epsilon_1 \mathbf{E} = \mathbf{E} + 4\pi \mathbf{P} \quad (3.6)$$

$$\mathbf{B} = \mu_1 \mathbf{H} = \mathbf{H} + 4\pi \mathbf{M} \quad (3.7)$$

With \mathbf{P} the electric polarization and \mathbf{M} the magnetization. We introduce the complex refractive index N defined as:

$$N(\omega) = n(\omega) + i\kappa(\omega) \quad (3.8)$$

where n is called refractive index and κ is the extinction coefficient that describes the absorption of light during its propagation.

For homogeneous and isotropic materials we get the complex dielectric function:

$$\epsilon = \epsilon_1 + i\epsilon_2 = \frac{N^2}{\mu_1} = \frac{n^2 - \kappa^2}{\mu_1} + i \frac{2n\kappa}{\mu_1} = \epsilon_1 + \frac{i4\pi\sigma_1}{\omega} = 1 + \frac{i4\pi}{\omega} \sigma \quad (3.9)$$

Where we define $\sigma = \sigma_1 + i\sigma_2$ the complex optical conductivity which is related to the total current (polarization current, bound current and conductive current) by $\mathbf{J}_{tot} = \sigma \mathbf{E}$.

3.2.2 General expression for the optical conductivity of a many-body correlated electron system

Using a Hamiltonian \hat{H} that takes into account a periodic potential and interacting particles (Coulomb potential), the relation $\hat{\mathbf{j}} = q_e \hat{\mathbf{v}}_q = -\frac{\partial \hat{H}}{\partial \mathbf{A}_{-q}}$ with \mathbf{A} the vector potential, gives a general expression for the optical conductivity:

$$\sigma(q, \omega) = i \frac{nq_e^2}{m\omega} + i \frac{\chi_{jj}(q, \omega)}{\omega} \quad (3.10)$$

where the first term corresponds to the diamagnetic contribution and the second term is the "regular" contribution taking into account crystal potential and electronic correlations. χ_{jj} , the current-current susceptibility, is defined in this case as:

$$\chi_{jj}(\omega) = \sum_{n,m} (p_n - p_m) \frac{|\langle n | \hat{\mathbf{j}}^{(r)} | m \rangle|^2}{\omega + E_n - E_m + i\delta} \quad (3.11)$$

With E_n and E_m two different energy levels of the many-body quantum states $|n\rangle$ and $|m\rangle$ respectively, $p_n = \frac{e^{-\frac{E_n}{k_B T}}}{Z}$ the statistical probability of occurrence of the many-body quantum state $|n\rangle$ and $Z = \sum_n e^{-\frac{E_n}{k_B T}}$ the partition function. The real part of the optical conductivity can be deduced from the current-current susceptibility by $\sigma_1(\omega) = -\frac{1}{\omega} \text{Im} \chi_{jj}(\omega)$ which gives:

$$\sigma_1(\omega) = \frac{\pi(1 - e^{-\beta\omega})}{\omega} \sum_{n,m} \frac{e^{-\beta E_n}}{Z} |\langle n | \hat{\mathbf{j}}^{(r)} | m \rangle|^2 \delta(\omega + E_n - E_m) \quad (3.12)$$

This expression shows that the spectrum of σ_1 consists of a series of peaks which represent excitations of energy $\Delta E = E_m - E_n$ from the ground state $|n\rangle$ to excited many-body states $|m\rangle$. While delta peaks describe the excitations of atoms and molecules, the excitation peaks broaden in solids due to the appearance of electronic bands.

From equation 3.11, it is possible to rewrite equation 3.10 combining the two terms in a single one and having the same sign for all poles including the one in the origin. The general expression for the complex optical conductivity tensor is given by:

$$\sigma(\omega) = \frac{2}{\Omega} \sum_{\alpha,\beta} \frac{p_\alpha \langle \alpha | \hat{\mathbf{j}} | \beta \rangle \langle \beta | \hat{\mathbf{j}} | \alpha \rangle}{E_\beta - E_\alpha} \frac{i\omega}{\omega(\omega + i\delta) - (E_\beta - E_\alpha)^2} \quad (3.13)$$

3. Optical properties of LaNiO_3 films tuned from compressive to tensile strain.

with Ω the volume of the system and $|\alpha\rangle$ and $|\beta\rangle$ are two many-body eigenstates of the system. The complete development and more details can be found in the lecture notes *Introduction to Correlated Matter* of Dirk van der Marel [163].

3.2.3 Specific expression for optical conductivity of interband transitions

The general formula for optical conductivity given by equation 3.13 takes into account the lattice potential and electron-electron correlations. However, the eigenstates $|\alpha\rangle$ and $|\beta\rangle$ are many body states and are difficult to compute. From the optical spectrum of an insulating material, the excitation can be described, to a first approximation, as the excitation of an electron-hole pair, with the hole on the j band just below the gap, and the electron in the m band above the gap (more details in van der Marel lecture notes [163]). For optical measurement, we consider the momentum of the phonon $q \rightarrow 0$ and we can take the limit $\mathbf{k} \rightarrow \mathbf{k}'$. After these assumptions and summing over all combinations, the optical conductivity of non-interacting electrons in a multi-band system is:

$$\sigma(\omega) = \frac{1}{\Omega} \sum_{\mathbf{k}, j, m}^{1^{st} BZ} \lim_{\mathbf{k}' \rightarrow \mathbf{k}} W_{j, m}(\mathbf{k}, \mathbf{k}') \frac{i\omega}{\omega(\omega + i\delta) - (\epsilon_{\mathbf{k}', m} - \epsilon_{\mathbf{k}, j})^2} \quad (3.14)$$

with:

$$W_{j, m}(\mathbf{k}, \mathbf{k}') \equiv \langle \mathbf{k}, j | \hat{\mathbf{j}} | \mathbf{k}', m \rangle \langle \mathbf{k}', m | \hat{\mathbf{j}} | \mathbf{k}, j \rangle \frac{f_{\mathbf{k}, j} - f_{\mathbf{k}', m}}{\epsilon_{\mathbf{k}', m} - \epsilon_{\mathbf{k}, j}} \quad (3.15)$$

Where j and m are two different bands, $\hat{\mathbf{j}}$ the current operator and f the Fermi-Dirac distribution.

Using the same band approach, it is possible to rearrange the terms of equation 3.13 neglecting electron-hole interactions (vertex correction) to obtain:

$$\begin{aligned} \sigma_1(\omega) &= \frac{\pi^2}{\Omega} \int d\omega' \sum_{\mathbf{k}; j, m} \frac{f(\omega') - f(\omega' + \omega)}{\omega} \\ &\times \mathbf{j}_{j, m}^*(\mathbf{k}) \mathbf{j}_{j, m}(\mathbf{k}) A(\mathbf{k}, m; \omega' + \omega) A(\mathbf{k}, j; \omega') \end{aligned} \quad (3.16)$$

which is the expression of the real part of the optical conductivity

describing the excitation of an electron-hole pair induced by the absorption of a photon. A is the total (electron+hole) spectral function defined as:

$$\begin{aligned}
 A(\mathbf{k}, j; \omega) &= A_e(\mathbf{k}, j; \omega) + A_h(\mathbf{k}, j; \omega) \\
 &= -\frac{1}{\pi} \text{Im} \frac{1}{\omega - \epsilon_{\mathbf{k}, j} + \mu - \Sigma(\mathbf{k}, j; \omega) - i\delta}
 \end{aligned}
 \tag{3.17}$$

with Σ the self energy.

The spectrum consists of a series of excitations which are broadened into bands by the imaginary part of Σ and shift by the real part of Σ which is related to the effective mass m^* of electrons.

3.2.4 Optical selection rules

The possible transition of a system from an initial quantum state $|i\rangle$ to a final quantum state $|f\rangle$ is given by the selection rules. In a general sense, the propagator $\int \Psi_i^* m \Psi_f dt$, with m the transition moment operator, defines the probability that the system passes from a state Ψ_i to Ψ_f . If the integral is zero, the transition is forbidden, if not, the transition is allowed. In the case of electronic transition (electric dipole transition) the integral of the propagator can be summarized in two rules that are presented at the bottom of figure 3.2a.

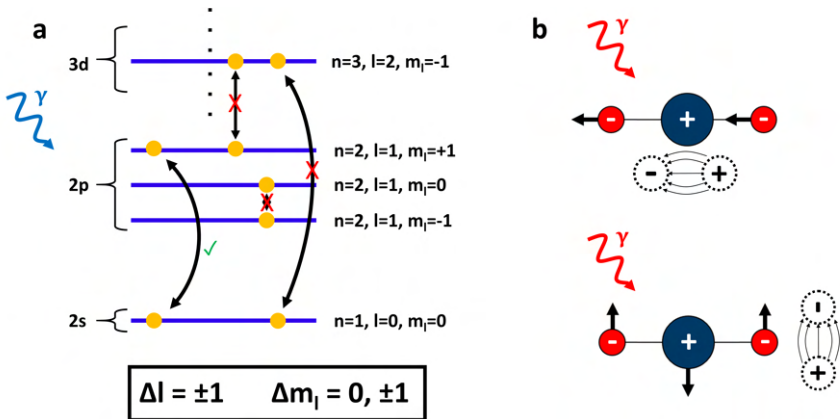


Figure 3.2: a, Summary of the selection rules for electric dipole transition. Illustration of allowed and forbidden transitions. b, Two vibrational excitations which induces an electric dipole moment through the molecule (odd parity) and are infrared active.

3. Optical properties of LaNiO_3 films tuned from compressive to tensile strain.

The first rule tells us that the change in the orbital quantum number during the transition should be either +1 or -1. The second rule states that the change in magnetic quantum number during the transition should be either 0, +1 or -1. It follows that some inter-band transitions are allowed while others are forbidden as the examples in Fig. 3.2a. Concerning vibrational excitations, an incoming light can be absorbed by a vibrational Q mode if the absorption changes the dipole moment μ of the molecule $\frac{\partial \mu}{\partial Q} \neq 0$. This vibration is called polar. Figure 3.2b shows the absorption of a photon by collective vibrations where the displacements of the red atoms induce an electric dipole moment.

3.2.5 Drude-Lorentz and extended Drude models

Despite some simplifications, the computation of the optical conductivity can be very cumbersome and not very convenient to provide an optical model. Fortunately, Paul Drude proposed in 1900 a theory that describes more simply the dynamics of electrons inside a metal. His model is based on several assumptions, two of them should be kept in mind:

- The density of free carriers is a gas which satisfies the kinetic theory of gas.
- The "collisions" between electrons and ions are instantaneous and the time between two of them is defined as the relaxation time τ . The scattering rate is defined by $1/\tau$. There is no electron-electron interaction.

A simple derivation from the complete assumptions [164] gives first of all the static conductivity:

$$\sigma(\omega = 0) = \sigma_0 = \sigma_{DC} = \frac{ne^2\tau}{m_e} \quad (3.18)$$

with n the electrons density. Using the average electrons momentum, the complex and frequency dependent optical conductivity is defined as:

$$\sigma(\omega) = \frac{\sigma_0}{1 - i\omega\tau} = \frac{\sigma_0}{1 + \omega^2\tau^2} + i\frac{\sigma_0}{1 + \omega^2\tau^2}\omega\tau \quad (3.19)$$

In this model, we can define the plasma frequency ω_p in equation 3.20 which defines the period of oscillation of the electronic gas around the equilibrium position due to the Coulomb attraction with the positive charges. Note that, in the case of metal, the real part of ϵ is negative below the plasma frequency and an electromagnetic field reaching the material with a frequency $\omega < \omega_p$ is completely reflected while for a frequency $\omega > \omega_p$, the wave can propagate in the material.

$$\omega_p^2 = \frac{4\pi n e^2}{m_e} \quad (3.20)$$

Note also that, by virtue of f-sum rule, the integration of $\sigma_1(\omega)$ from 0 to ∞ gives the number of electrons per formula unit and is related to the plasma frequency by : $\int_0^\infty \sigma_1(\omega) d\omega = \frac{\omega_p^2}{8}$. From equations 3.18 to 3.20 it is possible to rewrite the optical conductivity in a new form useful for the following part:

$$\sigma(\omega) = \frac{1}{4\pi} \frac{\omega_p^2 \tau}{1 - i\omega\tau} \quad (3.21)$$

The Drude model is a simple way to describe the motion of electrons inside metals and approximates well the optical conductivity of gold, silver, or aluminum [138, 139]. The low frequency of σ_1 is characterized by a Lorentzian centred at 0, called Drude peak, which represents the contribution of free carriers (Fig 3.3a). The scattering rate ($1/\tau$) of the Drude peak is constant. To model higher energy modes such as phonons, magnons or inter-bands transitions, we use Lorentzian functions considering that these excitations can be treated as classical harmonic oscillators. The complete optical conductivity therefore consists of the sum of Lorentzian functions:

$$\sigma(\omega) = \sum_j \frac{\omega_{pj}^2}{4\pi} \frac{i\omega}{\omega^2 - \omega_{0j}^2 + i\omega \frac{1}{\tau_j}} \quad (3.22)$$

With ω_{0j} , ω_{pj} and $\frac{1}{\tau_j}$, the position, the spectral weight and the width of the j-th Lorentz oscillator respectively. Note that these Lorentzian functions take into account time inversion symmetry as well as the fact that if no electric field is applied, the system has to be in equilibrium and no current should flow in the material. For $\omega_0 = 0$, we retrieve the equation 3.21. One extra contribution of all the very high energy modes should also added (called ϵ_∞ in the modelling of $\epsilon(\omega)$).

However, the Drude model (equation 3.21) takes only into account the interactions of electrons with impurities or defects. When electrons interact with each other or with bosons an energy dependent scattering rate has to be considered. These low energy interactions can be the electronic correlations discussed in the section 2.3.2. To model this type of interactions, Götze and Wölfle proposed in 1972 [140] to change the constant scattering rate $1/\tau$ by a complex and frequency dependent scattering rate $M(\omega)$ called Memory function $1/\tau \rightarrow -iM(\omega)$ with $M(\omega) = M_1(\omega) + iM_2(\omega) = (\frac{m^*(\omega)}{m} - 1)\omega + i\frac{1}{\tau(\omega)}$. The imaginary part defines the energy-dependent scattering rate while the real part is related to the effective mass m^* , which defines the renormalization of the mass due to interactions. Note that the effective mass is also

3. Optical properties of LaNiO_3 films tuned from compressive to tensile strain.

frequency-dependent. This model is called the extended Drude model. The new optical conductivity is defined as:

$$\sigma(\omega) = \frac{1}{4\pi} \frac{i\omega_p^2}{\omega + M(\omega)} \quad (3.23)$$

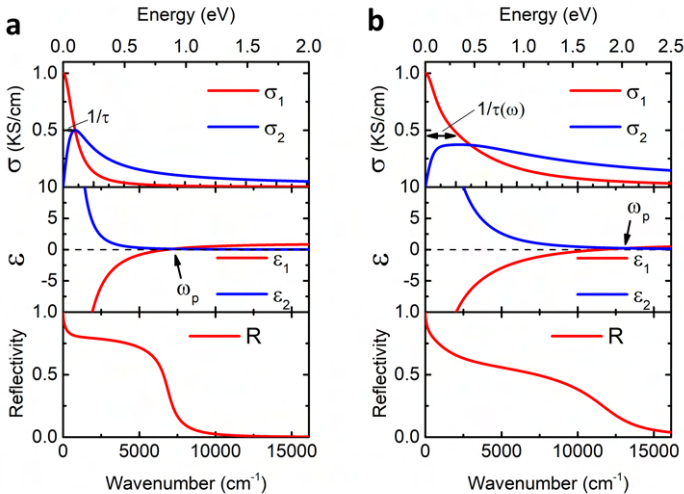


Figure 3.3: **a**, (top) Real and imaginary parts (σ_1 and σ_2) of the optical conductivity of a metal ($\gamma = 1/\tau \approx 800\text{cm}^{-1}$). (Middle) Real and imaginary parts (ϵ_1 and ϵ_2) of the dielectric function corresponding to the previous optical conductivity. (Bottom) Corresponding reflectivity. **a**, (top) σ_1 and σ_2 of a metal with strongly correlated electrons. The scattering rate is frequency dependent ($1/\tau(\omega)$). (Middle) ϵ_1 and ϵ_2 corresponding to the previous optical conductivity. (Bottom) Corresponding reflectivity.

By construction, the memory function $M(\omega)$ has to respect some conditions[140]:

- $M(\omega)$ is a holomorphic function for ω non-real.
- $M(\omega)$ decreases asymptotically like $1/\omega$.
- $M(\omega)$ obeys the symmetry relations $M(\omega) = -M(-\omega)$ and $M^*(\omega) = M(\omega^*)$

Beyond these conditions, the memory function can take any form. For example, the reflectivity of ZrB_{12} was impossible to fit with a simple Drude-Lorentz model [165]. To solve the problem, Teyssier et al. used the extended Drude model with a memory function composed of a superposition

of Dirac peaks. The deviation from the simple Drude model comes, in this case, from the electron-phonon coupling. A second example is high-Tc cuprates

$\text{Bi}_2\text{Sr}_2\text{Ca}_2\text{Cu}_3\text{O}_{10+\delta}$, $\text{Bi}_2\text{Sr}_2\text{CaCu}_2\text{O}_{8+\delta}$ and $\text{Bi}_2\text{Sr}_2\text{Cu}_2\text{O}_{6+\delta}$ for which the reflectivity and ellipsometric measurements are not well approximated by the simple Drude-Lorentz model [166]. In this case, Heumen et al. provide a memory function which allowed to deduce the strong correlations of these materials and infer that a part is of electronic origin. Figure 3.3b shows the optical conductivity, as well as the dielectric function and the reflectivity of a metal with strongly correlated electrons. The scattering rate of σ_1 is frequency dependent ($1/\tau(\omega)$), unlike simple metal.

For materials with strong correlations, the idea is to provide a complete energy-dependent scattering rate $\tau(\omega)$ to compute the optical conductivity. However, the lack of information on its frequency dependence often leads to consider simpler models. In the case of Fermi liquid with electron-electron correlations, it is possible to approximate this frequency dependant scattering rate using two Lorentzian functions centered at $\omega = 0$ with different scattering rate ($\frac{1}{\tau_1}$ and $\frac{1}{\tau_2}$). This results in the addition of a second Drude peak. The first narrow Drude peak represents the coherent part of the electrons motion in the lattice and the second peak simulates the incoherent part with a large scattering rate (around 10 times broader) which extends to the middle infrared domain.

The study of Nakajima et al. [167] shows reflectivity measurements of $\text{Ba}(\text{Fe}_{1-x}\text{Co}_x)_2\text{As}_2$ with different doping levels and reveals, after analytical inversion, that a shoulder appears at the tail of the optical conductivities. This shoulder cannot be fitted with a simple Drude-Lorentz model, but they noted that it's possible to fit this mid-infrared band by adding a second Drude peak. The optical conductivities of 3d transition metal pnictides [168] deduced from reflectivity measurements were analysed with the same method. In our study, it was also impossible to fit the optical measurements with a simple Drude model as shown on the example of LaNiO_3 thin film on LaAlO_3 in figure 3.4a (the fit procedure is explained in the Section 3.2.7). The corresponding optical conductivity of this "one Drude" fit is given in figure 3.4b. Adding a second broad Drude peak allows to improve considerably the matching between the data and the model (Fig. 3.4c). Figure 3.4d shows the behaviour of the optical conductivity of LaNiO_3 thin film corresponding to the double Drude fitting. A shoulder appear at the end of the narrow Drude in comparison with the optical conductivity of the simple Drude fit (shown in dash green).

3. Optical properties of LaNiO_3 films tuned from compressive to tensile strain.

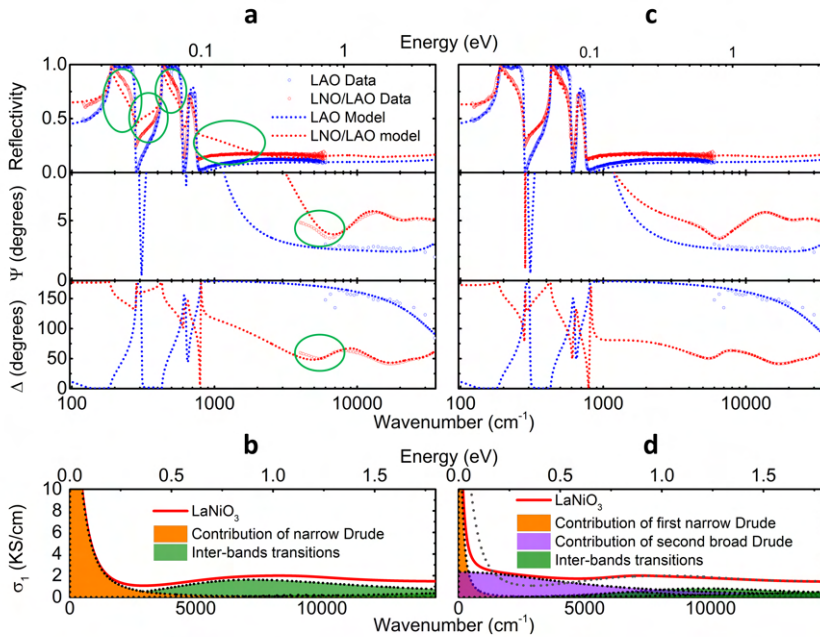


Figure 3.4: **a**, Simple Drude-Lorentz modeling of LaAlO_3 (LAO) and LaNiO_3 thin film on LaAlO_3 (LNO/LAO). **b**, Corresponding LaNiO_3 thin film optical conductivity from the simple Drude-Lorentz modeling. **c**, Double Drude-Lorentz modeling of LaNiO_3 thin film on LaAlO_3 . **d**, Optical conductivity of LaNiO_3 thin film resulting from double Drude-Lorentz modeling. The conductivity of the simple Drude-Lorentz is shown in dash gray for comparison.

3.2.6 Analytical inversion and Kramers-Kronig relations

In our study we investigate the optical conductivity of LaNiO_3 thin films deposited on various substrates inducing epitaxial strain. The optical conductivity cannot be measured directly but it can be determined by combining optical quantities. Using different optical techniques, we measure reflectivity, transmission, ellipsometric angles and resistivity of all the bare substrates and films+substrates to provide optical conductivity spectra in a broad range. Some of these techniques, like THz time domain transmission and ellipsometry, measure respectively the electric field or simultaneously the intensity and the phase of light, and therefore allow to get the complex optical conductivity ($\sigma = \sigma_1 + i\sigma_2$). However, some measurement such as normal incident reflectivity collects light intensity and provide only σ_1 after

analytical inversion. By virtue of the causality principle, the Kramers-Kronig relations allow from the knowledge of the the reflectivity over a broad (ideally infinite) energy range to deduce the phase and more generally relate real and imaginary part of an optical conductivity. The Kramers-Kronig relations for the optical conductivity are:

$$\begin{aligned}\sigma_1(\omega) &= \frac{1}{\pi} \mathcal{P} \int_{-\infty}^{\infty} \frac{\sigma_2(\omega')}{\omega' - \omega} d\omega' \\ \sigma_2(\omega) &= -\frac{1}{\pi} \mathcal{P} \int_{-\infty}^{\infty} \frac{\sigma_1(\omega')}{\omega' - \omega} d\omega'\end{aligned}\tag{3.24}$$

With \mathcal{P} the Cauchy principle value defined as $\mathcal{P}(1/x) = 1/x$ for $x \neq 0$ and $\mathcal{P}(1/x) = 0$ for $x = 0$.

However, this approach is limited and was not very convenient for the analysis of our thin films as it is not straight forward to deduce the sole contribution of the film even if the bare substrates have been measured. Furthermore, in our study the huge phonons signal of the substrates completely screens the response of the film in some regions of the infrared spectra, making the distinction between substrate and film impossible, and therefore producing singularities in the optical conductivity for this frequency range. To circumvent the problem we use a Drude-Lorentz fitting of the data explained in the next section.

3.2.7 Drude-Lorentz fitting of optical measurements with "Reffit"

An alternative approach to the analytical inversion is to fit the data with a Drude-Lorentz model. The objective is to elaborate Drude-Lorentz models with variable parameters for the substrate and the film and then to calculate the optical quantities (reflectivity, transmission or ellipsometry) using the Fresnel equations taking into account the parameters of the samples and of the experiment. The parameters of the models are then fitted to reconcile the calculated optical quantities with the experimental data. Examples of the fit of LaAlO_3 and LaNiO_3 on LaAlO_3 were shown in figure 3.4. Figure 3.5 summarizes the fitting procedure used in this study. The program "Reffit"[169] developed by Alexey Kuzmenko allows to model any optical conductivity with Drude-Lorentz models and to fit optical data. The first step is to create approximative models of both materials (we take the example of the last section: a LaNiO_3 film on a LaAlO_3 substrate) as shown in figure 3.5a. In this case, we expect a Drude peak characteristic for the metallic LaNiO_3 and several phonons in the infrared range characteristic for an insulating perovskite oxide LaAlO_3 . Then, the known parameters of the

3. Optical properties of LaNiO_3 films tuned from compressive to tensile strain.

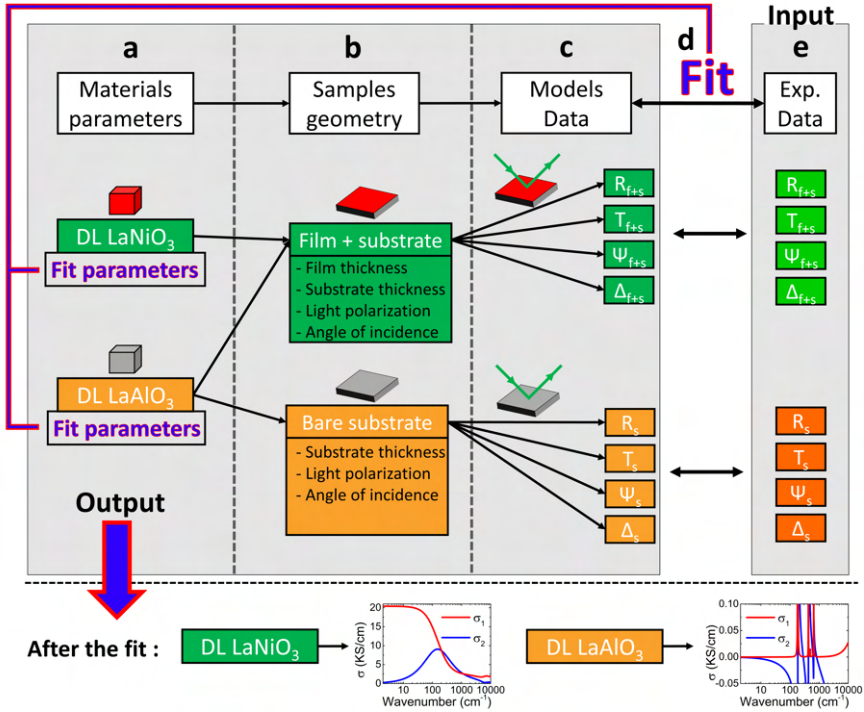


Figure 3.5: Schematic representation of the fitting process. **a**, Drude-Lorentz models of the film material (LaNiO_3) and the substrate material (LaAlO_3). The models contain the parameters which are fitted. After the fit, the parameters allow to provide optical conductivities based on the models. **b**, Specification of samples and experimental parameters. **c**, Optical quantities deduced from Drude-Lorentz models, samples and experimental parameters using Fresnel equations. **d**, Fit of the models parameters from experimental data and optical quantities coming from the models. The fit is an iterative loop. **e**, Experimental data.

samples, such as the thickness of the substrate, the multilayers structure of the ensemble film+substrate, the thickness and the in-plane isotropy of the film are defined as shown in figure 3.5b. The experimental parameters such as light polarization or angle of incidence have also to be specified. From Drude-Lorentz models as well as samples and experimental parameters, the program deduce all optical quantities (Fig. 3.5c) of the bare substrate and film+substrate (reflectivities R_s and R_{f+s} , transmissivities T_s and T_{f+s} , ellipsometric angles Ψ_s , Δ_s and Ψ_{f+s} , Δ_{f+s}) using the Fresnel equations discussed in sections 3.2.8 to 3.2.10. Finally, the program fits (Fig. 3.5d) simultaneously the parameters of the models of the film and of the substrate by comparing the data provide by the models and the experimental data (Fig. 3.5e). This is an iterative loop.

The fit (Fig. 3.5d) is performed by "Reffit" using the Levenberg-Marquardt algorithm of the chi-square minimization. This algorithm is first based on the "gradient descent" method which is determined by the minimization of the gradient:

$$\beta_k = -\frac{1}{2} \frac{\partial \chi^2}{\partial p_k} = \sum_{i=1}^N \frac{y_i - f(x_i, p_1, \dots, p_m)}{\sigma_i^2} \frac{\partial f}{\partial p_k}(x_i, p_1, \dots, p_m) \quad (3.25)$$

with χ^2 the chi-square functional, x_i the data coordinate, y_i the data value and σ_i the data error bar, while the internal parameters of the models are p_i . The program adjusts the parameter $p_k \rightarrow p_k + \delta p_k$ with $\delta p_k = c\beta_k$ ("c" a constant) and check if the fit is improved. Close to the minimum of β_k , and especially for many fitted parameters, the program minimizes the second derivative of χ^2 :

$$\alpha_{kl} = \frac{1}{2} \frac{\partial^2 \chi^2}{\partial p_k \partial p_l} \quad (3.26)$$

More details can be found in the "Reffit manual" [169]. After the minimization of β_k and α_{kl} , the Drude-Lorentz models parameters are adjusted and they can provide outputs of the optical conductivities. The corresponding optical conductivities are shown in bottom of figure 3.5.

3.2.8 General expressions of Fresnel equations

When an electromagnetic wave impinges on the interface between two media of different refractive index N , part of the incident wave is reflected while the rest is transmitted. The Fresnel equations define the ratios of the reflected R or the transmitted T electromagnetic energy flux with the incident electric field. Both reflected and transmitted light conserve the initial wave energy and $R+T=1$, while the absorption takes place inside the medium. These relations depend on the dielectric function of the two media.

In the case of the propagation of a plane electromagnetic wave from vacuum with a complex refractive index N_v ($n_{1v} = \mu_{1v} = 1; \kappa_{1v} = 0$) into a medium with refractive index N_m ($\epsilon_{1m} \neq 1, \mu_{1m} \neq 1$) as shown in figures 3.6a and b, two cases have to be considered: The case where the electric field is perpendicular to the plane of incidence xz , called s-polarization E_s (figure 3.6a) and the case where the electric field is parallel, called p-polarization E_p (figure 3.6b). Incident, reflected and transmitted light can be described by electromagnetic plane waves with electric field amplitude E_0 , magnetic field amplitude H_0 , a wave vector \mathbf{k} , a frequency ω and a velocity v :

3. Optical properties of LaNiO₃ films tuned from compressive to tensile strain.

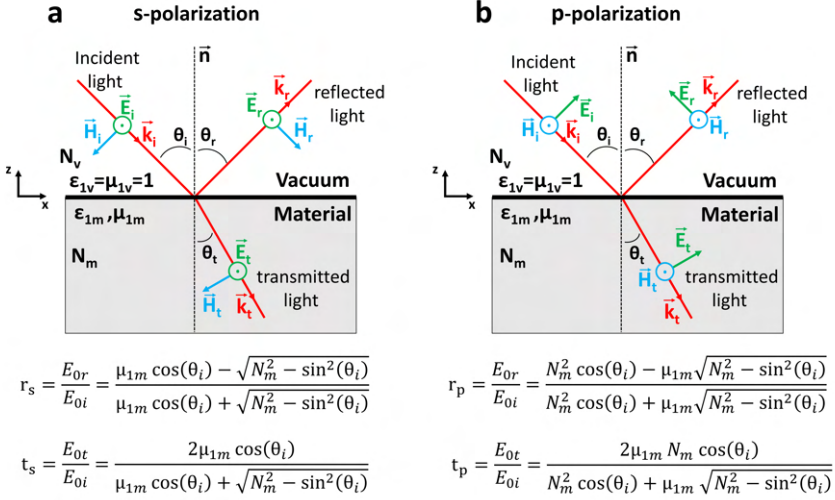


Figure 3.6: Illustration of the interaction of light with matter between two media. **a**, s-polarization. **b**, p-polarization. r_s , t_s and r_p , t_p are the complex reflections and transmission for the s and p-polarization, respectively.

- Incident light: $\mathbf{E}_i = \mathbf{E}_{0i} e^{i(\mathbf{k}_i \mathbf{r} - \omega_i t)}$ and $\mathbf{H}_i = \mathbf{n}_{k_i} \times \mathbf{E}_i$
- reflected light: $\mathbf{E}_r = \mathbf{E}_{0r} e^{i(\mathbf{k}_r \mathbf{r} - \omega_r t)}$ and $\mathbf{H}_r = \mathbf{n}_{k_r} \times \mathbf{E}_r$
- transmitted light: $\mathbf{E}_t = \mathbf{E}_{0t} e^{i(\mathbf{k}_t \mathbf{r} - \omega_t t)}$ and $\mathbf{H}_t = \sqrt{\frac{\epsilon_1}{\mu_1}} \mathbf{n}_{k_t} \times \mathbf{E}_t$

with \mathbf{n}_k the unit vector along \mathbf{k} and \mathbf{H} the magnetic field. Considering that the xy plane is the interface between the two media as shown in figure 3.6, the three vectors \mathbf{k}_i , \mathbf{k}_r and \mathbf{k}_t are in the same xz plane. There is no energy loss during reflection or transmission which implies that the frequency are equal $\omega_i = \omega_r = \omega_t$. Moreover, the speed of the reflected light is the same as the initial one $v_i = v_r = v_t$ (same medium). Therefore, incident and reflected light angles are the same $\theta_i = \theta_r$. Using Maxwell equations in matter in their integral form and considering an isotropic non-magnetic material ($\mu_{1m} = 1$), the complex reflection r_s and r_p , respectively perpendicular and parallel to the incident plane, as well as the complex transmission t_s and t_p , can be derived and are shown on bottom of figure 3.6a and b. Note that in the case of normal incident reflection, as for infrared microscope measurement, the distinction between $R_s = |r_s|^2$ and $R_p = |r_p|^2$ is irrelevant and the total reflection R (considering a non-magnetic sample) simplifies to: $R = \left| \frac{\sqrt{\epsilon-1}}{\sqrt{\epsilon+1}} \right|^2$. The complete derivation of Fresnel equations can be find in the reference [170, 171].

3.2.9 Fresnel equations of thin film on a substrate

In this section, we are interested in the Fresnel equations of a thin film deposited on a semi-infinite substrate. When the light impinges on the film, the electromagnetic wave is split between reflected and transmitted light as explain previously. However, there are now multiple reflections between the film/substrate and film/vacuum interfaces as shown in figure 3.7. These reflections have to be taken into account to deduce the total reflectivity r_{vfs} (vacuum, film, substrate) and the transmittivity t_{vfs} . To deduce these coefficients, consider the general Fresnel equations resulting from the boundary conditions:

$$\begin{aligned}
 r_s &= \frac{N_i \cos(\theta_i) - N_t \cos(\theta_t)}{N_i \cos(\theta_i) + N_t \cos(\theta_t)} & r_p &= \frac{N_t \cos(\theta_i) - N_i \cos(\theta_t)}{N_t \cos(\theta_i) + N_i \cos(\theta_t)} \\
 t_s &= \frac{2N_i \cos(\theta_i)}{N_i \cos(\theta_i) + N_t \cos(\theta_t)} & t_p &= \frac{2N_i \cos(\theta_i)}{N_t \cos(\theta_i) + N_i \cos(\theta_t)}
 \end{aligned}
 \tag{3.27}$$

With the indices i and t corresponding respectively to the incident and transmitted light (medium). For multiple reflections, and because the different optical path lengths, the phase of the light is different between the first r_{vf} and the second r_{fs} beam reflections. It may induce interferences which depend on the light wavelength, on the refractive indexes and on the thickness d of the film.

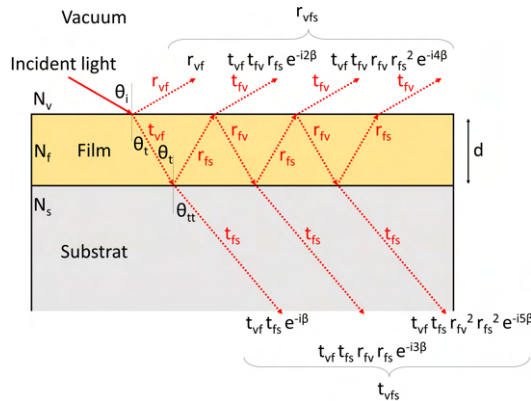


Figure 3.7: Representation of the multiple reflections at the film/substrate and film/vacuum interfaces.

3. Optical properties of LaNiO_3 films tuned from compressive to tensile strain.

After one transmission of the beam from vacuum to film t_{vf} followed by the reflection at the interface film/substrate r_{fs} , the outgoing light (t_{fv}) acquires a phase difference of 2β with β the film phase thickness defined as : $\beta = \frac{2\pi d N_f}{\lambda} \cos(\theta_t)$. The phase of the light can therefore be written as $e^{i2\beta}$. To deduce the total reflectivity r_{vfs} , it is sufficient to sum up the contribution of all the outgoing beams which form an infinite series simplified by an irreducible fraction. The same applies for the transmission. The amplitude reflection and transmission coefficients for the s and p-polarization are:

$$\begin{aligned}
 r_{vfs,s} &= \frac{r_{vf,s} + r_{fs,s}e^{-i2\beta}}{1 + r_{vf,s}r_{fs,s}e^{-i2\beta}} & r_{vfs,p} &= \frac{r_{vf,p} + r_{fs,p}e^{-i2\beta}}{1 + r_{vf,p}r_{fs,p}e^{-i2\beta}} \\
 t_{vfs,s} &= \frac{t_{vf,s}t_{fs,s}e^{-i\beta}}{1 + r_{vf,s}r_{fs,s}e^{-i2\beta}} & t_{vfs,p} &= \frac{t_{vf,p}t_{fs,p}e^{-i\beta}}{1 + r_{vf,p}r_{fs,p}e^{-i2\beta}}
 \end{aligned} \tag{3.28}$$

with v, f and s the vacuum, film and substrate medium respectively. Full developments can be found in references [172] and [173]. However, there is no analytical solution to express N_f (therefore ϵ_f and σ_f) as a function of r_{vfs} or t_{vfs} . The determination of the complex refractive index can be obtained by numerical iterations and is the purpose of the program "Reffit" described in the section 3.2.7.

3.2.10 Fresnel equations relating thin film ellipsometry to dielectric function ϵ

In this section, we will show that from ellipsometric measurements (described in the section 3.3.5) of a thin film on a substrate, it is possible to deduce the dielectric function $\epsilon(\omega)$ of the film. We consider light coming from the vacuum into a semi-infinite non-magnetic isotropic material ($\mu_1 = 1$) and simply rename the refractive index of the medium N_m by N and the initial angle θ_i by θ . From the complex reflectance defined as $\rho = \frac{r_p}{r_s}$ and using the Fresnel coefficients for s and p-polarized reflectivity shown in figure 3.6, the dielectric function ϵ and the complex reflectance ρ are related by the following formula :

$$\begin{aligned}
 \rho &= \frac{\sin(\theta)\tan(\theta) - \sqrt{\epsilon - \sin^2(\theta)}}{\sin(\theta)\tan(\theta) + \sqrt{\epsilon - \sin^2(\theta)}} \\
 \rightarrow \epsilon &= \sin^2(\theta) \left(1 + \tan^2(\theta) \left(\frac{1 - \rho}{1 + \rho} \right)^2 \right)
 \end{aligned} \tag{3.29}$$

In the case of a thin film deposited on a substrate, we saw that the Fresnel coefficients for multiple reflections are given by equations 3.28. The bare substrate reflectance can be denoted by ρ_{sub} and depends on the substrate dielectric function ϵ_{sub} , while the reflectance of the film+substrate is expressed by ρ . Using equations 3.28, ρ_{sub} and ρ give at the end of the day a relation of the dielectric function $\epsilon(\omega)$ of the film as a function of the dielectric function of the substrate ϵ_{sub} , the measured reflectance ρ of film+substrate and the measured reflectance ρ_{sub} from the bare substrate measurement:

$$\epsilon = \frac{1 + \epsilon_{sub} + C}{2} \pm \sqrt{\left(\frac{1 + \epsilon_{sub} + C}{2}\right)^2 - \epsilon_{sub}} \quad (3.30)$$

With C a factor depending on the initial angle θ , the light frequency ω , the thickness d of the film and is defined as:

$$C = i(\epsilon_{sub} - 1) \frac{\frac{\rho}{\rho_{sub}} - 1}{2\omega d \cos(\theta)} \left(1 - \frac{\epsilon_{sub} \sin^2(\theta)}{\epsilon_{sub} - \sin^2(\theta)}\right) \quad (3.31)$$

More details can be found in the appendix A of Ref. [62].

3.3 Experimental methods

In this section, we will discuss in detail the different optical measurement techniques used in this study which were combined to obtain the conductivity of the films according to the methods described previously. For each techniques, the optical quantities are discussed in the frame of the used methodology and the measured spectra are shown for all samples at low temperature.

3.3.1 Samples preparation

LaNiO₃ thin films were deposited on various substrates, which induce compressive or tensile strain through the film/substrate lattice mismatch. We used commercial single-crystal YAlO₃ (YAO), NdAlO₃ (NAO), LaAlO₃ (LAO), NdGaO₃ (NGO) and SrTiO₃ (STO) substrates from CrysTec GmbH with a 5 × 5 mm² surface area and 0.5 mm in thickness. All surfaces were (001)-oriented in pseudo-cubic notation. Prior to deposition all substrates were thermally treated in flowing oxygen to ensure atomically-flat surfaces. The epitaxial LaNiO₃ films were deposited via radio frequency off-axis magnetron sputtering at a temperature of 510°C in an oxygen:argon mix of 2:7 maintained at 0.24 mbar. After deposition, the quality of the films surface

3. Optical properties of LaNiO_3 films tuned from compressive to tensile strain.

was measured by atomic force microscopy and the crystallographic properties were checked using X-ray diffraction. Bragg-Brentano scans showed finite thickness oscillations, indicating a high quality film, providing the precise film thickness and the lattice constants of each film/substrate (see Table 3.1).

For each film/substrate combination, four contacts were made at the sample corners and transport measurements were done using the Van-Der-Pauw method. Then the DC resistivity was recorded in a ^4He dipping station down to 4 K.

Film specifications are summarized in Table 3.1.

Substrate	YAlO_3	NdAlO_3	LaAlO_3	NdGaO_3	SrTiO_3
Space group	Pnma	$\text{R}\bar{3}\text{c}$	$\text{R}\bar{3}\text{c}$	Pnma	$\text{Pm}\bar{3}\text{m}$
Substrate $a_{\text{sub},\text{exp}}^{(i)}$ (Å)	3.71	3.74	3.789	3.864	3.905
Film c -axis constant $^{(ii)}$ (Å)	3.87	3.953	3.91	3.822	3.818
Film cell volume (Å^3)	53.3	55.3	56.1	57.1	58.2
Film strain	-3.34%	-2.55%	-1.28%	+0.68%	+1.75%
Film thickness (uc) $^{(iii)}$	16	13	14	14	13
Film thickness (nm) $^{(iii)}$	6.2	5.1	5.5	5.4	5.0

Table 3.1: Film parameters determined at room temperature. Pnma, $\text{R}\bar{3}\text{c}$ and $\text{Pm}\bar{3}\text{m}$ belong to the orthorhombic, rhombohedral and cubic crystal systems respectively. (i) These values represent the geometric mean of the pseudocubic lattice constants parallel to the (001)-oriented substrate surfaces, and were obtained from out-of-plane X-ray diffraction data of the substrate measured at room temperature. (ii) Pseudocubic c -axis parameter calculated from the $\theta - 2\theta$ X-ray diffraction of the films. (iii) Thickness in units of the pseudocubic c -axis parameter, determined from the $\theta - 2\theta$ X-ray diffraction pattern of the films.

3.3.2 DC conductivity

DC (Direct Current) conductivity is the current response of a material subjected to an external static (no alternative) electric field $E(\omega = 0)$. It is the limit of the optical conductivity $\sigma(\omega \rightarrow 0)$. Applying a DC current through the material and measuring the resulting voltage gives the DC resistivity which is the inverse of DC conductivity. The van der Pauw method is a four-terminal sensing measurement, in which electrical connections are made at each corner of the sample. This method is widely used to measure the DC conductivity of thin films and in our case it allows to preserve most of the sample surface available for optical measurements.

Figure 3.8a shows the evolution of the resistivity $\rho(T) - \rho_0$ of strained films as a function of temperature from 10 to 300 K, with ρ_0 corresponds to the residual resistivity at 10 K. The increase of resistivity for increasing temperature is associated with the metallic behavior of LaNiO_3 . The values of $\rho(300\text{K})/\rho_0$, so-called residual resistivity ratio RRR (a large value indicates

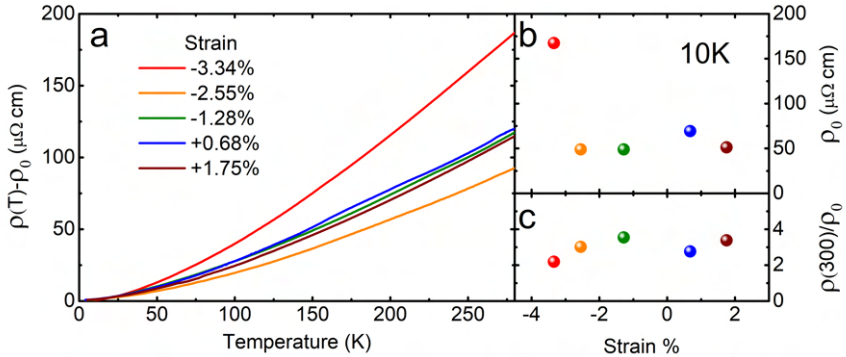


Figure 3.8: Direct current resistivity. **a**, Temperature dependent part of the DC resistivity, $\rho(T) - \rho_0$ of the five LaNiO₃ film/substrate combinations YAlO₃ (-3.34%), NdAlO₃ (-2.55%), LaAlO₃ (-1.28%), NdGaO₃ (+0.68%), SrTiO₃ (+1.75%), where ρ_0 is the residual resistivity. **b**, Values of ρ_0 : 167, 48, 48, 68, and 50 $\mu\Omega\text{cm}$ for YAlO₃, NdAlO₃, LaAlO₃, NdGaO₃, and SrTiO₃ respectively.

a good film quality), shown in Fig. 3.8c, are comparable than the values reported in the thesis of Scherwitzl [58]. At 300 K, $\rho(T) - \rho_0$ is about 100 $\mu\Omega\text{cm}$ and varies linearly for decreasing temperature, while the curves follow a T^2 behaviour below 50 K which supports the well-established Fermi-like T^2 temperature dependence of the resistivity of bulk and thick film LaNiO₃ [174, 175]. The residual resistivity ρ_0 as a function of strain is shown in figure 3.8b. The films at -2.55%, -1.28% and 1.75% of strain show similar resistivity with value around 50 ($\mu\Omega\text{cm}$), while the most compressively strained thin film (-3.34%) shows a huge increase of the residual resistivity (167 $\mu\Omega\text{cm}$) as observed by Scherwitzl [58]. A small increase is observed for the +0.68% strained film unlike Scherwitzl's results who observed a resistivity of 100 ($\mu\Omega\text{cm}$) for both tensile strains. Note that tensile strain may increase oxygen vacancy formation and increase the resistivity of the films [72, 176]. The low resistivity values of our tensile strained samples evince their good quality.

3.3.3 UHV cryostat

In all the experiments, we use ultra-high vacuum (10^{-7} - 10^{-6}) helium flow cryostats allowing measurements down to 10 K. A thermistor and a diode are mounted on the sample holder to assure a smooth and continuous temperature control.

3. Optical properties of LaNiO_3 films tuned from compressive to tensile strain.

3.3.4 Time domain Terahertz transmission

We measured Terahertz time domain transmission in the range of 0.2 to 3 THz (i.e. 7 and 100 cm^{-1} or 0.8 and 12 meV). The system is inside a chamber purged with nitrogen to avoid the huge absorption of water vapor and CO_2 in this frequency range.

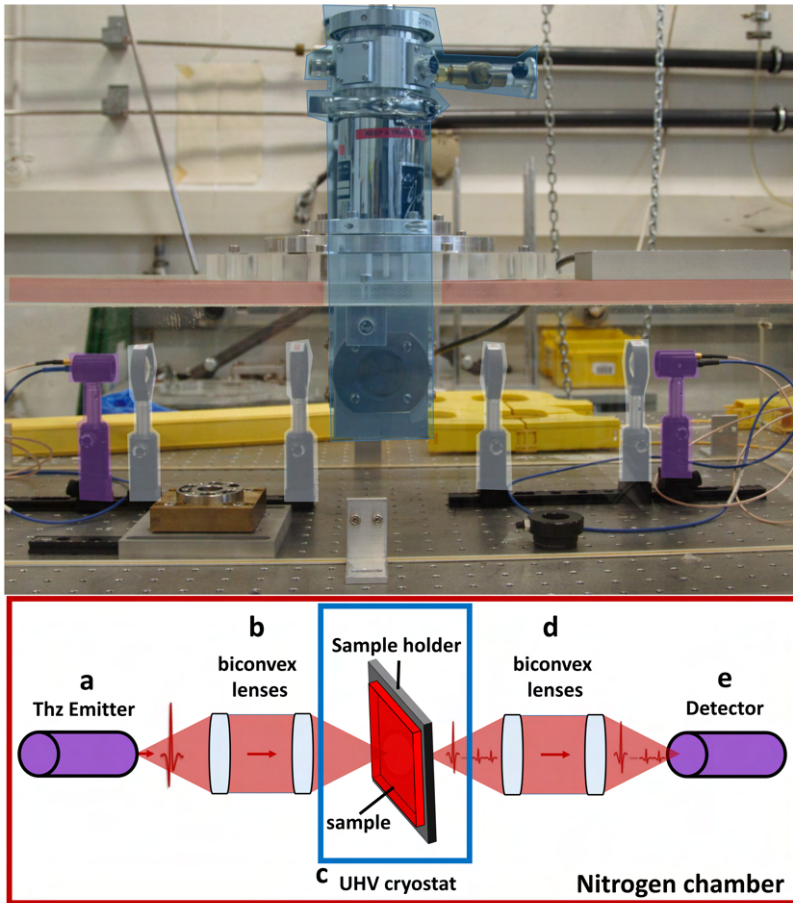


Figure 3.9: Terahertz time domain transmission setup. **a**, Thz emitter. **b**, Biconvex optical Lenses. **c**, Pierced sample holder covered by the sample in the ultrahigh vacuum cryostat. **d**, Biconvex optical Lenses. **e**, Detector.

Our home-made Terahertz transmission setup is composed of:

1. An emitter (fig. 3.9a), a photoconductive antenna polarized with DC

bias, generates a fast electromagnetic pulse in terahertz range (see more details in reference [177]).

2. Two biconvex lenses focus the pulse on the sample (fig. 3.9b).
3. The sample holder is a vertical copper plate which is pierced with a hole smaller than the samples. Both are placed inside a Janis UHV cryostat to measure down to 10 K (fig. 3.9c).
4. Two lenses collect the transmitted pulse and focuses it on the detector (fig. 3.9d).
5. The detector (Fig. 3.9f) is also a photoconductive antenna whose DC bias is replaced by an amperemeter. The transmitted terahertz pulse acts now as the external electric field and induces a transient current in the antenna. By measuring the value of this current as a function of time, we obtain the shape of the transmitted electric field E . Measuring directly E (and not only the intensity $I \propto E^2$) implies that the phase is accessible. In principle, it's possible to derive from this quantity (E) the complex dielectric function ϵ of the material. In the frame of our fitting procedure presented in section 3.2.7, we decided to use only the intensity and to calculate the transmission T . A fast Fourier transformation (FFT) of the electric field E and the product with its complex conjugate allows to obtain an intensity spectrum $I = E \cdot E^*$.
6. The ratio between the transmitted intensity with and without sample gives the transmission T of the material:

$$T = \frac{I_{sample}}{I_{ref}} = \frac{E_{sample} \cdot E_{sample}^*}{E_{ref} \cdot E_{ref}^*} \quad (3.32)$$

Multiple pulses due to film/substrate and film/nitrogen interfaces are separated in space and time (Fig. 3.9c). To extract the contribution of a simple transmission, the analysis has to take into account only the first pulse. THz transmission measurement works only for transparent media and SrTiO₃ as well as LaNiO₃ on SrTiO₃ could not be measured.

Figure 3.10 shows the THz transmission of all the bare substrates and films + substrates. The transmission are around 0.4 and 0.2 for the bare substrate and films+substrates respectively. The transmission is lower for films+substrates due to the metallic behaviour of the films. We observe for increasing energy a decrease of the transmission due to a phonon placed between 50 and 100 cm⁻¹ depending the substrate. The presence of twin domains in the LaAlO₃ and NdAlO₃ substrates influences the terahertz transmission. In the case of LaAlO₃ and LaNiO₃ films on LaAlO₃ substrates, we managed to cancel this interference effect by a proper incoming polarisation orientation. This

3. Optical properties of LaNiO_3 films tuned from compressive to tensile strain.

was not possible for NdAlO_3 and LaNiO_3 films on NdAlO_3 and we observe a drop at 25 cm^{-1} for both samples.

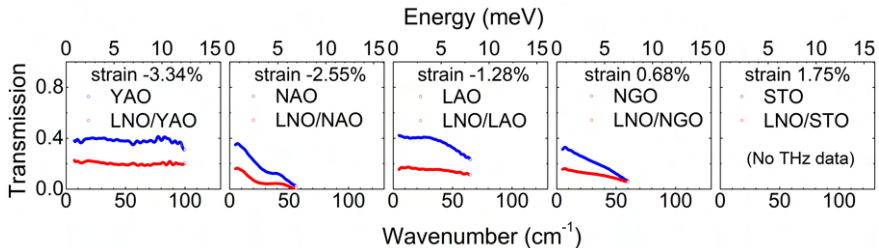


Figure 3.10: THz transmission data of the bare substrates (blue) and the films+substrates (red) at 10 K for the four strains (no THz measurement was possible for SrTiO_3 and LaNiO_3 on SrTiO_3).

3.3.5 Ellipsometry

Principle of ellipsometry measurement

Ellipsometry is an optical technique based on the change of polarization of light after reflection on a sample. An incident light is focused on a fixed polarizer to obtain a linear polarized beam. The light is then sent on the sample with an angle of incidence θ_i with respect to the normal. After reflection, the light is elliptically polarized and passes through an analyzer before being collected. Figure 3.11a illustrates the general setup to perform measurement.

The reflected beam can be decomposed into r_p and r_s components (defined in the section 3.2.8) and the complex reflectance ρ is defined as the ratio between both.

$$\rho = \frac{r_p}{r_s} = \tan(\Psi)e^{i\Delta} \quad (3.33)$$

with the two ellipsometric angles: Ψ related to the ratio of the norm of r_p and r_s ($\tan(\Psi) = \frac{|r_p|}{|r_s|}$ Fig. 3.11d) and Δ the phase difference between reflected S and P-polarized light ($\Delta = \phi_{rp} - \phi_{rs}$ Fig. 3.11c). The analysis of the signal depends on the measured technique and are described in the following. Note that the angle θ_i is chosen near the Brewster angle where the ratio between r_p and r_s is the highest (Fig. 3.11b). At the Brewster angle, P-polarization is completely refracted $\Rightarrow r_p = 0$ for medium without absorption. Using a HUV cryostat, the light travels through two windows and affects its polarization. It is possible to adjust this deviation by measuring the sample at room temperature inside and outside the cryostat. We consider

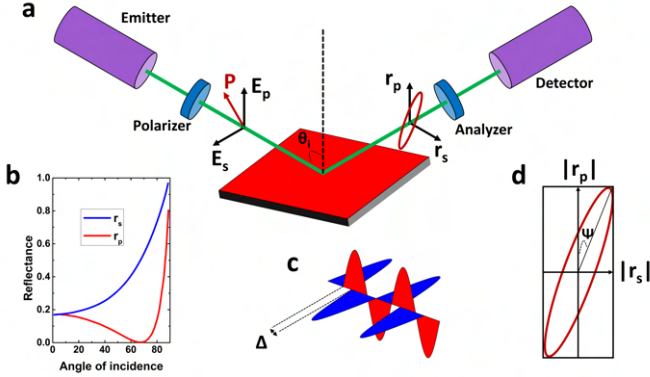


Figure 3.11: **a**, Ellipsometric measurement setup. **b**, Examples of reflectance for r_s and r_p polarization. **c**, Illustration of the phase shift between r_s and r_p . This phase shift is quantified by the angle $\Delta = \phi_{r_p} - \phi_{r_s}$. **d**, Illustration of the elliptical polarization of the light after reflection. The angle Ψ is related to r_s and r_p by :

$$\tan(\Psi) = \frac{|r_p|}{|r_s|}.$$

that the windows are not affected by the change of temperature and therefore the windows correction for Ψ and Δ are:

$$\tan(\Psi(T)) = \frac{\tan(\Psi_{cryo}(T))}{\tan(\Psi_{out}(T))} \quad (3.34)$$

$$\Delta(T) = \Delta_{cryo}(T) - \Delta_{out}(T) \quad (3.35)$$

Sections 3.3.6 and 3.3.7 present two different ellipsometry techniques, time domain terahertz ellipsometry and rotating analyzer visible ellipsometry, used in our study.

3.3.6 Time domain terahertz ellipsometry

We measure from 15 cm^{-1} ($\sim 2 \text{ meV}$) to 120 cm^{-1} ($\sim 15 \text{ meV}$) using a homemade ellipsometer which is surrounded by a high vacuum chamber (Fig. 3.12) maintained at 10^{-8} mbar. An airlock allows to insert the sample without breaking the vacuum of the main chamber

This setup uses a fast electromagnetic pulse in the THz frequency range, which is produced with the same system as the terahertz time domain transmission setup discussed in the section 3.3.4. The polarizer is set to 45° and only two measurements are performed: Analyzer set to 0° provides the complex E_p electric field, while the analyzer sets at 90° provides the complex E_s electric field. Considering that a gold reference would have the same response in both p and s configurations ($E_{ref,p} = E_{ref,s}$), the complex

3. Optical properties of LaNiO_3 films tuned from compressive to tensile strain.

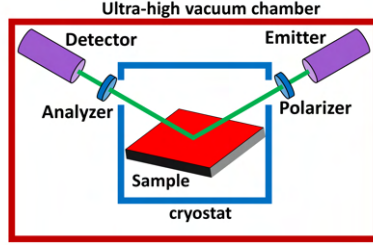


Figure 3.12: Time domain terahertz ellipsometry setup.

reflectance ρ , and therefore the two ellipsometric angles Ψ and Δ , can be directly calculated from E_p and E_s after their fast Fourier transformations:

$$\rho = \frac{r_p}{r_s} = \frac{E_p/E_{ref,p}}{E_s/E_{ref,s}} \quad (3.36)$$

Data were collected with an angle of incidence of 65° (60° for $\text{LaNiO}_3/\text{YAlO}_3$). In this frequency range only Ψ could be obtained with sufficient precision but is still very noisy for some samples.

Figure 3.13 shows the Ψ angle of THz ellipsometry measurements for all the substrates and films+substrates. Due to the high (of order 10^4) dielectric constant of SrTiO_3 no reliable THz ellipsometry data could be obtained for bare and film-covered SrTiO_3 . The value of Ψ is around 25° for the substrates and around 32° for the films+substrate. The value is higher for film+substrate due to the more reflective behaviour of the metallicity of films.

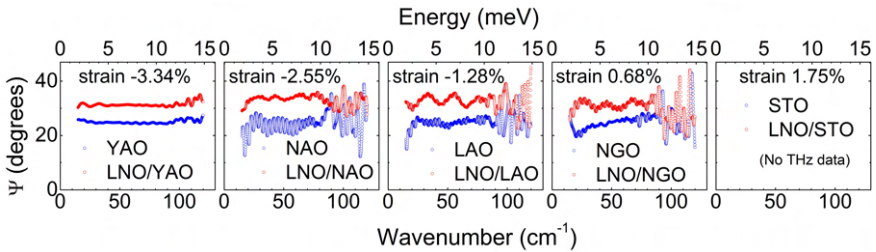


Figure 3.13: Ψ angle of THz ellipsometry measurements of the bare substrates and the films+substrate.

3.3.7 Near-infrared/Visible/Ultraviolet light ellipsometry

We use a Vase ellipsometer from Woollam allowing to measure from 4000 cm^{-1} ($\sim 0.5\text{ eV}$) to 35000 cm^{-1} ($\sim 4.3\text{ eV}$). The physical principle remains the analysis of the elliptically polarized light after reflection on a sample. The system is not in a vacuum chamber or purged with nitrogen because absorption of water vapour and CO_2 are not present in this frequency range. The sample is inside a UHV cryostat and a correction for the polarization effect by the windows of the cryostat has to be taken into account in the analysis of the data. Data were collected with an angle of incidence of 68° . Illustration of the setup is shown in Figure 3.14a.

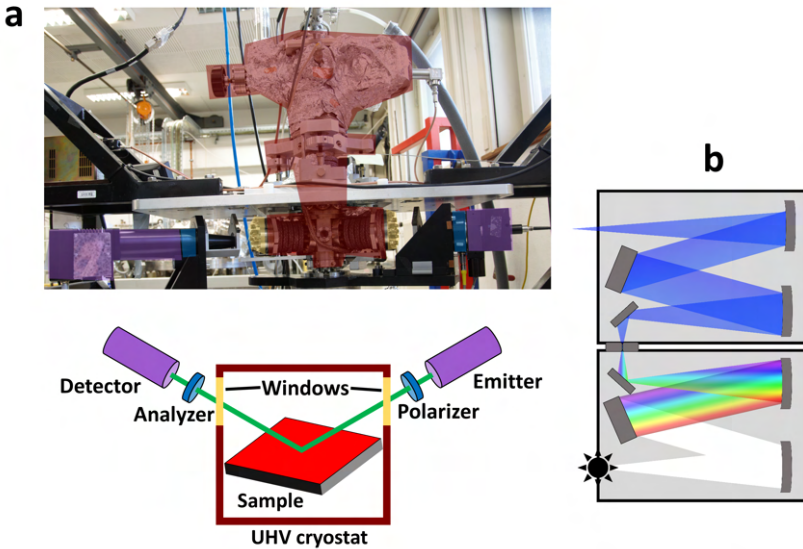


Figure 3.14: a, Visible ellipsometry setup. b, Double subtractive monochromator. The left part allows to select one short frequency range, while the right part refocuses and recombine the beam for the measurement.

The source is a double subtractive monochromator (Fig. 3.14b, white light is first diffracted, one frequency is then selected, and finally the beam is recombined) coupled to the polarizer via an optical fiber. The analyser is rotating at a fixed frequency $\omega = 20\text{ Hz}$ and detection is made using two detectors, strained InGaAs for the near-infrared frequencies and silicon Si for the visible and ultraviolet ranges.

3. Optical properties of LaNiO_3 films tuned from compressive to tensile strain.

The collected light intensity is modulated as:

$$I = I_0(1 + \alpha \cos(2A) + \beta \sin(2A)) \quad (3.37)$$

With A the angle of the analyzer which evolve in time as $A = \omega t$. A Fast Fourier transform of the intensity gives the coefficient α and β . These coefficient are directly measured at the output of the detectors and are related to ellipsometric angles Ψ and Δ by:

$$\alpha = \frac{\tan^2(\Psi) - \tan^2(P)}{\tan^2(\Psi) + \tan^2(P)} \quad \beta = \frac{2 \tan(\Psi) \cos(|\Delta|) \tan(P)}{\tan^2(\Psi) + \tan^2(P)} \quad (3.38)$$

with P the fixed angle of the polarizer. Using the latter formulas, the angles Ψ and Δ are defined as:

$$\tan(\Psi) = \sqrt{\frac{1 + \alpha}{1 - \alpha}} |\tan(P)| \quad \cos(\Delta) = \frac{\beta}{\sqrt{1 - \alpha^2}} \quad (3.39)$$

The complete development can be found in the reference [173].

Ψ and Δ were measured for angles of incidence with the surface normal varying from 65° to 70° for the different samples. Figure 3.15 shows Ψ and Δ for all the substrates and films+substrates. The two ellipsometric angles of the substrates show no features in this frequency range because there is no excitation (middle of the gap), except for SrTiO_3 which reveal features around 30000 cm^{-1} corresponding to interband transitions. The films+substrates show also many features in this frequency range indicating the presence of excitations which will be discussed in the following.

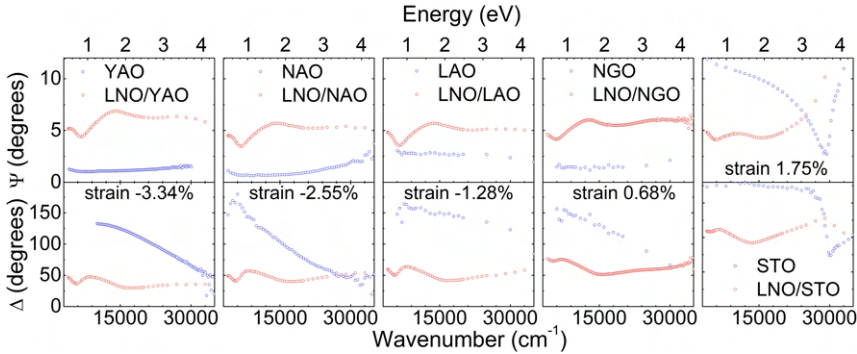


Figure 3.15: Ψ and Δ angle of visible ellipsometry measurements of the bare substrates and the films+substrates.

3.3.8 Infrared microscope

We used a "Hyperion 200" infrared microscope coupled to a Fourier transform infrared (FTIR) spectrometer Vertex 70V manufactured by Bruker which allows to probe the optical conductivity from 120 to 6000 cm^{-1} . The spectrometer is a Michelson-type, so-called Fourier-transform spectrometer, which allows to decompose the broadband frequencies of the infrared sources into its spectral constituents. However, the mirror rotates around an axis (RockSolid configuration) unlike usual Michelson-type spectrometers composed of a linear moving mirror and a static mirror (more details in Ref. [178]). Two sources are used: a mercury arc lamp emitting from 120 to 700 cm^{-1} (FIR) and a globar light emitting from 550 to 6000 cm^{-1} (MIR). A germanium mylar beam splitter and a bolometer detector are used with the FIR source, while a KBr beam splitter and a mercury cadmium telluride (MCT) detector are used with the MIR source. The measurement is done at normal incidence and the beam is focused by a reflective objective (Fig. 3.16c).

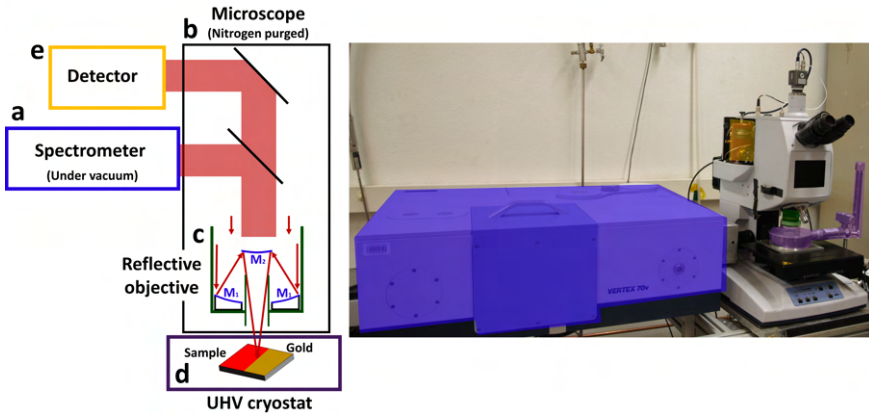


Figure 3.16: Infrared microscope. **a**, Michelson type spectrometer. **b**, Microscope. **c**, Reflective objective composed of two mirrors M_1 and M_2 . **d**, Sample with half of the surface recovered by gold, inside the UHV cryostat. **e**, Detector.

The reflective objective uses two mirrors M_1 and M_2 which focus the beam to the sample. While the spectrometer is under vacuum, the microscope is purge with nitrogen to avoid water vapour and CO_2 absorption. The use of the microscope is not necessary to measure the infrared response of these macroscopic samples, but it allows to measure simultaneously a gold reference deposited on a small part of the sample (Fig. 3.16d), which makes the measurement fast and reliable. The UHV cryostat containing the sample is placed under the objective.

3. Optical properties of LaNiO_3 films tuned from compressive to tensile strain.

Figure 3.17 shows the reflectivity measurements of the bare substrates (blue symbols) and films+substrates (red symbols) from 0 to 1000 cm^{-1} (left panel) and from 1000 to 4000 cm^{-1} (right panel). Many phonons of the substrates are observable between 120 and 900 cm^{-1} which are partially screened by the collective free carriers excitation of LaNiO_3 in the case of films+substrates. These phonons also totally screen the response of the film in some regions. The spectra is almost flat above 1000 cm^{-1} but the value gives many informations about the free carriers spectral weight (modeled by the narrow Drude peak) and the electronic correlations (modeled by the broad Drude peak).

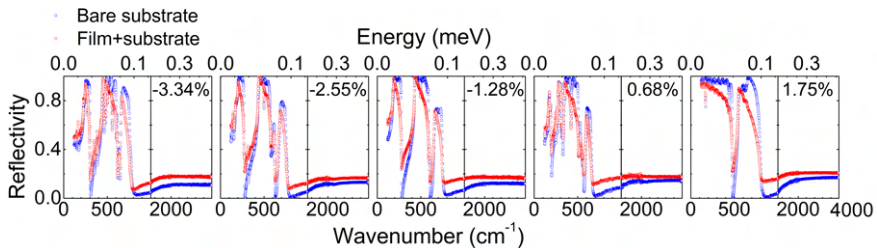


Figure 3.17: Reflectivity measurements of the bare substrates and the films+substrates for -3.34% (LNO/YAO), -2.55% (LNO/NAO), -1.28% (LNO/LAO), 0.68% (LNO/NGO) and 1.75% (LNO/STO) of strain from left to right. Left panels show data from 0 to 1000 cm^{-1} and right panels from 1000 to 4000 cm^{-1} .

3.4 Strain dependence of the optical conductivity

The parameters of Drude-Lorentz models were adjusted with the help of the program RefFit [169], as described in the section 3.2.7, to fit the full set of data of the transmission, reflection and ellipsometry of bare substrates and films+substrate shown in Fig. 3.18.

For all temperatures and strains, the DC conductivity, $\sigma_1(0)$, fell within the noise level of the optical conductivity at the lowest frequencies of the measured range (i.e. 0.6 meV) and we therefore used these transport data as additional constraints. The error bars are obtained by varying the relative weights of the different types of spectra (transmission, reflection, ellipsometry) in the fit procedure. We did not observe significant in-plane anisotropy of the optical constants, which confirms the observations in Ref. [56]. These fits were used to generate the complex optical conductivity which are given at 10 K in Fig. 3.19a.

3.4 Strain dependence of the optical conductivity

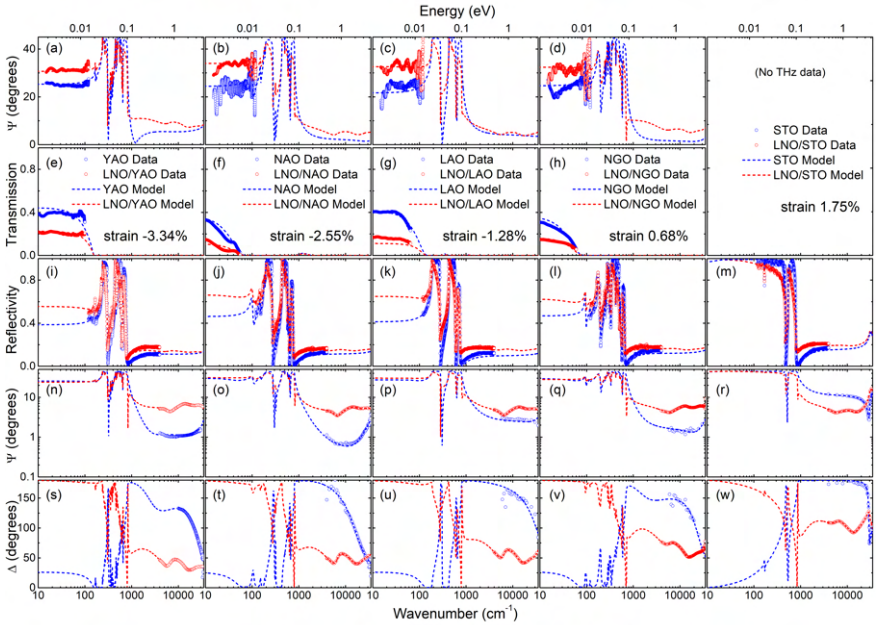


Figure 3.18: Full set of optical data at 10 K of the bare substrates YAlO_3 (YNO), NdAlO_3 (NAO), LaAlO_3 (LAO), NdGaO_3 (NGO), SrTiO_3 (STO) and the LaNiO_3 film+substrates, as well as Drude Lorentz fits to the full data set. Blue dots and curves represent the bare substrate, red dots and curves represent the film+substrate. **a-d**, $\Psi(\omega)$ of the terahertz ellipsometry measurements. **e-h**, Transmission in terahertz range. **i-m**, Infrared reflectivity measurements. **n-r**, $\Psi(\omega)$ angle of the visible ellipsometry measurements. **s-w**, $\Delta(\omega)$ angle of the visible ellipsometry measurements.

The spectrum at low frequencies is dominated by the zero energy mode due to the free carrier response. In order to fit the spectra in the infrared range at low temperature it was necessary to model the optical conductivity at low frequencies as a superposition of a narrow Drude peak ($\hbar/\tau < 0.1$ eV) and a broad Drude peak ($\hbar/\tau = 0.3$ eV) [167, 168] as explained in section 3.2.5. Given that the two-Drude fit only captures the gross features in the infrared part of the spectrum, and finer details are buried by the strong phonon peaks of substrate and film, it is not possible to provide fine details on the frequency dependant scattering rate $1/\tau(\omega)$.

We note however that the superposition of a broad and a narrow Drude peak is expected for a Fermi-liquid [179] for which the quasi-particle scattering rate has the following frequency dependence [140, 179]: $1/\tau = \alpha + \beta\omega^2$. Indeed, the narrow peak corresponds to the frequency range dominated by the constant part of the scattering rate, while the broader one is due to the frequency-dependent term. This observation supports the well-established

3. Optical properties of LaNiO₃ films tuned from compressive to tensile strain.

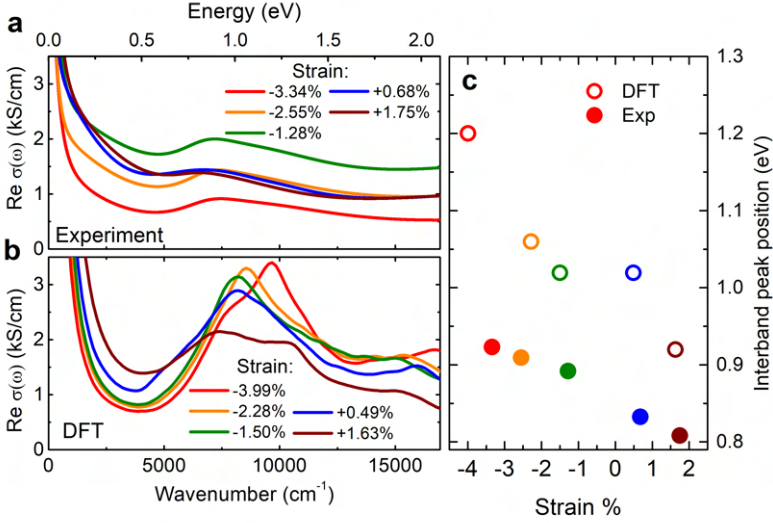


Figure 3.19: **a**, Optical conductivity spectra at 10 K of LaNiO₃ films at different substrate induced in-plane strains indicated in the legend. These spectra roughly fall in two groups: Negative strain (red, orange and green) display a clear peak at 0.8 eV separated from the Drude peak by a minimum at 0.5 eV. Positive strain (blue and brown curves) showing a weak maximum, almost a shoulder, at approx. 0.65 eV. **b**, Optical conductivity spectra calculated with density functional theory (DFT) of LaNiO₃ films for in-plane strains indicated in the legend and assuming a fixed scattering rate $\hbar/\tau=60$ meV. **c**, Position of the maximum of the peak of the optical conductivity at ~ 1 eV, in experiments and in DFT calculations. An overall decrease of the peak position is observed as strain is varied from the most compressive to the most tensile.

Fermi-like T^2 temperature dependence of the resistivity of bulk and thick film LaNiO₃ below 50 K [174, 175] also observed in our resistivity measurements (Fig. 3.8). In thin films the exponent is usually lower [58, 142]. Recently LaNiO₃ films on LSAT substrates were found to show T -linear resistivity below 1 K as a result of magnetic impurity-induced short-range antiferromagnetic fluctuations [180].

We observe a broad peak around 1 eV, which has been reported previously for LaNiO₃ [54, 56] and for the metallic high temperature phase of RNiO₃ with R = Sm, Nd [62]. The experimental optical conductivity at negative strain shows a clear peak at ~ 0.8 eV separated from the Drude peak by a minimum at ~ 0.5 eV (Fig. 3.19a), while for positive strain there is a weak maximum, almost a shoulder, at ~ 0.65 eV. The decrease of the position of this peak from compressive to tensile strain displayed in Fig. 3.19c is qualitatively captured by the DFT calculations which are presented in the following.

3.4 Strain dependence of the optical conductivity

In the theoretical spectra (Fig. 3.19b) we also see that the minimum at ~ 0.5 eV is constant for negative strain, and starts to fill up for positive strain.

We have performed electronic band structure calculations using density functional theory (DFT), and display the computed optical conductivities of this compound in the aforementioned range of strain values in Fig. 3.19b. A film of LaNiO_3 was simulated using a $C2/c$ unit cell, which corresponds to $a^-a^-c^-$ octahedral rotation pattern in Glazer notation [181]. The primitive cell of this structure contains four formula units with oppositely oriented tilts and rotations of the NiO_6 octahedra. The strain effect of the substrate was taken into account by constraining the in-plane pseudo-cubic vectors $\mathbf{a}_p, \mathbf{b}_p$ to the corresponding vectors of a generic cubic substrate. The strain values are defined with respect to the lattice constant of the PBE-relaxed bulk structure ($a_p \approx 3.863\text{\AA}$). We used the method of Ref. [61]. The in-plane lattice parameters were fixed and all other degrees of freedom, such as the out-of-plane lattice vector, oxygen, and cation positions, are allowed to relax. For most of the strains, except for the very large ones, the final space group of the relaxed unit cell remained $C2/c$. For the extreme compressive strain (-4.0%) with vanishing \mathbf{a} -, \mathbf{b} -rotation angles, $\alpha = \beta = 0^\circ$, and for the extreme tensile strain (+5.0%) with $\gamma = 0^\circ$ the relaxation converged to unit cells corresponding to supergroups of $C2/c$: $I4/mcm$ under compression and $Fmmm$ under tension. Crystal structure relaxation was performed within the generalized gradient approximation (Perdew-Burke-Ernzerhof parametrization, PBE) [182] using the projected-augmented waves (PAW) method [183] as implemented in the Vienna Ab-initio Simulation Package (VASP) [184–186]. The integration over the Brillouin zone was done using a k -mesh with $11 \times 11 \times 11$ points and a plane-wave cutoff of $E_{\text{cut}} = 600$ eV. Structure relaxation was considered converged when the forces were smaller than 10^{-3} eV/ \AA .

In Fig. 3.20 we show the resulting density of states and the band structure along a high symmetry path through the Brillouin zone for three different strains.

To evaluate the orbital character of the band structure, as shown in Fig. 3.20d-f, we projected the Kohn-Sham wavefunctions onto e_g -like ($d_{z^2}, d_{x^2-y^2}$) local states centered on the Ni atoms. We selected band states in a narrow energy window ($[-1.6, 4.0]$ eV) around the Fermi level, corresponding to antibonding states in the local frame of octahedra, which are then transformed into projected localized orbitals (PLOs) as defined in Refs. [187, 188].

Optical conductivities for the relaxed structures have been calculated using WIEN2k [189] and the transport code implemented in the TRIQS/DFTTools package [190], which is based on the TRIQS library [191]. We used a denser

3. Optical properties of LaNiO₃ films tuned from compressive to tensile strain.

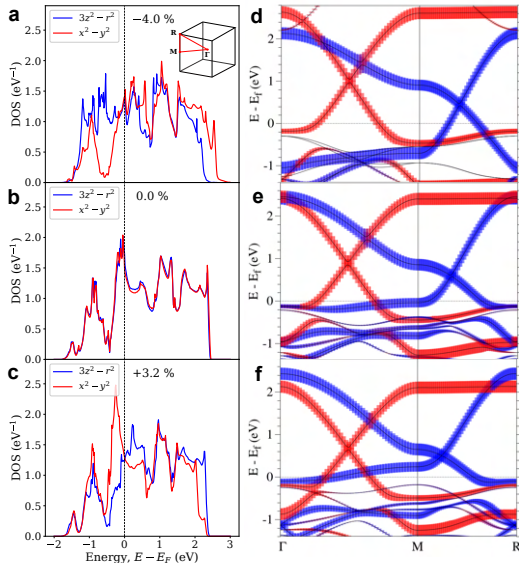


Figure 3.20: **a-c**, DFT density of states projected on d_{z^2} (blue) and $d_{x^2-y^2}$ (red) orbitals. **d-f** energy momentum dispersion along the trajectory shown in the inset of **a**, with orbital character for three different strain values: -4.0% (**a**, **d**), 0.0% (**b**, **e**), +3.2% (**c**, **f**).

k -mesh of $33 \times 33 \times 33$ points and assumed a fixed scattering rate of $\hbar/\tau=60$ meV for all strains. The DC conductivity was calculated from the relation $\sigma_{DC} = \tau\omega_p^2/(4\pi)$, where ω_p^2 is the spectral weight tensor defined as

$$\omega_p^2 = \frac{4\pi e^2}{\Omega_{pc}} \sum_{\mathbf{k}, j}^{1^{st} BZ} \mathbf{v}_j(\mathbf{k})\mathbf{v}_j(\mathbf{k}) \left(-\frac{\partial f_{\mathbf{k},j}}{\partial \epsilon_{\mathbf{k},j}} \right), \quad (3.40)$$

$\mathbf{v}_j(\mathbf{k})$ is the group velocity of the j 'th band for momentum value \mathbf{k} , Ω_{pc} is the volume of the primitive cell, and $f_{\mathbf{k},j} = 1/[1 + \exp\{(\epsilon_{\mathbf{k},j}/k_B T)\}]$ is the Fermi-Dirac distribution. We see that the overall frequency dependence of the experimental data in Fig. 3.19a as a function of strain is qualitatively well accounted for by the DFT results.

To demonstrate the effect of oxygen-octahedra rotations and tilts on the electronic properties, we also performed calculations for (hypothetical) undistorted $P4/mmm$ tetragonal structures using the in- and out-of-plane lattice constants of the fully relaxed distorted structures.

By comparing to calculations for this hypothetical structure without NiO₆

3.4 Strain dependence of the optical conductivity

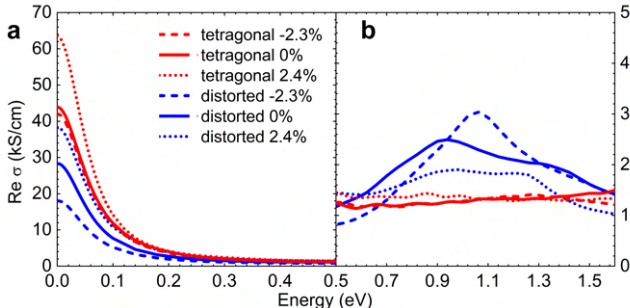


Figure 3.21: Calculated DFT optical conductivity **a**, below and **b**, above 0.5 eV of tetragonal structures without oxygen-octahedra rotations and tilts (red) compared to the fully distorted structures (blue) at -2.3% (dashed), 0.0% (solid) and +2.4% (dotted) strains assuming a fixed scattering rate of $\hbar/\tau = 60$ meV.

octahedral distortions (see Fig. 3.21), we obtain direct evidence that the broad peak around 1 eV is due to optical inter-band transitions, being allowed as a result of the band-backfolding occurring in the distorted structure. Indeed, this feature is due to octahedral distortions, rotations, and tilts as well as symmetry lowering and presence of two Ni atoms per unit cell which leads to a pronounced weight in the optical conductivity observed in theory and experiment (Fig. 3.19). This optical transition therefore does not occur in the undistorted tetragonal structure. In the low-frequency region of the optical conductivity we observe two effects: First, the DC conductivities are larger for the tetragonal structures, due to larger inter-site hoppings as a result of straight bonds. Second, the trend of a conductivity decrease under increased strain is still present (although only weakly pronounced for tensile strains), which can be traced back to how the crystal-field splitting evolves under strain. Evolution of inter-site hoppings and crystal-field splitting as a function of strain are shown below in Fig. 3.24).

3. Optical properties of LaNiO₃ films tuned from compressive to tensile strain.

3.5 Spectral weight and mass enhancement

From experimental and calculated optical conductivities, we determined the integrated spectral weight, defined as:

$$W(\Omega) = \frac{4\pi\hbar^2 e^2}{m_e V_{fu}} N_{eff}(\Omega) = 8\hbar^2 \int_0^\Omega \text{Re } \sigma(\omega) d\omega \quad (3.41)$$

where V_{fu} is the volume occupied by one formula unit, \hbar the reduced Planck constant, e and m_e the electron charge and mass respectively. The resulting experimental and theoretical effective number of carriers $N_{eff}(\Omega)$ are displayed in Fig. 3.22a-e.

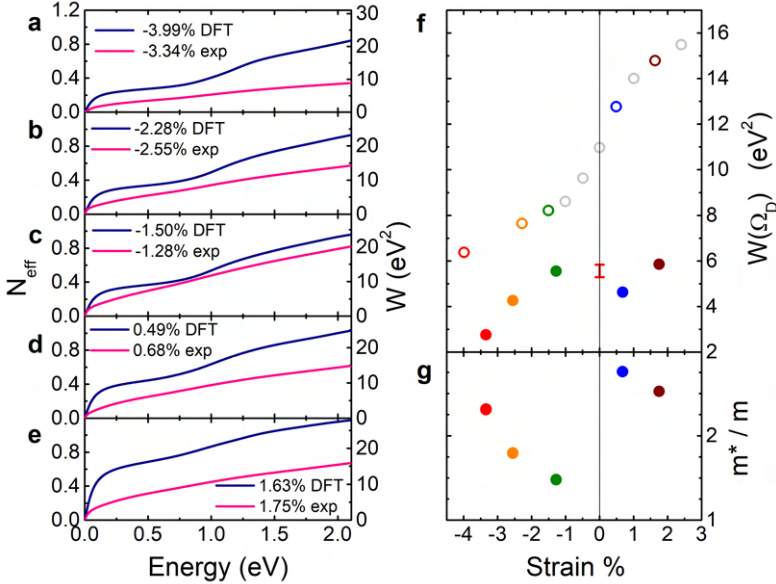


Figure 3.22: a-e Optical spectral weight W as a function of frequency from experiment at 10 K and DFT calculations for each strain value. f, Experimental (closed symbols), and DFT (open symbols) evolution of the free carrier spectral weight $W(\Omega_D)$ of LaNiO₃ films as a function of strain. For the theoretical values of -3.99% strain the calculated crystal structure is $I4/mcm$; for all other strain values the structure converged to $C2/c$. The error bar applies to all experimental points and was determined by repeating the Kramers-Kronig analysis after multiplying the reflectivity with 1 ± 0.05 . g, Strain dependence of the effective mass according to Eq. 3.42.

3.5 Spectral weight and mass enhancement

By virtue of the f -sum rule the limiting value of $N_{eff}(\Omega)$ for $\Omega \rightarrow \infty$ corresponds to the number of electrons per formula unit, and the spectral weight in this limit corresponds to the squared plasma frequency of all (core and conduction) electrons: $W(\infty) = \hbar^2 \omega_p^2$. Of particular interest is the spectral weight of the narrow Drude peak, corresponding to $W(\Omega_D)$, taking $\Omega_D = 0.35$ eV which is well above the Drude width $1/\tau^*$ but small enough not to include interband transitions and mid-infrared spectral weight. The values of $W(\Omega_D)$ as a function of strain are displayed in Fig. 3.22f. A key observation is that experiment and computation both display an overall increase of the Drude weight $W(\Omega_D)$ (Fig. 3.22f) by approximately a factor of two when going from the most compressive to the most tensile strain. For experiment, it increases from most compressive -3.34% to -1.3% strain, suddenly drops between -1.3% and +0.68% and then increases again when the tensile strain increases to 1.75%. This trend may appear as counter-intuitive: one might have expected an overall decrease of the inter-atomic in-plane hopping strength, and hence of $W(\Omega_D)$, when atoms get farther away from one another under tensile strain. Our DFT calculations correspondingly yield the opposite trend of a decrease of the out-of-plane Drude weight and conductivity from compressive to tensile (see Fig. 3.24), a prediction which we leave for future experimental confirmation. Explaining these apparently counter-intuitive trends is one of the main emphases of this study.

A striking feature of the DFT calculations – absent from the experimental data – is the sharp increase between -1% and +1% strain. The experimental values even show a slight dip at +0.7% strain.¹ The other observation from Fig. 3.22f is that the experimental Drude weight is systematically smaller than the DFT computed value, leading to effective masses of around two: this is a hallmark of correlation effects. These two observations are not limited to the low-frequency Drude weight but apply to the integrated spectral weight $W(\Omega)$ for all measured frequencies, as shown in Fig. 3.22a-e.

To analyze this further it is of interest to make an estimate of the mass enhancement by comparing the measured and calculated spectral weights of

¹Since the measured optical response depends on the film thickness, one may suspect that this discrepancy could result from assuming the wrong value for the film thickness, or from the presence of a dead (*i.e.* insulating) layer. However, the thicknesses of these films are accurately known from X-ray diffraction. Since even for the insulating phase of RNiO₃ the spectral weight in the visible part of the spectrum is not so different from the metallic phase [62], the assumption of a dead layer cannot explain the low value of $N_{eff}(2\text{eV})$ for the tensile samples. Moreover, transport experiments on films on LaAlO₃ as a function of film thickness have demonstrated that the films switch as a whole from metal to insulator at a critical thickness [68].

3. Optical properties of LaNiO₃ films tuned from compressive to tensile strain.

the Drude peak:

$$\frac{m^*}{m} = \frac{W_{\text{DFT}}(\Omega_D)}{W_{\text{EXP}}(\Omega_D)}. \quad (3.42)$$

The mass enhancement, shown in Fig. 3.22g, is between about 1.5 and 3.0, consistent with previous reports [54, 56, 192]. Based on dynamical mean-field theory calculations, this is the expected range of mass enhancements resulting from the on-site Hubbard and Hund’s rule interactions in these compounds [54, 56, 61, 129, 150, 193]. Most members of the RNiO₃ family exhibit a metal-insulator transition which has been characterized as a ‘site selective’ Mott transition [122, 125]. While LaNiO₃ remains metallic at all temperatures, it is overwhelmingly natural to assume that the Hubbard U and Hund’s J -interaction play an important role in the physical properties of this material. One of the most typical consequences of the on-site interaction is a transfer of optical spectral weight from the free carrier response of the Ni $3d$ band to high energy [151]. Consequently most of the missing free carrier spectral weight is recovered in the oxygen- $2p$ to Ni- $3d$ transitions which span over approximately 10 eV. The fact that in Fig. 3.22a-e the spectral weight difference between experiment and DFT persists up to 2 eV is therefore a strong indication that the low energy spectral weight is suppressed by the Hubbard U and Hund’s J -interaction.

3.6 Strain dependence of the electronic structure

In order to understand the evolution of the electronic structure as a function of strain, we now turn to an in-depth analysis of how the structural changes evolve as a function of strain and, in turn, how they affect electronic structure as computed from DFT – this is the focus of Figs. 3.23 and 3.26.

The first important consideration is a structural one. Fig. 3.23a displays the strain dependence of the rotations of the NiO₆ octahedra with respect to the (x, y) axis (‘tilts’) and with respect to the z -axis (‘rotations’), as obtained from our DFT structural relaxation calculations. As reported in previous work [61, 96], tensile strain promotes tilts and suppresses rotations, while compressive strain has the opposite effect. As a consequence, tensile strain distorts the out-of-plane Ni-O-Ni bond, keeping the in-plane bond angles almost unchanged [194], making the (oxygen mediated) effective nickel-nickel in-plane hopping more favorable than the out-of-plane hopping.

To calculate the hopping ratios t_{ab}/t_c , shown in Fig. 3.23ad, we constructed a low-energy Wannier Hamiltonian on a $10 \times 10 \times 10$ k-grid using maximally-localized Wannier functions [195–197] of Ni-centered orbitals of e_g symmetry. For all strains we used a frozen energy window ([0.04,0.74] eV)

3.6 Strain dependence of the electronic structure

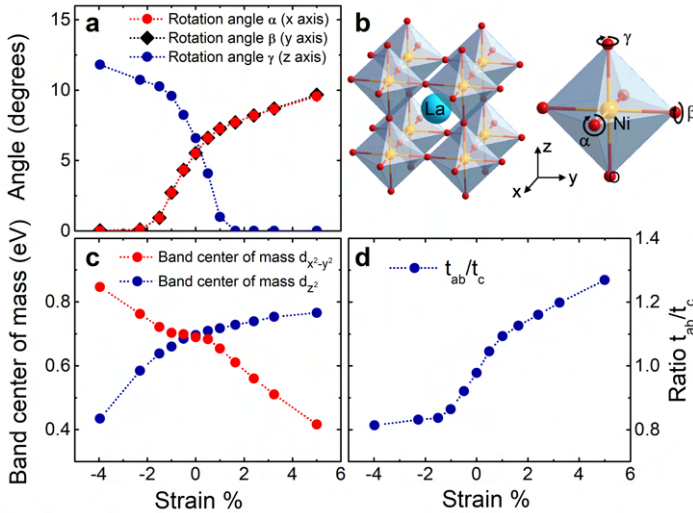


Figure 3.23: **a**, Rotation of the oxygen octahedra along the x and y axis (corresponding to out-of-plane tilts α and β) and along the z axis (corresponding to the in-plane rotation angle γ) extracted from the relaxed DFT crystal structures. Note that the values of α and β are very close. **b**, Unit cell of LaNiO_3 and illustration of the tilt axes. **c**, Evolution of the intra- e_g crystal field splitting, evaluated from the projected DFT density of states as a function of strain. **d**, Calculated ratio of the in-plane to out-of plane hopping amplitudes as a function of strain.

to improve the quality of the Wannier fit. We checked that the Wannier functions are centered exactly on the atomic positions and confirmed that the resulting Wannier Hamiltonian is real. However, it should be noted that the employed e_g -like basis is not sufficient to accurately match the band structure for states below the frozen energy. From the Wannier model we extracted the on-site energies (Fig. 3.24c), which show the same trend as the band center of mass shown Fig. 3.23 c. Additionally, we calculated effective in-plane t_{ab} and out-of-plane t_c hopping amplitudes (Fig. 3.24b) via

$$\begin{aligned}
 t_{ab} &= \sum_{\mathbf{R} \in \{ab\}} \frac{\sqrt{\sum_{i,j} |t_{i,j}(\mathbf{R})|^2}}{N_{|\mathbf{R}|}} \\
 t_c &= \sum_{\mathbf{R} \in \{c\}} \frac{\sqrt{\sum_{i,j} |t_{i,j}(\mathbf{R})|^2}}{N_{|\mathbf{R}|}}
 \end{aligned} \tag{3.43}$$

For t_{ab} the sum runs over all real-space vectors $\mathbf{R} \in \{ab\}$ without any out-of-plane component and without any in-plane components for t_c , respectively.

3. Optical properties of LaNiO_3 films tuned from compressive to tensile strain.

The indices $i, j \in \{z^2, x^2 - y^2\}$ are orbital indices and $N_{|\mathbf{R}|}$ is the number of Ni-atoms at the same distance $|\mathbf{R}|$, *e.g.* there are two nearest neighbor out-of-plane hoppings and four nearest neighbor in-plane hoppings. Under tensile strain the in-plane DC conductivity increases. In the calculations, the out-of-plane DC conductivity shows the exact opposite behavior, it decreases under tensile strain (see Fig. 3.24a).

Fig. 3.23d displays the ratio of in-plane to out-of-plane Ni-Ni effective hopping t_{ab}/t_c . This ratio is seen to increase from about 0.8 to 1.2 when going from compressive to tensile strain. At the same time, the compression of the c -axis under tensile strain leads to an energetic destabilization of the out-of-plane antibonding d_{z^2} orbital in comparison to the in-plane $d_{x^2-y^2}$ one.

Fig. 3.23c displays the intra- e_g crystal field splitting $\Delta_c \equiv \varepsilon(x^2 - y^2) - \varepsilon(z^2)$ (relative stabilization energy of the in-plane orbital), defined from the center of mass of each band (the first moment), which is negative for tensile strain and positive for compressive strain. Both effects, the favoring of the in-plane hopping and the stabilization of the $d_{x^2-y^2}$ orbital, give rise to an increase of the conductivity when going from compressive to tensile strain (Fig. 3.24a).

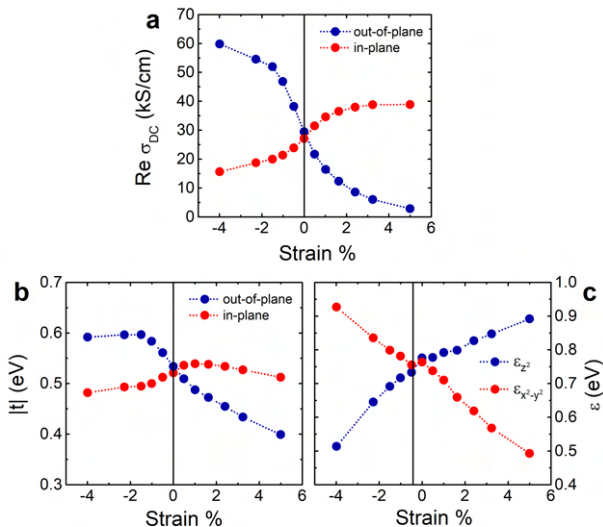


Figure 3.24: **a**, Calculated strain dependence of the in-plane (red) and out-of-plane (blue) DC conductivity using a fixed scattering rate of $\hbar/\tau=60$ meV. **b**, Wannier model effective in-plane t_{ab} (red) and out-of-plane t_c (blue) hopping amplitudes. **c**, on-site energies of the d_{z^2} (blue) and $d_{x^2-y^2}$ (red) Wannier orbitals.

3.6 Strain dependence of the electronic structure

These considerations provide an insight into the important factors to explain the behavior of the conductivity. However, the low-frequency (Drude) part of the spectral weight is essentially a Fermi surface property, and the observed changes in the optical response therefore motivate a detailed analysis of the DFT Fermi surface.

In Fig. 3.25 we show the effect on the Fermi surface and the velocities when tuning the crystal field splitting Δ_c and the hopping ratio t_{ab}/t_c starting from the unstrained tetragonal structure (middle column). Note that the

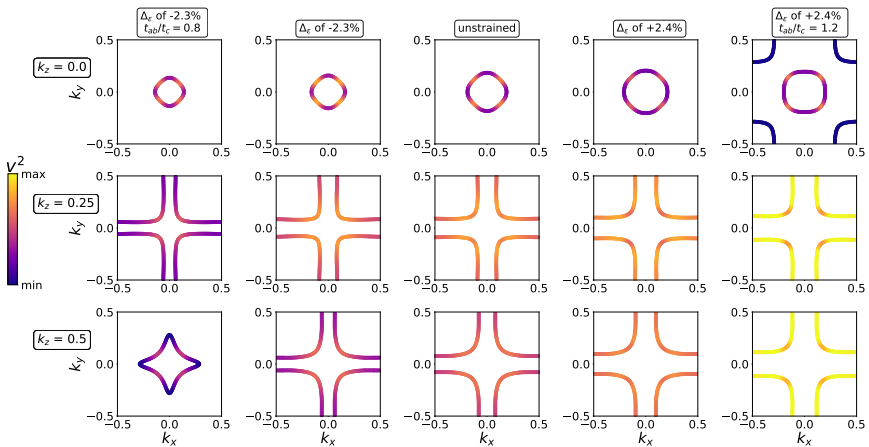


Figure 3.25: Fermi surface of the unstrained tetragonal structure without octahedral rotations and tilts calculated with DFT and a subsequent Wannier model construction (middle column). The second and fourth columns show the Fermi surface of the same model, but with the crystal-field splitting Δ_c of -2.3% and +2.4% tetragonal structures, respectively. The first and last columns show the effect of scaling the hopping ratio t_{ab}/t_c by 0.8 and 1.2 in addition to the modified Δ_c . Each row corresponds to a different value of the out-of-plane momentum k_z (in units of π/c). Along each Fermi surface sheet the magnitude of the in-plane Fermi velocity $v_x^2 + v_y^2$ is color-coded. Note that the additional sheets visible in Fig. 3.26 are Fermi surface reconstructions due to a two Ni-atom (twice as large) unit cell.

additional sheets visible in Fig. 3.26 are Fermi surface reconstructions due to a two Ni-atom (twice as large) unit cell. Only if both the change in Δ_c and the change in t_{ab}/t_c are accounted for (first and last column) can the Lifshitz transitions under strain be qualitatively reproduced.

3. Optical properties of LaNiO_3 films tuned from compressive to tensile strain.

The changes in Δ_c and t_{ab}/t_c also lead to higher in-plane velocities, when adjusted in accordance with the effect of tensile strain (i.e. Δ_c decreases and t_{ab}/t_c increases), as seen from the color-coding of the Fermi surfaces. We encourage the reader to further explore the effect of Δ_c and t_{ab}/t_c on the Fermi surface and the band structure with our interactive online applet (Ref. [198]). The in-plane velocities of the states on the Fermi surfaces, shown in Fig. 3.25 and Fig. 3.26 have been calculated with the BoltzTraP2 software package [199].

In Fig. 3.26 we display the calculated Fermi surfaces for five values of strain, as in-plane (k_x, k_y) cuts for three different values of the out-of-plane momentum k_z . The striking observation is that a transition in the topology

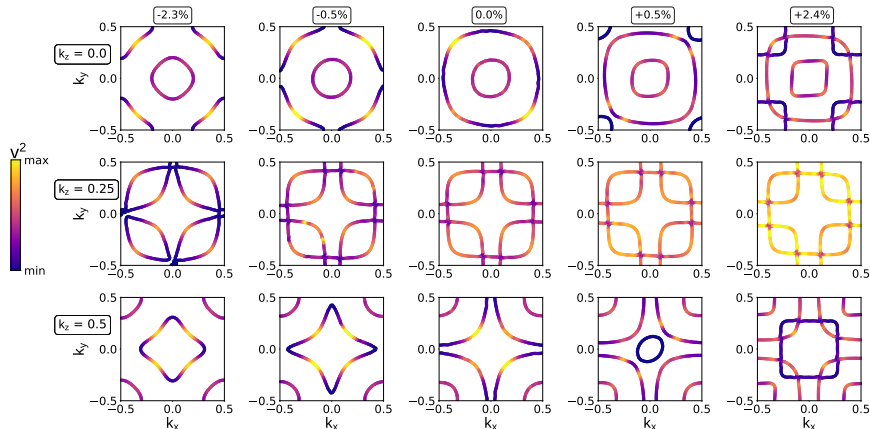


Figure 3.26: DFT Fermi surface for 5 values of strain (columns). Each row corresponds to a different value of the out-of-plane momentum k_z (in units of π/c). The Lifshitz transition is manifest when a small compressive (see $k_z = 0.5$) or tensile (see $k_z = 0.0$) strain is applied. Along each Fermi surface sheet, the magnitude of the in-plane Fermi velocity $v_x^2 + v_y^2$ is color-coded, demonstrating the overall increase of the in-plane velocity under tensile strain.

of the Fermi surface (Lifshitz transition) is found as soon as a small strain is applied to the unstrained compound, for both compressive and tensile strain. Focusing for example on the $k_z = 0$ cut, we see that an additional Fermi surface sheet appears at the zone corner when a small tensile strain is applied, while the outer Fermi surface sheet switches from closed to open (i.e from Γ -centered to X -centered) under compressive strain. We have calculated the magnitude of the in-plane electronic velocity $v_x^2(\mathbf{k}) + v_y^2(\mathbf{k})$ as the momentum \mathbf{k} varies along each Fermi surface sheet, and displayed the result in Fig. 3.26 as a color intensity map. This reveals the considerable

3.6 Strain dependence of the electronic structure

increase of the in-plane velocity from compressive to tensile strain, especially visible e.g. for the $k_z = 0.25 \pi/c$ cut.

Overall, our calculated Fermi surfaces are in good agreement with the ARPES data of Yoo *et al.* [150]. Comparing the images in panels (c) and (d) of Fig. 3 from Ref. [150] (corresponding to compressive and tensile strains, respectively), one can clearly see at least one signature of the Lifshitz transition. Specifically, on going from compressive to tensile strain, a pocket at point M (folded to point Z) emerges. This is exactly the picture one can infer from our Fig. 3.26 ($k_z = 0.5 \pi/c$ cut, strains from -2.3 % to +2.4 %). Another notable feature is a star-shaped sheet visible both in our Fig. 3.26 ($k_z = 0.5 \pi/c$ cut, strains -0.5 % and -2.3 %) and in Fig. 3(c) of Ref. [150] displaying the ZRA plane. It seems to us that the precise topology of this sheet is harder to determine unambiguously from the reported ARPES data. This sheet is definitely open at tensile strains and its neck is defined by a flat band close to the Fermi level (the band along ZR in Fig. 1 of Ref. [150] and the d_{z^2} -like band along ΓM in our Fig. 3.20). Both in our DFT results and in ARPES the band moves up when going from tensile to compressive strain. However, while in our calculations it clearly crosses the Fermi level at a strain slightly below zero, thus closing the star-shaped sheet, its fate is less clear in ARPES data at -1.3 % strain. Yoo *et al.* infer the band position from the maxima of the energy-distribution curves (EDCs) and the results shown in Fig. 1 of Ref. [150] indicate that at -1.3 % the ZR -band is still below the Fermi level. However, the band is very flat and lies very close to the Fermi level, and a more detailed analysis of the data may be necessary. Nevertheless, the comparison of trends observed in our calculations and in ARPES suggests that the star-shaped sheet closes at some value of the strain on the compressive side, even if slightly below -1.3 % strain. Hence we conclude that there is overall reasonable qualitative agreement between our results and the ARPES data and a clear indication of a Fermi surface Lifshitz transition.

The strain dependence of the two key electronic structure parameters Δ_c and t_{ab}/t_c can be directly connected to the evolution of the Fermi surface topology. We show that by starting from an e_g Wannier model for the (hypothetical) $P4/mmm$ tetragonal structure without octahedral rotations and tilts, the calculated DFT trends in the Fermi surface can be semi-quantitatively explained when these two parameters are varied. We emphasize that the evolution of the hopping anisotropy (t_{ab}/t_c) and the change in the crystal-field splitting (Δ_c) both result, when taken into account separately, in a decrease of the Drude weight when strain is increased. However, the magnitude of the changes seen in the conductivity (factor of two), as well as the evolution of the Fermi surface, can only be understood when both ingredients are considered together.

Taken together, our findings on the calculated electronic structure provide

3. Optical properties of LaNiO_3 films tuned from compressive to tensile strain.

a consistent explanation of the overall trends for the strain dependence of the optical spectra, and in particular explain why tensile strain leads to an increase of the Drude weight and optical conductivity. We note that a Lifshitz Fermi surface transition under strain has indeed been observed by ARPES spectroscopy for this material [150].

3.7 Conclusions

In conclusion, we combined optical data of strained LaNiO_3 thin films, ranging from highly compressive (-3.34%) to moderate tensile (+1.75%) strain, on a large frequency range from around 1 meV to 4 eV, using different optical techniques. The data were fitted using a Drude-Lorentz model and two Drude peaks was necessary to approximate the frequency dependant scattering rate due to electron-electron correlations. Our optical measurements reveal a remarkable sensitivity of the electronic structure of LaNiO_3 to strain. In contrast to naive intuition, the in-plane low-frequency Drude weight increases by a factor close to two when we lattice-tune the material from highly compressive (-3.34%) to moderate tensile (+1.75%) biaxial strain. We performed density functional theory calculations which reveal that these effects are due to drastic changes of the electronic structure under strain, caused by the changes in tilts and rotations of the NiO_6 octahedra. Our DFT calculations reveal a topological change of the Fermi surface (Lifshitz transition), which strongly modifies the velocity of carriers on the different Fermi surface sheets. We have provided a simple explanation of the evolution of the topology of the Fermi surface and of these trends, based on the changes of both the crystal field splitting and ratio of in-plane to out-of-plane hopping under strain. A prediction of our theory is that the Drude weight associated with the out-of-plane conductivity should correspondingly decrease from compressive to tensile strain. Our experimental results also reveal that interaction effects are sensitive to strain, with an enhancement factor of the optical effective mass ranging between about 1.5 and 3.0. The evolution of the electronic structure ultimately results from the structural changes under strain (rotations, tilts and c/a aspect ratio of the octahedra), illustrating the rich interplay between structural and electronic aspects of transition-metal oxides. This interplay can be leveraged in tuning electronic functionalities of oxides by strain engineering. Strain tuning of the electronic structure of LaNiO_3 and the detailed theoretical description thereof provide important tools for extending the use of this material in applications such as electrodes, gas-sensing and catalysis [200].

Raman spectroscopic evidence for multiferroicity in rare earth nickelate single crystals

In this chapter, we discuss Raman spectroscopic measurements taken on RNiO_3 single crystals ($R = \text{Y, Er, Ho, Dy, Sm, Nd}$) for temperatures from 10 K to very high temperatures, close to the melting point of materials. We probed the metal-insulator and the magnetic transition with respect to the evolution of the phonons modes and the electronic Raman continuum. Below the Neel temperature, the appearance of additional phonon modes indicates a symmetry breaking that is associated with the appearance of a ferroelectric phase and therefore an indirect evidence of multiferroicity in these compounds. Using Density-Functional theory we calculate the IR and Raman active phonons of YNiO_3 to compare with our experimental results. This chapter starts with a general introduction to Raman spectroscopy followed by a description of the used Raman spectrometer and the presentation of the six measured samples. The results of the metal-insulator transition are discussed in the context of the overall trend of the mode frequencies and the decrease of the electronic background. Entering the magnetically ordered phase, we discuss the appearance of the magnetic resonance as well as a large number of additional vibrational modes, implying a breaking of inversion symmetry expected for multiferroic order. We show also the impact of pressure on SmNiO_3 and NdNiO_3 which reveal an insulator-metal transition and an orthorhombic-rhombohedral phase transition, respectively. This chapter has been adopted with small modifications from Physical Review Research 3, 033007 (2021), I.Ardizzone, J.Teyssier, I.Crassee, A.B.Kuzmenko, D.G.

4. Raman spectroscopic evidence for multiferroicity in rare earth nickelate single crystals

Mazzone, D.J.Gawryluk, M.Medarde, D.van der Marel [83].

4.1 Introduction

So far, experimental evidence for multiferroicity in nickelates is inexistent. However, first principles electronic band structure calculations predict that the combination of breathing distortion and non-centrosymmetric magnetic order can induce an inversion symmetry breaking also in the crystal lattice and thus induce an electric dipole, making nickelates type-II multiferroics [46–48, 50–53, 162, 201, 202]. For example, $\uparrow\uparrow\downarrow$ magnetic ordering in TlNiO_3 [50] and TmNiO_3 [53] has been predicted to induce a large effective ionic displacement from site-centered to partially bond-centered, while the asymmetric bonding between lead and oxygen in PbNiO_3 [201] has been predicted to drive a polar displacement along the [111]-direction. This ionic displacement and symmetry breaking combined with magnetic order make them all potential multiferroic materials. For rare earth nickelates, experimental confirmation of this idea has been inhibited by the unavailability of single crystals. The Paul Scherrer Institut (PSI) offered us the opportunity to measure the first ever reported nickelate single crystals of extremely high quality. As the size of the crystals is of only a few micrometers, infrared measurement is elusive and Raman spectroscopy is a perfectly suited technique to probe a possible symmetry breaking at the metal-insulator and magnetic transition. Raman spectroscopy is extremely sensitive to small changes of the crystal symmetry as it detects: (i) the phonon spectrum and (ii) the activation or deactivation of modes through optical selection rules. For example, Raman spectroscopy was able to reveal a ferroelectric state in KH_2PO_4 (KDP) [203] and SrTiO_3 [204] by direct observation of the ferroelectric polar mode and its softening at the ferroelectric transition. Raman scattering can also probe magneto-electric excitations, as in the manganite perovskite TbMnO_3 [205] in which the intermediate type of charge ordering between site-centered and bond centered leads to a lack of inversion symmetry [206]. Here the spiral spin ordering driven by Dzyaloshinskii-Moriya interaction induces a displacement of oxygen ions and thus a symmetry breaking. Raman spectroscopy was intensively used to study samarium and neodymium nickelate thin films [207, 208]. A large rearrangement of the phonon spectrum is observed at the structural (metal-insulator) transition, but indications of inversion symmetry breaking were not noticed in these works.

In the present study, we collected Raman spectra on six different single crystals of the chemical composition RNiO_3 with $\text{R}=\text{Y, Er, Dy, Ho, Sm}$ and Nd in a broad range of temperatures. We monitored the change

of the spectroscopic features as the materials pass through three different phases, namely the metallic phase at high temperatures, the paramagnetic insulating phase at intermediate temperatures, and the magnetically ordered phase at low temperatures. Entering the magnetically ordered phase we observe the appearance of a large number of additional vibrational modes, implying a lowering of the symmetry and a breaking of the centrosymmetry according to factor group analysis expected for multiferroic order. A recent investigation [209] of neutron and X-ray diffraction on the same crystals has indeed reported the existence of pronounced lattice anomalies at T_N .

4.2 Raman spectroscopy

Raman scattering spectroscopy is an optical measurement technique that uses scattered light to probe electronic, magnetic and vibrational excitations of matter.

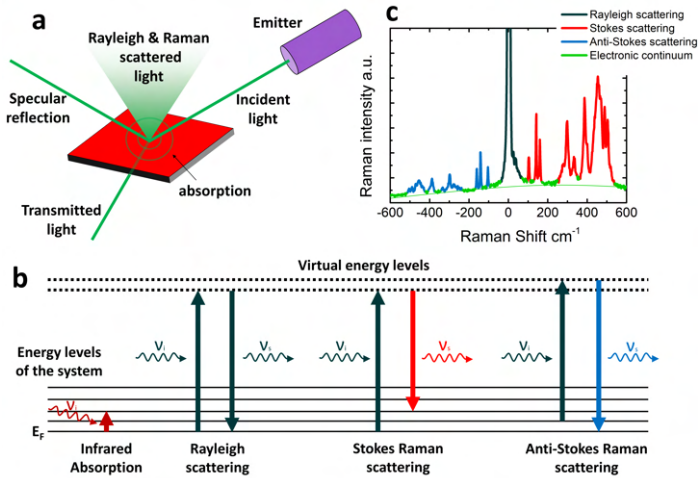


Figure 4.1: **a**, Illustration of the different interaction between light and matter. Raman spectroscopy measures the scattered light. **b**, Infrared absorption compared to the different scattering process (Rayleigh scattering $\nu_i = \nu_s$, Stokes scattering $\nu_i > \nu_s$ and anti-Stokes scattering $\nu_i < \nu_s$). **c**, Example of DyNiO_3 Raman spectra with Rayleigh scattering (dark), Stokes signal composed of phonons (red), anti-Stokes response (blue) and the Raman continuum (green).

While elastic specular reflection and transmitted light give information on the direct dipole excitations described in the section 3.2, Raman spectroscopy is based on the study of the inelastic scattered light shown in figure 4.1a. Figure 4.1b summarizes the different scattering processes compared to the

4. Raman spectroscopic evidence for multiferroicity in rare earth nickelate single crystals

direct dipole excitation. In the case of infrared absorption (direct dipole transition), the system passes from a low to high energy level by absorbing a photon with a frequency ν corresponding to the difference between these two levels. For elastic scattering, called Rayleigh scattering, the system absorbs the photon, is excited to a virtual energy level, and return to the same initial energy level while emitting a photon with the same frequency $\nu_s = \nu_i$. For example, the blue color of the sky is the result of blue light scattered by Rayleigh process from molecules and small particles in the atmosphere. For inelastic scattering, the system absorbs the high-energy photon of frequency ν_i , but when it relaxes, it emits a photon of lower frequency $\nu_s < \nu_i$ or of higher frequency $\nu_s > \nu_i$ than the initial one. These processes are called Stokes and anti-Stokes scattering respectively. For anti-Stokes scattering, electrons are excited from a thermally occupied states. The Raman shift corresponding to the difference between the incident and the scattered photon is defined by:

$$\Delta\nu = \nu_i - \nu_s \quad (4.1)$$

Spatial fluctuations (crystal inhomogeneities) induce Rayleigh scattering, while temporal fluctuations (phonons, spin waves, electronic charge fluctuations) create inelastic scattering. Figure 4.1c shows the spectrum of DyNiO₃ Raman measurement from -600 to 600 cm⁻¹ at 305 K. Rayleigh scattering is presented in dark. The Rayleigh signal is 10⁶ to 10⁹ more intense than the Raman signal. We will show in Section 4.2.4 that it is essential to suppress the Rayleigh peak to have access to the inelastic signal. The Stokes signal composed of many phonons is shown in red in Fig. 4.1c, while the anti-Stokes signal shown in blue reveals the same features with intensity modulated by thermal occupation (Bose-Einstein statistics factor).

The measured Raman intensity is related to the Raman susceptibility $\chi = \chi' + i\chi''$, which is described in the next section. This intensity is a combination of two processes: The peaks shown in figure 4.1c, except the Rayleigh peak, are due to the excitation of electrons (to virtual energy states) which scatter over the system, giving (Stokes) or taking (anti-Stokes) energy and momentum to collective excitations such as phonons (lattice vibration) or magnons (spin excitations) before relaxation. The electronic background, called Raman continuum, shown in green in the figure 4.1c is caused by the excitation of a continuum of electron-hole pairs around the Fermi level. This process is related to the optical conductivity by $\chi'' \propto \omega\sigma_1(\omega)$. The electronic process is usually weaker than the Raman signal from phonons.

4.2.1 Raman process

From a classical point of view, we can relate Raman processes to the polarization of the material induced by an external electric field $\mathbf{P} = \epsilon_0 \chi_e \mathbf{E}_i$ with χ_e the electric susceptibility of the material and \mathbf{E}_i the initial alternative electric field ($\mathbf{E}_i = E_0 \cos(\mathbf{k}_i \cdot \mathbf{r} - \omega_i t) \mathbf{e}_i$ with \mathbf{e}_i an unitary vector $\parallel \mathbf{E}_i$). Fluctuation in the material such as phonons or magnons can be described as:

$$\mathbf{Q} = \mathbf{Q}_0 \cos(\mathbf{q} \cdot \mathbf{r} - \nu t) \quad (4.2)$$

Thus, linear response theory allows to express the modulation of the susceptibility χ_e induced by the fluctuations:

$$\chi_e = \chi_{e0} + \left(\frac{\partial \chi_e}{\partial \mathbf{Q}} \right)_0 \mathbf{Q} \quad (4.3)$$

The polarization is therefore defined as:

$$\begin{aligned} \mathbf{P} = & \epsilon_0 E_0 \mathbf{e}_i \chi_{0e} \cos(\mathbf{k}_i \cdot \mathbf{r} - \nu_i t) \\ & + \frac{\epsilon_0 E_0 \mathbf{e}_i \mathbf{Q}_0}{2} \left(\frac{\partial \chi_e}{\partial \mathbf{Q}} \right)_0 \cos[(\mathbf{k}_i - \mathbf{q}) \cdot \mathbf{r} - (\nu_i - \nu) t] \\ & + \frac{\epsilon_0 E_0 \mathbf{e}_i \mathbf{Q}_0}{2} \left(\frac{\partial \chi_e}{\partial \mathbf{Q}} \right)_0 \cos[(\mathbf{k}_i + \mathbf{q}) \cdot \mathbf{r} - (\nu_i + \nu) t] \end{aligned} \quad (4.4)$$

It can be seen that the first term does not depend on the frequency ν of the collective excitation and describes elastic scattering. The two other terms take into account the temporal fluctuations of the electric susceptibility. The term with $(\nu_i - \nu)$ accounts for the Stokes response, the term with $(\nu_i + \nu)$ contributes the anti-Stokes signal. Inelastic scattering thus occurs for $\frac{\partial \chi_e}{\partial \mathbf{Q}} \neq 0$.

The Raman excitation phenomenon can also be described in a local classical point of view by the variation of the polarizability α . The polarizability α is a local quantity and defines the ability of the electronic cloud to deform under the effect of an electric field. Therefore, considering a fluctuation \mathbf{Q} as above, the Raman scattering occurs when $\frac{\partial \alpha}{\partial \mathbf{Q}} \neq 0$. The polarizability α is easier to illustrate spatially than the susceptibility χ_e and therefore will be used in the section 4.2.2.

4. Raman spectroscopic evidence for multiferroicity in rare earth nickelate single crystals

From a quantum point of view, the probability that a photon with initial energy $\hbar\nu_i$ is inelastically scattered with an energy between $\hbar\nu_s$ and $\hbar(\nu_s + \delta\nu)$ in a solid angle $d\Omega$ is defined by the differential cross section $\frac{d\sigma}{d\Omega d\nu}$, with σ the cross section, which represents the rate of gain/loss of energy by the system:

$$\begin{aligned} \frac{d\sigma^2}{d\Omega d\nu} &= \left(\frac{\nu_i}{\nu_s}\right) \frac{V}{LI_i} \frac{d^2 I_S}{d\Omega d\nu_s} \\ &= \frac{V\nu_i\nu_s^3}{(4\pi)^2 c^4} \underbrace{|\mathbf{e}_s^* \cdot \overbrace{\frac{\partial \chi}{\partial \mathbf{Q}}}}_{\text{Raman vertex}} \cdot \mathbf{e}_i|^2}_{\text{Raman tensor}} \underbrace{\langle \hat{Q}(q)\hat{Q}^*(q) \rangle_\nu}_{\text{Excitations fluctuations}} \end{aligned} \quad (4.5)$$

where χ is now the Raman susceptibility. The Raman vertex, also defined as $\gamma_{\mathbf{k}}(\mathbf{e}_i^*, \mathbf{e}_s) = \mathbf{e}_s^* \cdot \tilde{\gamma}_{\mathbf{k}} \cdot \mathbf{e}_i$, with $\tilde{\gamma}_{\mathbf{k}} = \frac{\partial \chi}{\partial \mathbf{Q}}$ the Raman tensor, acts as a filter which depends on the polarisation of the initial and the scattered photon as well as the "Q" fluctuation and leads to the Raman selection rules described in the next section. Therefore the Raman signal is proportional to the square of the Raman vertex, $I(\mathbf{e}_i, \mathbf{e}_s) \propto |\mathbf{e}_s^* \tilde{\gamma}_{\mathbf{k}} \mathbf{e}_i|^2$. More details can be found in references [210] and [211].

4.2.2 Raman selection rules

We have seen that a fluctuation Q is Raman active and therefore participates in the Stokes and anti-Stokes signal when it modifies the polarizability α , i.e. $\frac{\partial \alpha}{\partial Q} \neq 0$. We have also seen in the Section 3.2.4 that a mode can be dipole active if it changes the electric moment of the molecule, i.e. $\frac{\partial \mu}{\partial Q} \neq 0$. To visualize the phenomena, different phonon modes are presented in figure 4.2. Two cases have to be treated. If the molecule is centrosymmetric (has a center of inversion), there is a condition, called mutual exclusion, which avoids this double excitation (Raman and dipole active). The atoms (red circles) can either oscillate symmetrically with respect to the center of symmetry (blue atom) which leads to a change in the polarizability but no change in the dipole moment (the mode is Raman active but IR inactive) as shown in figure 4.2a, or the atoms can oscillate antisymmetrically and change the dipole moment but not the polarizability (dipole active but Raman inactive) as shown in figure 4.2b. If the molecule is not centrosymmetric, this property vanishes and the polarizability as well as the dipole moment of the molecule change for the phonons "Q" as shown for the two examples in Fig. 4.2c and d. The modes are therefore simultaneously dipole and Raman active.

From the quantum point of view, the Raman intensity is proportional to the square of the Raman vertex ($I(\mathbf{e}_i, \mathbf{e}_s) \propto |\mathbf{e}_s^* \tilde{\gamma}_{\mathbf{k}} \mathbf{e}_i|^2$), which implies that

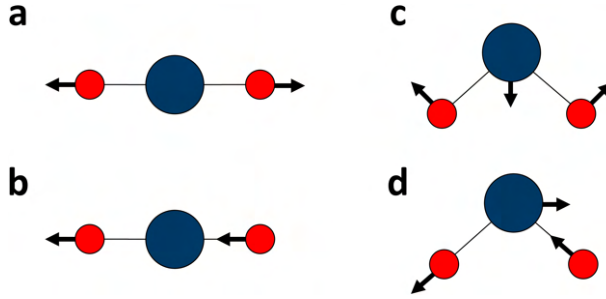


Figure 4.2: Illustration of different normal modes Q for a molecule AB_2 . **a** Raman active mode of a centrosymmetric molecule. **b** Dipole active mode of a centrosymmetric molecule. **c,d** Non centrosymmetric molecule with two different modes that are simultaneously Raman and dipole active.

depending on the initial and scattering photon polarization, some modes are visible and others not. Indeed, the Raman tensor $\tilde{\gamma}_{\mathbf{k}}$ can be decomposed to an irreducible representation of the point group. For example, the orthorhombic metallic phase of nickelates gives rise to 24 Raman active modes whose the irreducible representation [207] is:

$$\tilde{\gamma}_{Pbmn} = 7\tilde{\gamma}_{A_{1g}} \oplus 7\tilde{\gamma}_{B_{1g}} \oplus 5\tilde{\gamma}_{B_{2g}} \oplus 5\tilde{\gamma}_{B_{3g}} \quad (4.6)$$

While the insulating phase presents also 24 modes, they are arranged as:

$$\tilde{\gamma}_{P21/n} = 12\tilde{\gamma}_{A_g} \oplus 12\tilde{\gamma}_{B_g} \quad (4.7)$$

The possible modes that can be probed are shown in the next section.

4.2.3 Geometry of incoming and outgoing light

The Raman experiment uses monochromatic light generated by a laser and the beam is therefore naturally polarized. The direction of polarization depends on the configuration of the laser but can be rotated using a half waveplate. It is therefore possible to align the polarization of the beam parallel or perpendicular to an axis of the measured crystal. We set the z axis along the propagation direction of the laser beam, while the x and y axis are parallel to the crystal as shown in figure 4.3.

An analyzer can be used to select the polarization of the scattered light and thus help to deduce the nature of the vibrational modes. In our experiment, we used the backscattered light configuration, which means that the wave vector of the initial and scattered beam are antiparallel ($\mathbf{k}_i = -\mathbf{k}_s$). Considering that the initial polarization is along the x axis, it is therefore possible to put the crystal parallel to x or perpendicular to x (along y) to

4. Raman spectroscopic evidence for multiferroicity in rare earth nickelate single crystals

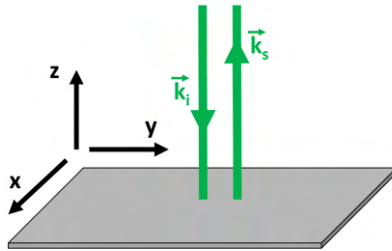


Figure 4.3: Illustration of the geometry of incoming and outgoing light.

excite different vibrations. After scattering, the polarization can be along x or y axis depending on the excited vibration. The analyzer can be rotated in both configurations to detect them individually. The used notation is: $Z(YX)Z$. The first and last letter correspond respectively to the direction of incoming and scattered light respectively (Z in our experiment). The first letter in brackets corresponds to the direction of polarization of the incoming light and the second letter corresponds to the direction of polarization of the scattered light. The following table resumes the nature of the mode as a function of these parameters:

Geometry	Mode nature
$Z(XX)Z$	A_g
$Z(XY)Z$	B_g
$Z(YX)Z$	B_g
$Z(YY)Z$	A_g

Table 4.1: Nature of the probed Raman active modes using backscattered light configuration as a function of the incoming and outgoing polarizations.

4.2.4 Raman experimental setup

Raman spectra were recorded using a Horiba LabRAM HR Evolution spectrometer, whose setup is schematically illustrated in figure 4.4 and permits measurements down to very low wavenumbers ($\sim 10 \text{ cm}^{-1}$), with a resolution of 0.5 cm^{-1} over the full spectral range. The principle is as follows: The light source is a high-power Nd-YAG (neodymium-doped yttrium aluminium garnet) laser that generates a spatially and temporally coherent monochromatic light with a wavelength of 532 nm. The light passes through a power filter which can select nine different intensities and then passes through a beam expander. The beam is sent to a Notch filter, which reflects

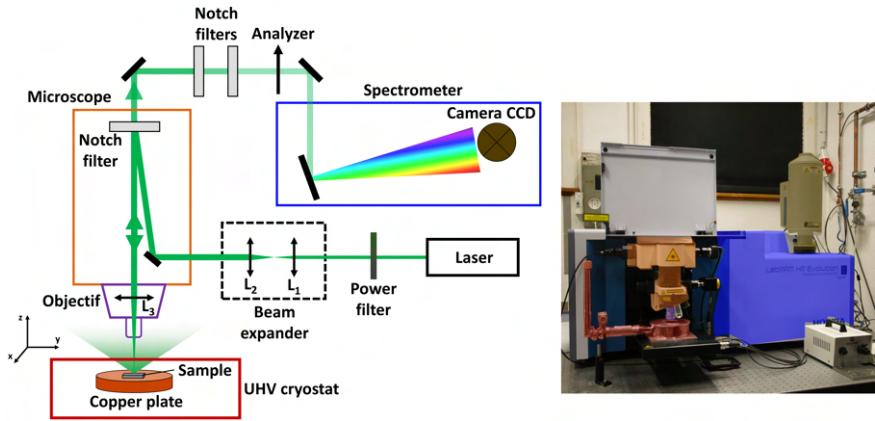


Figure 4.4: Schematic illustration of the Raman measurement setup.

only the laser frequency (532nm), but transmits all other wavelengths. In this first step, the beam is focused on the sample to a $2\ \mu\text{m}$ spot using a window corrected 63x objective. The window is a borosilicate glass with anti-reflective coating efficient between 400 and 800 nm. The micro-crystals were glued on the copper plate of the He flow cryostat (Konti Micro from CryoVac GMBH) using high vacuum grease. Size, shape and orientation of the incident polarisation (parallel to the horizontal axis) varied from one sample to another because the small size of the crystals prohibited a reproducible alignment and concomitant polarisation analysis of the Raman spectra. The light is scattered by the sample (Rayleigh, Stokes and anti-Stokes) and after collection returns to the Notch filter which transmits only light with frequency different than 532 nm (the measurement is therefore done in the darkness to avoid light pollution). Theoretically the filtering efficiency is close to 100% but a small fraction of Rayleigh signal passes through so that two supplemental Notch filter are used to minimize the contribution of Rayleigh scattering. An analyzer can be used to differentiate the polarization of the light and therefore the nature of the vibrations as explained in the section 4.2.2. Finally, the scattered light is diffracted by a grating inside the spectrometer to decompose the different frequencies which are finally detected by a nitrogen cooled charge-coupled device (CCD) camera. Spectra were measured in a broad temperature range from 10 K to 2178 K.

4.2.5 Data analysis and methods for controlling and determining the temperature of the sample

In the high vacuum cryostat, the cold finger is in thermal contact with the copper plate on which the sample is mounted. As other optical setups available in our laboratory, the cryostat allows the temperature of the sample to be lowered down to 10 K and to be stabilized between 10 and 300 K for measurements. A well known problem with Raman spectroscopy is the heating of the sample by the laser. Indeed, the high power necessary to induce detectable Raman scattering often increase the temperature of absorbing samples. However, we can take advantage of this and the modulation of the laser power can be used to achieve temperatures as high as the melting point of the material. Typically, the sample temperature is measured by the thermistor temperature sensor installed on the sample holder. However, as the sample is heated locally during the measurement by the laser, the real sample temperature is set by the equilibrium between the laser heating and the heat exchange between the sample and the sample holder. Due to differences in, amongst other, absorption coefficient, size, shape and the contact between grease layer, crystal and copper, the thermal coupling of the crystals to the cold plate varies from one specimen to another. For this reason, the same incident laser power can heat up different crystals to different temperatures, which will diverge from the temperature measured by the thermistor. To work around this problem, the temperature of the sample is directly extracted from the Raman spectrum from the Stokes/anti-Stokes ratio. The Raman spectrum intensity at finite temperatures is given by:

$$I(\omega, T) = \frac{\text{Im}\chi(\omega)}{1 - e^{-\hbar\omega/k_B T}} \quad (4.8)$$

where $\omega = \omega_i - \omega_s$ is the Raman frequency shift, ω_i (ω_s) is the frequency of the incoming (scattered) photon, T is the temperature, k_B the Boltzmann constant and $\chi(\omega)$ the Raman susceptibility. The imaginary (real) part of $\chi(\omega)$ is an odd (even) function of ω . Since the denominator of Eq. 4.8 changes sign at the origin of ω , the function $I(\omega, T)$ is positive for positive and negative ω . Positive (negative) frequencies represent the Stokes (anti-Stokes) side of the spectrum. Since the Stokes/anti-Stokes ratio

$$\frac{I(\omega, T)}{I(-\omega, T)} = e^{\hbar\omega/k_B T} \quad (4.9)$$

is a universal function of ω/T , the temperature can in principle be readily obtained from this ratio. In practice one first needs to correct the spectra for the wings of the zero-loss peak and for a dark current background. In addition it is necessary to correct for spectrometer spectral response and for the drift of the zero of the frequency axis. Since Eq. 4.9 can only be applied

after these corrections have been made, we use a different approach, which consists of fitting [169] the spectra for positive and negative Raman shifts to a sum of oscillators $\chi_j(\omega)$ for which we use :

$$\chi(\omega) = \sum_j \frac{\omega^2 f_j}{\omega_j^2 - \omega(\omega + i\gamma_j)} \quad (4.10)$$

where f_j parametrizes the amplitude of the j 'th Raman mode, ω_j its peak frequency, and γ_j its half width at half maximum. For all samples the spectra at different temperatures could be satisfactorily modeled with a Lorentzian line shape of the oscillators. The temperature of the sample is used as fitting parameter together with the parameters ω_j , γ_j and f_j of the oscillators. Additional adjustable parameters were the zero of the frequency axis, a frequency independent background, and a symmetric profile for the zero-frequency peak. We excluded the frequency range $-50 \text{ cm}^{-1} < \omega < 50 \text{ cm}^{-1}$ from the fitting procedure for all crystals except NdNiO_3 for which the excluded range was $-20 \text{ cm}^{-1} < \omega < 20 \text{ cm}^{-1}$. Crucially, the Stokes and anti-Stokes side of the spectrum are acquired simultaneously and the spectrum for $\omega < 0$ and $\omega > 0$ is fitted with a single set of parameters. Figure 4.5 shows the example of the fitting procedure of DyNiO_3 where the sample holder is kept at 20 K while the relative intensity of the Raman peaks shown in the inset reveals through fitting that the temperature at the location of the laser beam is in fact 64 K. The spectrum also reveals a continuum of excitations (green) which is most likely of electronic origin.

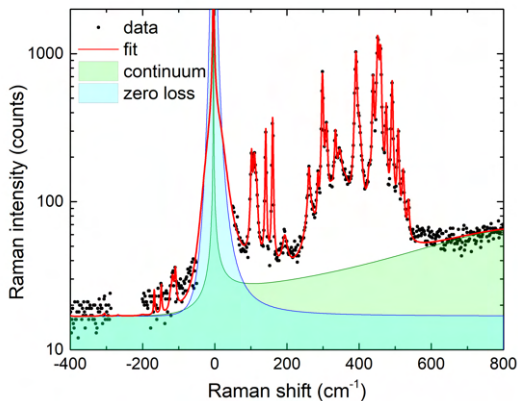


Figure 4.5: Illustration of the different contributions to a Raman spectrum. Raman spectrum of DyNiO_3 shown together with multi-oscillator fit obtained by adjusting the temperature, the oscillators parameters of Eq. 4.10, a background and the zero frequency.

4. Raman spectroscopic evidence for multiferroicity in rare earth nickelate single crystals

As the laser power had to be varied in order to tune the sample temperature, it was necessary to normalize the spectra by the average intensity of the Stokes response extracted between 250 and 550 cm^{-1} .

4.2.6 Sample preparation

The RNiO_3 single crystals with $R = \text{Nd, Sm, Dy, Ho, Er, Y}$ used in this study were grown under high oxygen gas pressure ($p_{max} = 2000$ bar) using a novel synthesis route described in Ref. [209]. The size of the crystals varies from one rare earth to another from 1 to 100 μm . Images of some of the single crystals mounted in the cryostat are displayed in figure 4.6. Their crystal structure and physical properties were characterized using a

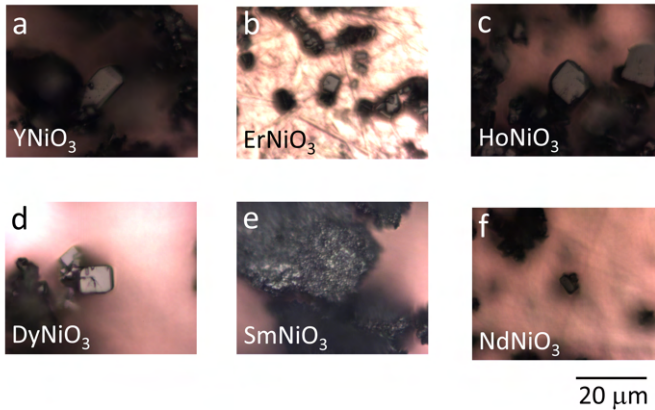


Figure 4.6: Images of a, YNiO_3 , b, ErNiO_3 , c, HoNiO_3 , d, DyNiO_3 , e, SmNiO_3 and f, NdNiO_3 single crystals inside the cryostat of the Raman spectrometer.

broad palette of techniques (powder and single crystal X-ray diffraction, neutron diffraction, EDX, SEM, DSC, magnetization, and heat capacity). The chemical composition, lattice parameters, atomic positions, T_{MI} and T_N obtained from these techniques were in excellent agreement with the values previously reported in the literature for ceramic samples of the same composition (see Ref.[209]).

4.3 Results for the paramagnetic phase

Examples of spectra of all measured nickelates are presented in figure 4.7, at low temperature (in the antiferromagnetic insulating phase) as well as high temperature (in the paramagnetic metallic phase).

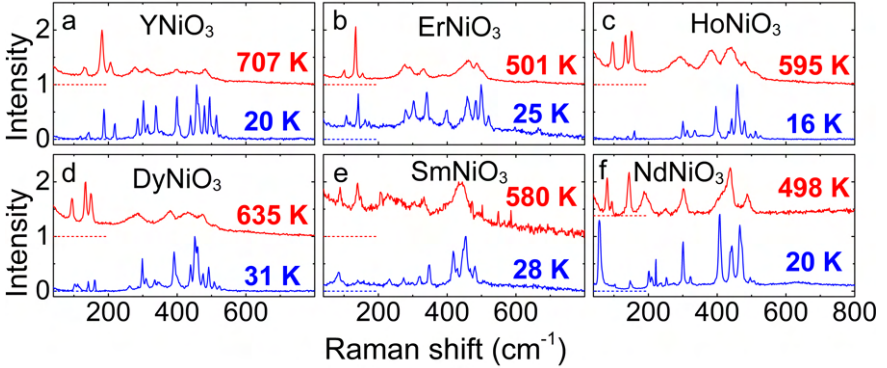


Figure 4.7: Raman spectra in the high temperature metallic state (red curve) and in the low temperature antiferromagnetic state (blue curve) of **a**, YNiO_3 , **b**, ErNiO_3 , **c**, HoNiO_3 , **d**, DyNiO_3 , **e**, SmNiO_3 and **f**, NdNiO_3 .

The full dataset covering the entire temperature range is shown in Fig. 4.8 as colorplots of the Raman response in the frequency-temperature plane. Figure 4.9 shows the evolution with temperature across the different structural and electronic phases of the main phonons for the six compounds. We begin with an observation on the character of the Raman modes. In the metallic and insulating phases the crystal point group has, at least down to T_N , inversion symmetry. Consequently the optical modes are either Raman active (even parity) or dipole active (odd parity). The $Pbnm$ (metallic phase at high temperature) and the $P2_1/n$ (insulating phase at low temperature) space groups contain four formula units, and therefore have 60 vibrational degrees of freedom corresponding to 3 acoustic modes, 33 odd parity modes observable in the optical conductivity and 24 even parity modes that are Raman-active. Another important feature shared by the $P2_1/n$ and $Pbnm$ phases is that the four Ni atoms seat on inversion centers. Consequently only the motions of oxygens and rare earth atoms contribute to the Raman spectrum.

In the metallic state, modes are very broad as they are superposition of several phonons close in energy (we know it is the case for octahedra modes in NdNiO_3 [212]) further broadened by the electron-phonon interaction. Cooling down to the paramagnetic insulating state, the transition results in a significant blueshift of all modes and both Fig. 4.8 and Fig. 4.9 tend

4. Raman spectroscopic evidence for multiferroicity in rare earth nickelate single crystals

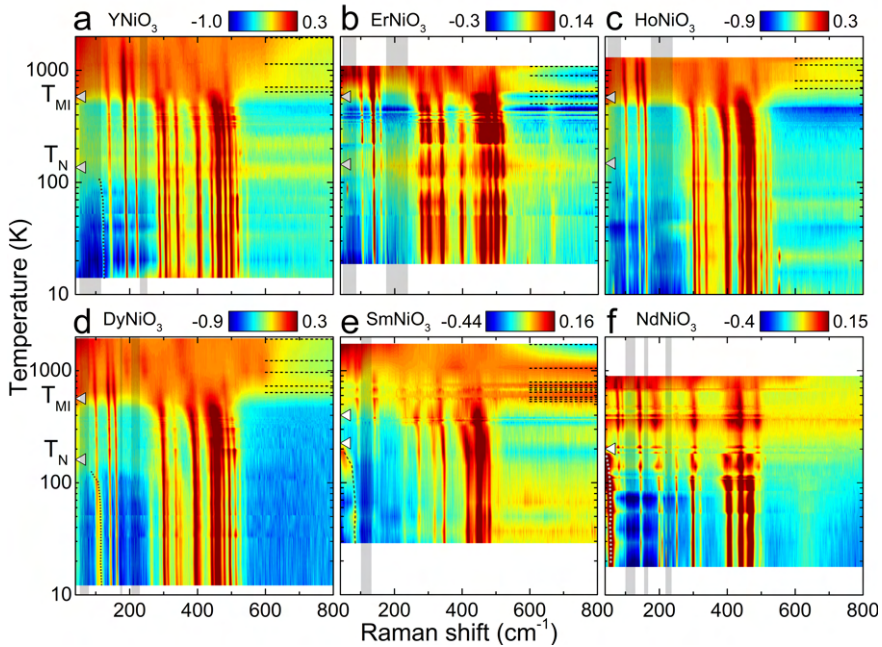


Figure 4.8: Colorplots of Raman intensity a, YNiO_3 , b, ErNiO_3 , c, HoNiO_3 , d, DyNiO_3 , e, SmNiO_3 and f, NdNiO_3 samples. The horizontal axis shows the Raman shift in cm^{-1} , the vertical axis the temperature in K on a log scale, and the color represents the intensity of the signal in a logarithmic scale. White triangles indicate the temperatures of metal to insulator transition (high temperature) and the magnetic ordering (low temperature). When present, the soft-mode frequency from the spectral fit is marked with a dashed gray line. Gray regions are averaging windows used for the temperature dependence of the Raman electronic background. Dotted horizontal lines indicate the temperatures of the spectra above 700 K used for the color plot. The temperature mesh below 700 K is too dense to indicate this way.

to indicate a massive increase of modes number as the systems become insulating. Cooling through T_{MI} the four NiO_6 octahedra within the primitive cell bifurcate into one set with short Ni-O bonds and a second set with long bonds which might cause a lift of degeneracy. However, the number of Raman active modes (24) is not affected by the symmetry breaking and we may reasonably expect that intensity and frequency of these modes change at the transition due, inter alia, to the vanishing of electron-phonon coupling. The overall trend of the mode frequencies as a function of rare earth element (Fig. 4.9) is a blueshift of all frequencies when moving from Nd to Y element. This trend is most pronounced for the three main modes below 230 cm^{-1} , where in particular the case of YNiO_3 stands out in that the three main modes have frequencies approximately 35-40 % higher than for HoNiO_3 ,

4.3 Results for the paramagnetic phase

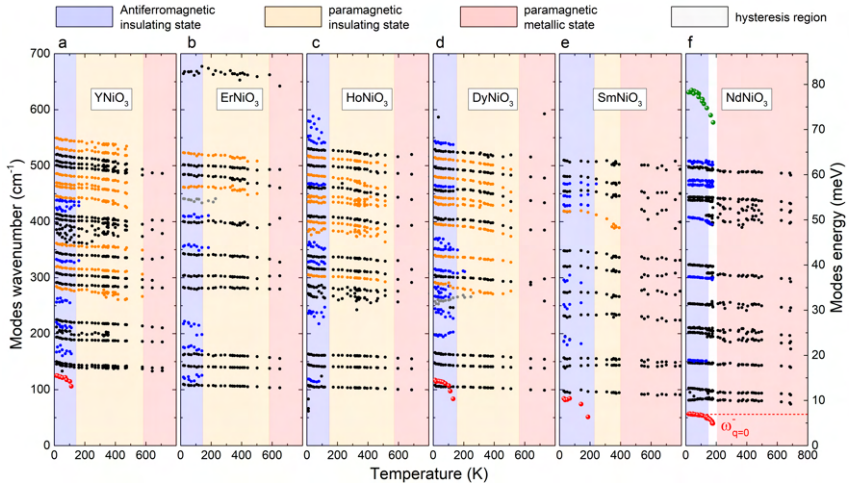


Figure 4.9: Evolution with temperature of the frequency of the Raman modes. Black symbols: Modes already present above T_{MI} . Orange symbols: Additional modes below T_{MI} . Blue symbols: Additional modes below T_N . Red symbols: Anti-ferromagnetic resonance. Green symbols (NdNiO_3): Bimagnon bound state.

in agreement with the ratio $(m_{Ho}/m_Y)^{0.5} = 1.36$ expected for vibrations with a rare earth character mainly. The modes above 500 cm^{-1} shift up by approximately 10 % from Nd to Y, revealing a hardening of the chemical bond, a trend that is expected in view of the reduction of the lattice constant for the smaller rare earth elements. A weak feature in ErNiO_3 at 670 cm^{-1} , not seen in any of the other samples, is possibly due to impurities or to an Er $4f$ crystal field excitation.

High energy peaks between 250 cm^{-1} and 650 cm^{-1} are involving stretching or bending of nickel-oxygen bonds that are strongly hybridized in the metallic state. This strong electron-phonon coupling shows up upon warming up from the insulating to the metallic state, as a red-shift and a strong broadening of these modes already 10 K below the metallic state.

The mode visible at 10 K at 420 cm^{-1} and 410 cm^{-1} for SmNiO_3 and NdNiO_3 respectively, seems to strongly soften upon approaching the metal insulator transition. The strong softening of this phonon is consistent with previous report of Raman experiments for $\text{Sm}_x\text{Nd}_{1-x}\text{NiO}_3$ thin films [207]. The absence of this trend for other rare earths might be related to the more second-order like character of the transition. The frequencies of most low energy modes between 100 and 250 cm^{-1} likely associated with the motion of the rare earth or rotation modes of oxygen octahedra are only weakly affected by the transition.

4. Raman spectroscopic evidence for multiferroicity in rare earth nickelate single crystals

The Raman spectra of all samples also show an interesting behavior in the temperature dependence of the electronic continuum. Raman susceptibility $Im\chi(\omega)$ is related to the free carriers optical conductivity $\sigma(\omega)$ as:

$$Im\chi(\omega) \propto \omega Re\sigma(\omega) \quad (4.11)$$

This manifests as a broad contribution, in the metallic phase of all samples, to the electronic background (so-called Raman continuum) superimposed on the vibrational features that is strongly suppressed as the system enters the insulating state (see Fig.4.8.).

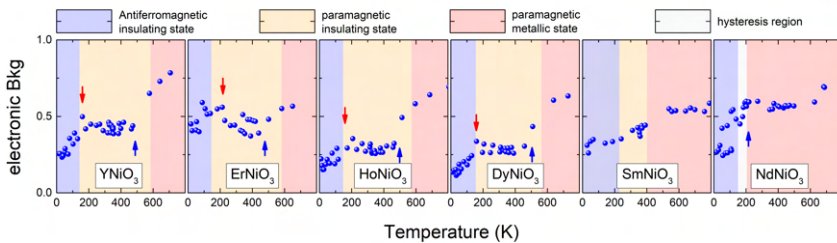


Figure 4.10: Evolution of the electronic background with temperature. Kinks associated with the two transitions are indicated as arrows.

In figure 4.10, we plot the average electronic background as a function of temperature which corresponds to the average value of the Raman intensity of each spectrum in the regions without Raman active modes in between 50 and 250 cm^{-1} . The sharp drop associated with the metal-insulator transition, marked by a blue arrow, often falls below the metal insulator transition reported that matches well the structural transition detected from phonon spectral change for each compound. In addition, conductivity is further reduced when going from the paramagnetic to the antiferromagnetic insulating state (red arrow in Fig. 4.10). This confirms a previous observation that the magnetic ordering reinforces the charge ordering and thus the localisation of free carriers [70].

4.4 Results for the antiferromagnetic phase

NdNiO_3 is special among the samples studied in that the anomalies at the metal-insulator transition are particularly sharp. Here we see for all phonons an abrupt narrowing and an intensity change at T_N ($=T_{MI}$), and the 305 cm^{-1} mode splits into a strong peak at 300 cm^{-1} and a weak one at 315 cm^{-1} , confirming the observations in Refs. [207, 208]. We observe

an additional mode at the low frequency end of the spectrum (58 cm^{-1} at the lowest temperatures), showing a strong redshift upon raising the temperature to T_N . This mode is present for all compounds except ErNiO_3 and HoNiO_3 and its frequency slightly increases for stronger deformation (120 cm^{-1} for Yttrium). Since this is in the range of the zone-center magnon obtained for the same material from extrapolating resonant inelastic x-ray scattering (RIXS) data (13 meV) [161] we interpret this mode as the anti-ferromagnetic resonance. NdNiO_3 is the only compound showing a peak near 640 cm^{-1} with a strong redshift upon raising the temperature to T_N . This is probably a bi-magnon: Taking the experimental value of the energy of the zone-boundary magnon from RIXS [161] we arrive at $2 \times 55 \text{ meV}$ giving 887 cm^{-1} as the upper bound. The lower frequency in the Raman spectrum can be qualitatively understood as a consequence of magnon-magnon coupling.

We will focus now on dysprosium nickelate DyNiO_3 , which reveals the most pronounced features. A DyNiO_3 crystal is shown in Fig. 4.11a and the Raman spectra of DyNiO_3 are shown in Fig. 4.11b for representative temperatures near the melting point (1911 K), in the metallic phase (729 K), deep inside the paramagnetic insulator phase (205 K) and deep inside the magnetically ordered phase (12 K). For DyNiO_3 we have acquired spectra up to 1911 K . At this elevated temperature, which is close to the melting point, few modes can still be detected separately and will be discussed in section 4.6. Cooling to 729 K (about 200 K above T_{MI}) blueshifts and sharpens these features, so that 7 narrow peaks and 4 broader ones can be distinguished, which is below the expected 24 Raman active phonons of the $Pbnm$ structure, presumably due to a small Raman cross section and overlap of some modes. Cooling the samples through the magnetic phase transition has a surprisingly large impact on the Raman spectra. As is illustrated in Fig. 4.11b, we observe below T_N at least 5 relatively strong additional modes at $120, 270, 310, 350, 460 \text{ cm}^{-1}$ and 2 weaker ones at 200 and 540 cm^{-1} . The total number of modes in the low temperature Raman spectrum is 22 out of 24 that are Raman active, *i.e.* the number of Raman active modes observed in DyNiO_3 does not indicate as such that the space group in the magnetic phase should be different from $P2_1/n$. However, it is remarkable that certain modes appear in pairs. For DyNiO_3 the modes near $305, 340$ and 450 cm^{-1} split into doublets below T_N . We notice this for the 305 cm^{-1} mode of NdNiO_3 and the splitting of the 340 cm^{-1} mode is also clearly seen for HoNiO_3 and ErNiO_3 . A well defined mode appears for DyNiO_3 near 280 cm^{-1} surrounded by two shoulders. The same mode is observable at low temperature for HoNiO_3 with the difference that this narrow peak is still present as a shoulder in the paramagnetic phase. A second well defined characteristic mode appears at around 350 cm^{-1} for

4. Raman spectroscopic evidence for multiferroicity in rare earth nickelate single crystals

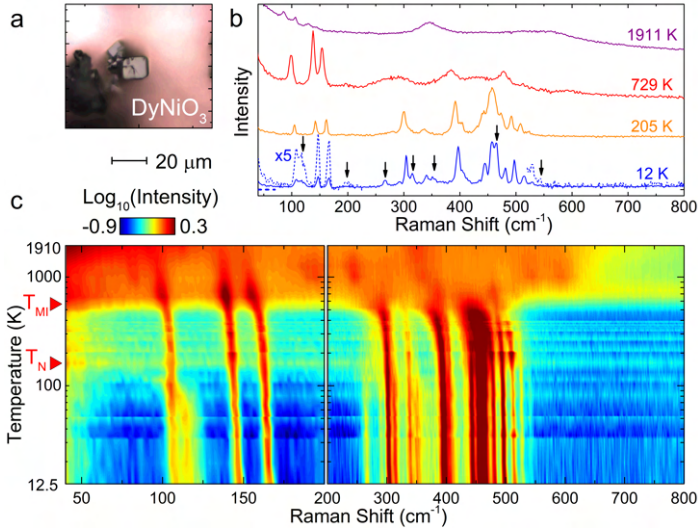


Figure 4.11: **a**, Image of a DyNiO_3 single crystal inside the cryostat. **b**, Typical Raman spectra recorded on DyNiO_3 at temperatures in the antiferromagnetic insulating phase (blue curve, dashed line is a factor 5 magnification of the blue curve), paramagnetic insulating phase (orange curve) and metallic paramagnetic phase (red curve). The purple curve is close to the melting point of the material. The curves have been given vertical offsets to avoid clutter. Raman modes appearing in the antiferromagnetic phase are marked by arrows. **c**, colormap of the Raman response in the full temperature range from 12.5 K to 1911 K. Metal-insulator and magnetic transitions are labeled as red symbols.

DyNiO_3 , which is observable also for HoNiO_3 and ErNiO_3 . We observe also the appearance of a broad mode for DyNiO_3 , YNiO_3 and HoNiO_3 at 250 cm^{-1} (Fig. 4.9). Other new modes emerge at 550 and 570 cm^{-1} for HoNiO_3 , at 200 and 550 cm^{-1} for DyNiO_3 and at 440 cm^{-1} for ErNiO_3 .

For the interpretation of the additional modes below T_N the case of YNiO_3 is of particular importance. Taking a close look at the Raman spectra in the paramagnetic and antiferromagnetic insulating phase shown in Fig. 4.12a and b respectively, we notice that (i) there are 24 Raman modes above T_N and (ii) this number increases to 31 below T_N . One of the extra modes (the one at 120 cm^{-1}) is the antiferromagnetic resonance. Since Y has no $4f$ electrons, we can exclude beyond any doubt contributions of $4f$ crystal field excitations to the Raman spectra. The only remaining interpretation of the additional modes is therefore that these are phonons. Since for $P2_1/n$ the number of Raman active phonons is limited to 24, observing 30 Raman active phonons is a clear demonstration that the space

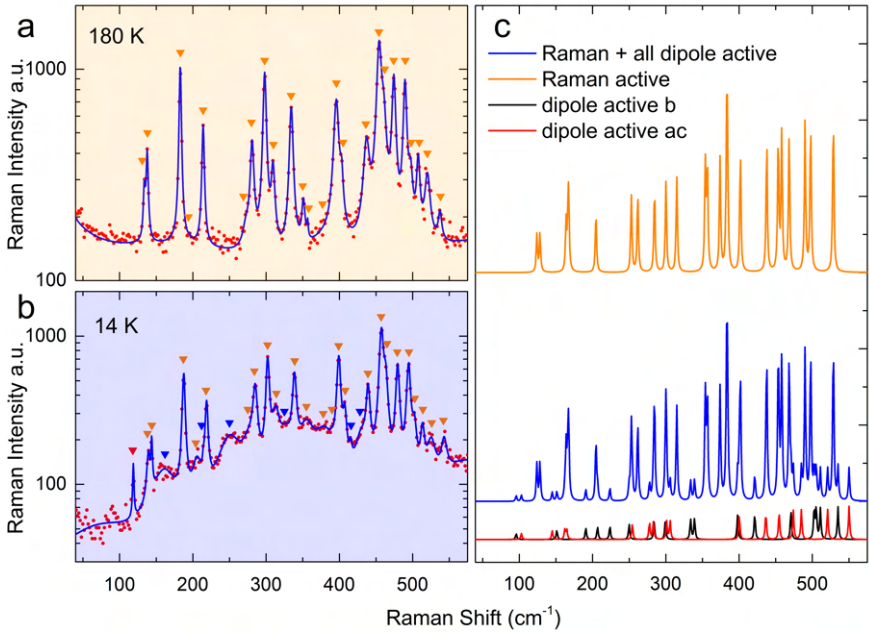


Figure 4.12: Raman spectra of a YNiO_3 single crystal **a**, in the paramagnetic insulating phase (180 K) and **b**, in the antiferromagnetic insulating phase (14 K). Orange triangles: Raman modes of the paramagnetic phase. Blue triangles: Additional modes in the magnetic phase. Red: anti-ferromagnetic resonance. **c**, simulated Raman spectrum of YNiO_3 in the paramagnetic insulating phase (orange) and the insulating antiferromagnetic phase (blue) where it is assumed that all dipole active phonons (b -axis: black, ac -plane: red) have become Raman active as a result of inversion symmetry breaking. The modes have a Lorentz line-shape with a full-width at half-maximum of 4 cm^{-1} . The intensities of the Raman modes were all given the same value, and the intensities of all polar modes $1/5$ th of those of the Raman modes.

group in the antiferromagnetic phase must be different from $P2_1/n$. Some of the peaks, *e.g.* the additional mode around 270 cm^{-1} in DyNiO_3 in Fig. 4.11(b), are already present above T_N . This is possibly the consequence of short range antiferromagnetic order that is still present above T_N . This interpretation is consistent with the disappearance of intensity within a range of 20 K as the temperature is increased above T_N .

To compare, we calculated Raman and dipole active phonon frequencies of YNiO_3 (Fig. 4.12c) using Density-Functional Perturbation Theory as implemented in Quantum Espresso [213]. The monoclinic unit cell was relaxed and an all electrons self consistent calculation was used with a generalized gradient approximation within the Perdew-Burke-Ernzerhof functional [214]. Cut-off energies for kinetic energy and charge density

4. Raman spectroscopic evidence for multiferroicity in rare earth nickelate single crystals

were 100 Ry and 600 Ry respectively. The k -points corresponding to the electronic wave functions were integrated on a $7 \times 6 \times 5$ Monkhorst-Pack grid yielding 72 k -points in the irreducible wedge of the Brillouin zone. Dynamical matrices were then computed using a self consistent convergence criterion of 10^{-12} Ry. Polarized neutron diffraction experiments have proven the magnetic origin of the aforementioned $(1/2, 0, 1/2)$ superlattice [43, 154, 215]. Consequently the magnetic order modulates the force constants with the same lattice periodicity as the one of the paramagnetic state, thus excluding the possibility that the additional modes are folded zone-boundary phonons. If on the other hand a breaking of inversion symmetry were to occur, this would have a major impact on the Raman spectra. The implication for the vibrational modes is that all dipole active modes become simultaneously Raman active and vice versa. For non-polarized Raman as used for the spectra in Fig. 4.12 at most 33 polar modes will then contribute to the Raman spectra below T_N . The *ab initio* calculations of the vibrational spectrum presented in Fig. 4.12c demonstrate that the features in the experimental data of Fig. 4.12b are indeed consistent with polar modes that become Raman active below T_N . Some of the additional modes below T_N show up as shoulders of peaks already present in the paramagnetic insulating phase. The fact that some of these modes appear as pairs and others not, is then a simple consequence of the fact that some of the Raman and polar modes correspond to similar vibrational patterns, the main difference being the in-phase and out-of-phase motion of subsets of the atoms (in the present case four formula units) inside the primitive cell. The fact that 30 vibrational modes at low temperature are observed for YNiO_3 , which is 6 more than allowed by the factor group analysis, implicates that the antiferromagnetic phase is polar.

4.5 Discussion

It is fully established that the magnetic order of these compounds is described by the propagation vector $(1/2, 0, 1/2)$ (or $(1/4, 1/4, 1/4)$ when referred to the underlying pseudocubic lattice), but the orientation of the magnetic moments is less clear [154, 155, 159–161, 215]. Giovannetti *et al.* [48] discuss three types of magnetic order labeled T , S and N . For T -type order, the magnetic moments are arranged in planes of parallel spins alternating as $\uparrow\uparrow\downarrow\downarrow$ along the $[1, 1, 1]$ direction of the underlying pseudocubic structure, which they predict to be polar with electric dipole components along a and c . For S -type, they predict a net electric dipole along b . The predicted multiferroicity for T and S originates in the phenomenon that theoretically regions between parallel (opposite) magnetic moments become electron poor (rich) due to exchange-correlation as it was illustrated in figure 2.17 in the section 2.4. The non-

collinear magnetic structure N owes its multiferroicity to spin-orbit coupling, and has an electric dipolar moment oriented in the ac plane but much weaker than the collinear T and S arrangements [48]. For S and N-type magnetic order, the space group is $P_{2a}2_1$ according to the symmetry operations, while for T-type magnetic order the space group is $P_{2a}c$ as it was demonstrated in the section 2.4. Perez-Mato *et al.* predicted the existence of magnetism-induced ferroelectricity from group theory arguments based in the symmetry of the paramagnetic space group and the magnetic propagation vector [51]. According to these arguments a symmetry decrease from centrosymmetric P_{21}/n to polar $P_{2a}2_1$ and the appearance of spontaneous polarization along the b crystal axis are expected to occur below T_N for the collinear and non-collinear magnetic structures reported respectively for PrNiO_3 [215] and HoNiO_3 [154]. In any of these scenarios the electric fields induced by the electronic charge displacements will act as a force on the ions, deforming the lattice and pushing the Ni-ions away from centrosymmetric positions. The modes that involve displacements of the Ni atoms along b are schematically shown in Fig. 4.13 together with their impact on the optical selection rules.

Moving from Nd to Y, the number of additional modes that we can detect below T_N increases. That the multiferroic effect is strongest for the smaller rare earth ions has in fact been anticipated by Giovannetti *et al.* [48]. The ingredients responsible for the multi-ferroic effects are magnetic order, breathing distortion and rotation of the oxygen octahedra (Fig. 2.17 section 2.4). This combination of factors is uncommon in the multiferroic family tree [202] and characteristic for the rare earth nickelates. Of the samples studied here YNiO_3 has the smallest tolerance factor (Table 2.1 in the section 2.2.1) and consequently the largest octahedral rotation, highest T_{MI} and the strongest breathing distortion. While the moderate decrease of T_N from NdNiO_3 to YNiO_3 suggests a weakening of the magnetic order parameter, this is more than compensated by the increasing octahedral rotation and breathing distortion, together resulting in the observed positive trend of the multiferroic coupling from large to small tolerance factor.

For PrNiO_3 , Gawryluk *et al.* analyzed the temperature dependence of the crystal structure in terms of symmetry adapted modes [216]. The unconventional temperature dependence of the lattice parameters below $T_{MI} = T_N$, and the observation of a nearly perfect linear correlation between the breathing mode amplitude and the staggered magnetization, lead to the conjecture of a hidden order in the insulating phase, in particular the predicted polar distortion induced by the noncentrosymmetric magnetic order discussed by Giovannetti *et al.* and Perez-Mato *et al.* [48, 51]. The clear lattice anomalies recently observed at T_N for EuNiO_3 [209] confirm this intuition, giving additional support to the Raman findings.

4. Raman spectroscopic evidence for multiferroicity in rare earth nickelate single crystals

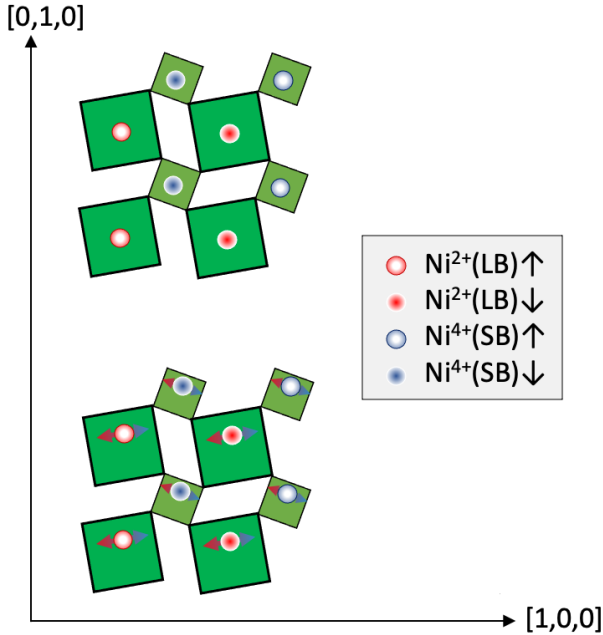


Figure 4.13: Scheme of the spontaneous inversion symmetry breaking. Labels for up/down spin and long/short-bond Ni are indicated at the right hand side. To avoid clutter oxygen atoms (at the corners of the squares) and rare earth atoms (in the open spaces) are not indicated. Top: The Ni ions occupy inversion symmetric positions. Bottom: The electric fields induced by the T-type or S-type antiferromagnetic order (see Fig. ??) push the Ni ions to low symmetry positions, which has two main effects: (i) It contributes a net electric dipole moment. (ii) Since these positions lack inversion symmetry, modes of any polarization are simultaneously Raman active and dipole active. Vibrations around the rest-position are symbolized by double-headed arrows.

4.6 Raman measurement at very high temperature or under high pressure

In the previous section, we saw that the metal-insulator and the magnetic transitions are driven or accompanied by structural transitions. For this last section, we are interested in the effect of high pressure and very high temperature on these single crystals. To start with the latter, figure 4.14 shows, for each crystal, four Raman spectra above the metal insulator transition. The spectra with the highest temperature we could reach for each sample is shown in blue.

The peak at 450 cm^{-1} present in the insulating phase of all compounds disappears gradually above the metal-insulator transition temperature. A

4.6 Raman measurement at very high temperature or under high pressure

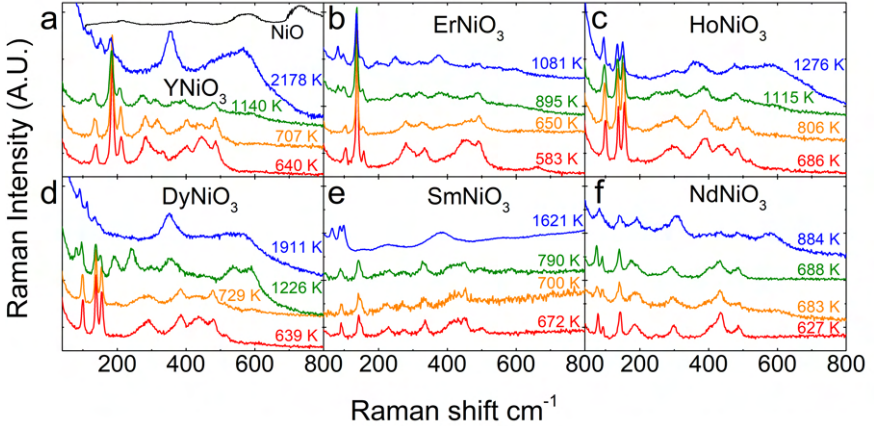


Figure 4.14: Raman spectra of rare earth nickelates single crystals at high temperature above the metal-insulator transition. **a**, YNiO_3 . NiO from reference [217]. **b**, ErNiO_3 . **c**, HoNiO_3 . **d**, DyNiO_3 . **e**, SmNiO_3 . **f**, NdNiO_3 .

small peak appears below 100 cm^{-1} for YNiO_3 , ErNiO_3 , DyNiO_3 and SmNiO_3 for temperature above 730 K. For the highest temperatures of all the samples except ErNiO_3 and NdNiO_3 (temperature may perhaps not be high enough), we observe a reduction of the number of phonons and the appearance of two bands around 400 and 600 cm^{-1} . At high temperature, we expect an orthorhombic to rhombohedral structural transition as it is the case at 770 K for PrNiO_3 [115]. However, it is also known that RNiO_3 decomposes to NiO and RE-O at high temperature, especially for smaller rare earth elements that are thermodynamically less stable.

By comparing the Raman spectrum of NiO (Fig. 4.14a) and of R_2O_3 ($\text{R}=\text{Y, Er, Ho, Dy, Sm}$) presented in figure 4.15 we can assume that the modes at 400 and 600 cm^{-1} at very high temperature are R_2O_3 and NiO vibrational excitations, respectively. Moreover, the modes related to the rare earths (between 100 and 200 cm^{-1}) are slightly affected by this decomposition. The two pics around 100 cm^{-1} of NdNiO_3 seem to be replaced by a large peak at 884 K. This mode will be discussed in the following and compared with the results of measurements under pressure.

It was reported that the temperature of the metal-insulator transition of nickelates decreases for increasing pressure [92, 103], while several studies show at room temperature a pressure-induced insulator-metal transition for YNiO_3 [102], EuNiO_3 [92, 103, 106] and SmNiO_3 [101, 104, 105] at about 14, 6 and 2.5 GPa, respectively. The decreasing of T_{MI} for NdNiO_3 and PrNiO_3 with increasing pressure was also reported [108, 109] and the total

4. Raman spectroscopic evidence for multiferroicity in rare earth nickelate single crystals

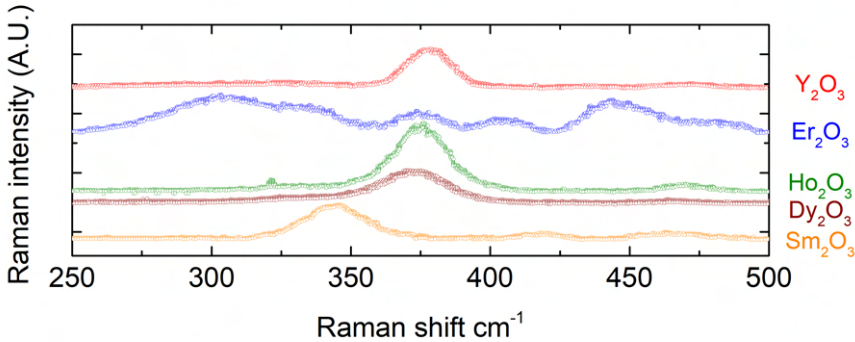


Figure 4.15: Raman spectra of R_2O_3 ($R=Y, Er, Ho, Dy, Sm$) from reference [218].

suppression of the metal-insulator transition ($T_{MI} \rightarrow 0$ K) was observed at ~ 2.6 GPa [91] and 1.3 GPa [107–109], respectively. With increasing pressure, the Ni-O-Ni superexchange angle increases, while the Ni-O bond lengths are contracted. It leads to a broadening of the electronic bandwidths which closes the gap. Note that the structural transition from $P2_1/n$ to $Pbnm$ space groups occur simultaneously. It was also observed for $NdNiO_3$ [112], $PrNiO_3$ [111] and $SmNiO_3$ [105] that pressure induces orthorhombic-rhombohedral phase coexistence followed by a pure rhombohedral $R\bar{3}c$ phase.

To apply pressure on crystals, we used a diamond anvil cell. Two diamond anvils are facing each other as shown in figure 4.16 and a gasket (small metallic discs of copper beryllium) with a borehole forms a chamber sealed by the two anvils. To induce hydrostatic pressure, this chamber is filled by a pressure transmitting media (oil). The measured crystal is bathed in the transmitting media and the pressure can be tuned by the application of helium gas in a stainless steel membrane which brings the two diamonds closer. The diamonds press together and therefore induce strain on the crystal. To measure with precision the pressure inside the chamber, a ruby crystal is used as a pressure gauge and is placed near the sample. Indeed, two characteristic fluorescence peaks of ruby shift to higher frequency for increasing pressure and can be simultaneously measured with the Raman spectrum. The frequency of the second peak allows to deduce the pressure in the chamber. In the framework of the measurement, the Raman beam passes through the diamond before impinging on the samples. A complete description of the pressure measurement with diamond anvil cell can be found in reference [219]. Our measurements were performed at room temperature.

4.6 Raman measurement at very high temperature or under high pressure

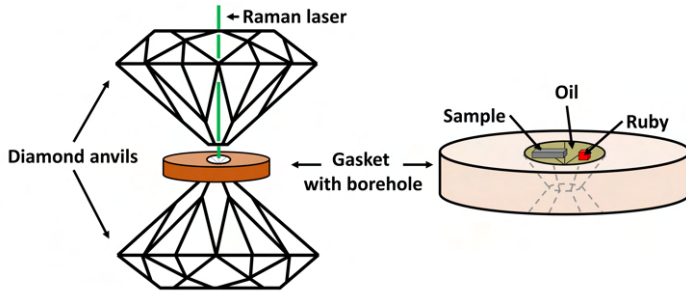


Figure 4.16: Illustration of the diamond anvil cell. The two diamonds face each other and press together. Between them, a gasket with a borehole creates a chamber in which the crystal of interest and a ruby crystal are placed. To apply hydrostatic pressure, the chamber is filled with pressure transmitting media (oil).

We measured a single crystal of SmNiO_3 (which is insulating at ambient temperature and pressure condition) between 30 and 550 cm^{-1} up to 16.9 GPa. The spectra are presented in figure 4.17a. The oil used as a pressure transmitting medium slightly contributes to the Raman response with the presence of two broad bands at 225 and 300 cm^{-1} (indicated by the stars) and add a significant background at low frequency (below 200 cm^{-1}) that was removed in the Fig. 4.17. The oil contribution disappears as pressure increases as the sample get pressed against the diamond and almost disappears around 1 GPa. The Raman response at 0.1 GPa is similar to the spectrum at 360K (0 GPa) presented in the last section. We had to use high power of the laser to induce detectable Raman scattering which heats up the sample about 350 K. The spectra does not evolve much up to 1 GPa. Between 1 GPa and 2.4 GPa, several noticeable changes occur in the spectrum. The mode at 450 cm^{-1} splits into two peaks, one at 430 cm^{-1} and the other at 460 cm^{-1} , while the mode at 300 cm^{-1} and 400 cm^{-1} have totally disappeared. These three features are characteristic of the temperature-induced insulator-metal transition observed in the last section at ambient pressure and reproduced in figure 4.17b. The Raman response at 530 K (above the transition) and at 300 K at 2.36 GPa is almost equivalent. This pressure-induced metal-insulator transition was already reported around 2.5 GPa in several studies [101, 104, 105]. The transition is accompanied by a transition from the $P2_1/n$ monoclinic to $Pbnm$ orthorhombic structure. We also observe a shift of the modes at 260 and 230 cm^{-1} to ~ 270 and 220 cm^{-1} respectively, while the modes associated to the rare earth are not affected by the transition. The mode at 400 cm^{-1} associated with the distortions of the oxygen octahedra red shifts from T_N to T_{MI} as shown in the evolution with temperature in agreement with Girardot et al. [207]. They explain that it is a signature of the charge disproportionation and the disappearance of this

4. Raman spectroscopic evidence for multiferroicity in rare earth nickelate single crystals

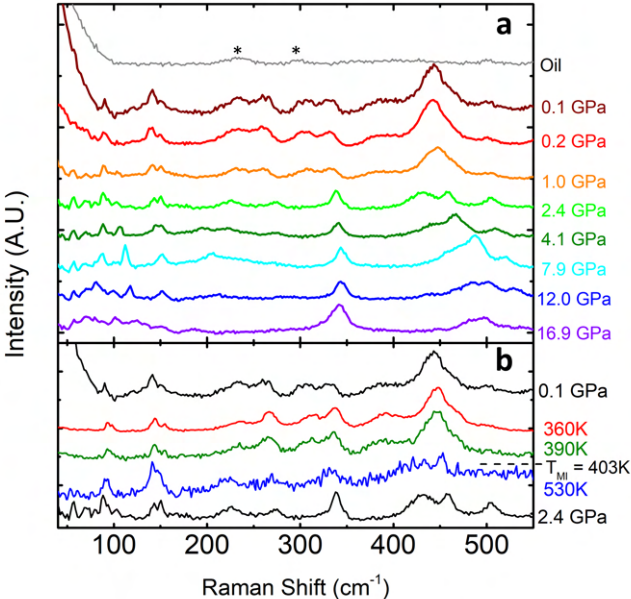


Figure 4.17: **a**, Raman measurement of SmNiO_3 under pressure from 0.08 to 16.9 GPa at room temperature. The intensity of the Raman signal is in arbitrary unit. Huge changes occur in the spectra between 1.0 and 2.4 GPa which is a signature of the metal-insulator transition. **b**, Temperature evolution of the Raman spectra of SmNiO_3 across the metal-insulator transition and comparison with SmNiO_3 under pressure.

mode indicates that the structure recovers equivalent Ni-O bonding (unlike the breathing distortion in the insulating phase) and therefore become metallic. Increasing the pressure up to 16.9 GPa, the two peaks at 430 and 460 cm^{-1} shift to higher frequency (480 and 500 cm^{-1} respectively), while the other peaks, for example the mode at 340 cm^{-1} , remain at the same frequency. The two peaks around 150 cm^{-1} merge into a single broad peak beyond 7.8 GPa. For higher pressure (from 16 to 30 GPa), the system should present an orthorhombic-rhombohedral phase coexistence followed by a pure rhombohedral $R\bar{3}c$ phase as reported by Massa et al. [105]. However, the deformation of the gasket did not allow us to reach such high values.

Figure 4.18a shows the Raman spectra of NdNiO_3 single crystal under pressure from 0 to 21.4 GPa. As for SmNiO_3 , the spectrum at 0 GPa is similar to the Raman response of NdNiO_3 at 340K collected as a function of temperature and are comparable to the spectra reported by Zaghrioui

4.6 Raman measurement at very high temperature or under high pressure

[208]. Two modes at 75 cm^{-1} are present as reported in our temperature measurement but are hidden by the noise. From 0 to 7.1 GPa, the peaks at 150 and 310 cm^{-1} remain nearly at the same frequency, while the peak at 440 shifts to 460 cm^{-1} and its intensity increases relatively to the others. From 7.1 to 8.5 GPa a mode at 90 cm^{-1} , absent at lower pressure, starts to

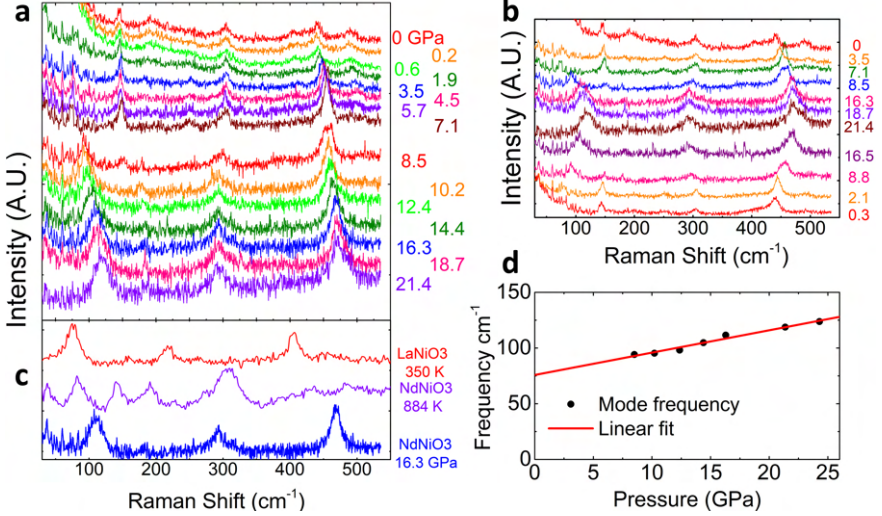


Figure 4.18: **a**, Raman measurement of NdNiO₃ under pressure from 0 to 21.4 GPa at room temperature. **b**, Raman measurement of NdNiO₃ under pressure from 0 to 21.4 GPa, then from 21.4 to 0.3 GPa at room temperature. The transition is completely reversible and no hysteresis is noticeable. **c**, Comparison between Raman spectra of LaNiO₃ at 350 K, NdNiO₃ at 884 K and NdNiO₃ at 16.3 GPa (300K).

appear, while the modes at 150 and 250 cm^{-1} start to vanish. The peak at 460 cm^{-1} does not move any more in frequency (up to 10.2 GPa). There might even be two peaks but the resolution of our data does not allow us to assure this observation. This reveals the coexistence of phases, the orthorhombic and rhombohedral phase described by Medarde [112]. At 10.2 GPa, the peak at 90 cm^{-1} has completely emerged, while the peaks at 150 and 250 cm^{-1} have totally disappeared. From 10.2 to 21.4 GPa, the peak at 310 cm^{-1} still remains at its position, while the peak at 90 and 460 cm^{-1} shift to higher energy (to ~ 120 and 475 cm^{-1} respectively). We performed measurements from 21.4 to 0 GPa and the transition is completely reversible as shown in figure 4.18b. Note that no hysteresis is noticeable. Assuming that at 16.3 GPa NdNiO₃ is completely in a rhombohedral crystal structure, some features should be similar to LaNiO₃ which remains rhombohedral for all temperatures at ambient pressure. Figure 4.18c shows the comparison

4. Raman spectroscopic evidence for multiferroicity in rare earth nickelate single crystals

between LaNiO_3 at 350K (which was measured in the same way than all the other nickelates of the previous section), NdNiO_3 at 16.3 GPa and NdNiO_3 at 884 K presented at the beginning of this section. The peaks at 300 and 475 cm^{-1} in NdNiO_3 were already present in the orthorhombic structure and therefore cannot be associated to a mode of the rhombohedral structure. However, the broad band that appears at 90 cm^{-1} from 7.1 to 8.5 GPa is very close to the mode at 75 cm^{-1} in LaNiO_3 . This large peak is characteristic of LaNiO_3 (present at all temperatures) and does not appear in the other nickelates, which may indicate that it belongs to the rhombohedral structure (note that the LaNiO_3 spectra evolve very slightly from 75 to 380K). A linear fit of the position of this mode for NdNiO_3 as a function of pressure (Fig. 4.18d) shows that at 0 GPa the mode would be at 76 cm^{-1} , which is exactly the position of the peak in LaNiO_3 . Note also that the spectra of LaNiO_3 (350K) and NdNiO_3 (16.3 GPa) have the same number of peaks and look very similar. To come back to the spectrum of NdNiO_3 at 884 K we observe the same band at approximately the same frequency as LaNiO_3 . Since PrNiO_3 enters the rhombohedral phase at 770 K, we can assume that NdNiO_3 at 884 K is close to the structural phase transition or has already undergone it.

4.7 Conclusion

In conclusion, we measured the first ever reported high-quality nickelate RNiO_3 single crystals with $\text{R} = \text{Y, Ho, Dy, Eu, Sm}$ and Nd using Raman spectroscopy. We measured the crystals at low temperature in the insulating antiferromagnetic phase, but we used also the modulation of the laser power to achieve temperatures as high as the melting point of the sample and extracted directly the temperature of the samples from the Stokes/anti-Stokes ratio of the Raman spectrum. In the metallic phase, we observed very broad modes due to the superposition of several phonons close in energy that are further broadened by the electron-phonon interaction. The metal insulator transition is characterized by a strong suppression of the Raman continuum as well as a significant blueshift and narrowing of all modes, among other things, due to the vanishing of electron-phonon coupling. A slight decrease of the Raman continuum is also observable when going from the paramagnetic to the antiferromagnetic order. Below the Neel temperature, we observed the appearance of the magnetic resonance and a large number of additional phonons. These additional vibrational modes are evidence for a clear centrosymmetry breaking, as all dipole active phonons are simultaneously Raman active. Indeed, the electric fields (polarization) induced by the electronic charge displacements and imposed by the magnetic order act as a force on the ions, deforming the lattice and pushing the

Ni-ions away from their centrosymmetric positions. The space group is not $P2_1/c$ anymore, but $P2_a2_1$ if the magnetic order is S and N-type, and $P2_ac$ if the magnetic order is T-type. The spontaneous polarization occurring alongside with the magnetic order makes nickelates $RNiO_3$ type-II multiferroics. Finally, we observe the pressure induced insulator-metal transition of $SmNiO_3$ single crystal as well as the orthorhombic-rhombohedral phase transition of $NdNiO_3$.

Remerciements

J'aimerais adresser tout d'abord de chaleureux remerciements à Dirk qui m'a offert le privilège d'effectuer cette thèse et qui m'a partagé l'expérience scientifique de toute une vie avec une approche à la fois rigoureuse et humaine. Ce sont de nombreuses heures que nous avons passées dans ton bureau à démêler les effets des corrélations tout en recalculant ces satanées conversions SI en CGS. Nos discussions se sont finalement toujours terminées sur le manque de piste cyclable à Genève ou sur la meilleure manière d'attraper une grenouille lorsque le verre est à moitié plein. Je m'en souviendrai.

Mes plus sincères remerciements s'adresse ensuite à Jérémie qui a été pour moi à la fois un mentor, un ami et un garant de l'aboutissement de cette thèse. Tu m'as enseigné ta connaissance quasi absolue de tous nos appareils optiques et de la physique qui s'y rapporte. Tu m'as aussi appris à réfléchir, à accomplir, à grandir. Ton humilité, ta bienveillance et ton altruisme font de toi un individu exceptionnel. En 3 ans, je pense que j'ai passé plus de fois la porte de ton bureau que celle de chez moi, et pourtant on était toujours contents de se voir ! C'est peut-être tout le chocolat qu'on a mangé qui nous a toujours donné le sourire. Et sérieusement, que penses-tu si je continue dans une carrière de linguiste ou d'écrivain ? Peu importe, je sais que tu me soutiendrais.

Je remercie également les membres de mon jury, Antoine Georges, Marisa Medarde et Jean-Marc Triscone, qui auront pris le temps de lire ma thèse et de se plonger dans quatre années de travail résumées en une centaine de pages.

La suite de mes remerciements sont dédiés au membre de mon groupe en commençant par Willem qui a toujours été là pour me donner un coup de main, mais qui aurait peut-être bien aimé qu'on aille un peu plus souvent

Remerciements

à l'Escale. Je te promets que cet été on va planter des choux en faisant la psychanalyse du développement des piments. D'ailleurs, je pense que ta gentillesse et ta vivacité d'esprit te permettront de te réaliser dans n'importe quel avenir professionnel. La complicité et l'affection sont désormais enracinés entre nous : Yeah man.

Mes prochaines phrases sont consacrées à Jean-Marie et Michael qui nous ont malheureusement quittés trop tôt pour pratiquer d'autres activités. Merci Jean-Marie d'avoir toujours été là au bon moment pour m'éviter des bourdes - alors que je transpirais déjà la panique - et de m'avoir régulièrement expliqué des concepts loin d'être évidents. Quant à Michael, artisan de Matlab, merci de m'avoir appris à programmer et à trouver LA virgule qui empêche l'exécution du programme. Sache que tes crêpes et tes cannelés nous ont manqués au point où j'ai dû reprendre la relève pour éviter qu'on meurt de faim.

Merci à Alexey de m'avoir permis d'apprendre à manipuler le cryo-SNOM dont la physique est à la pointe de la recherche actuelle et de m'avoir fait participer à des projets dont j'avais rêvés.

Merci à Nimrod de m'avoir fait découvrir ses appareils "home made" et d'avoir pris du temps pour m'expliquer leur fonctionnement et leur utilité pour mes recherches.

Une grande dédicace également à Francesco, Bastien et Adrien toujours prêts à discuter de physique fondamentale et à prendre un moment pour réfléchir de manière plus globale aux phénomènes qui nous entourent. Je vous solliciterai, désormais, pour une sortie de ski ou un footing matinal et j'espère que nous nous réunirons davantage en dehors de l'uni.

Un grand merci aussi à Siobhan pour ton important travail de relecture et tes commentaires constructifs.

Je remercie pareillement toutes les autres personnes qui étaient présentes à l'institut comme Spiros, pour ton affabilité et ton bon sens ; Lionel le pilier des TPs ; Adrien, pour mon premier voyage au PSI ; Nicolas, pour ta déconade et notre future campagne ; Iris, pour ta vivacité dans notre bureau ; Christophe, pour tes cours passionnants ; Nathalie qui m'a suivi depuis le début de mon bachelor ; Enrico, Céline et Matteo, pour leurs connaissances cristallographiques ; Weiwei, Yixi, Julien, Sylvain, Dragana, Fabienne, Christophe, Pierre, Itzik, Kai.

Mes remerciements se tournent maintenant vers toutes mes amies qui m'ont soutenu et ont pris régulièrement des nouvelles de moi : Roxane, Solène, Sarah, Célié, Katia, Léa. Un grand merci à mes amis Max et Sab qui ont vu l'évolution de mon épuisement et qui m'ont conforté tout en me conseillant de prendre un peu de temps pour moi ; conseil que je n'ai

finalement jamais appliqué. Un big up à mes amis Nénés qui ont réussi de temps en temps à me faire boire une petite bière ou fumer une cigarette pour me détendre un peu tout en écoutant avec patience les récits de mes recherches. Merci à Hervé et Dominique pour ce cadre idilique qu'ils m'offrent depuis mon plus jeune âge à la montagne et qui m'a permis de me lancer dans l'écriture de cette thèse. Mes remerciements aussi à Gael, Alban et Gaby pour leur soutien. Un merci également à mes collègues de la mairie : Magali et Philippe pour leur soutien et leurs huiles essentielles, Renate pour tes encouragements, Jean-Marc, Louise, Jean-Luc et Komla qui m'ont vu disparaître ces derniers mois, mais qui sont restés toujours disponibles.

Finalement, j'aimerais remercier profondément mes parents et ma soeur qui m'ont fait confiance et m'ont soutenu pour que j'accomplisse mon travail consciencieusement et avec détermination jusqu'au bout.

Un grand merci aussi à toi, Manuela, pour ta grande générosité et de m'avoir transmis ce message de soutien afin que je me lance dans cette aventure.

Ces dernières lignes ne pouvaient qu'être destinées à la personne qui a été à mes côtés à chaque instant de cette expérience, qui m'a offert ses encouragements, son écoute, son réconfort, sa motivation, sa douceur, sa sagesse, son indulgence et qui a partagé mes joies comme mes coups durs. Tout cela avec le plus grand dévouement et de manière inconditionnelle ; simplement parce que tu es une femme extraordinaire, pleine de magie et que tu as le coeur sur la main. Tu es la femme la plus merveilleuse du monde et la clef de mon bonheur. Merci d'enseigner chacune de mes journées. Marina, je t'aime.

Bibliography

- [1] N. F. Mott and R. Peierls, “Discussion of the paper by de Boer and Verwey”, *Proceedings of the Physical Society* **49**, 72–73 (1937).
- [2] G. Jonker and J. V. Santen, “Ferromagnetic compounds of manganese with perovskite structure”, *Physica* **16**, 337–349 (1950).
- [3] R. von Helmolt et al., “Giant negative magnetoresistance in perovskitelike $\text{La}_{2/3}\text{Ba}_{1/3}\text{MnO}_x$ ferromagnetic films”, *Phys. Rev. Lett.* **71**, 2331–2333 (1993).
- [4] M. N. Baibich et al., “Giant Magnetoresistance of (001)Fe/(001)Cr Magnetic Superlattices”, *Phys. Rev. Lett.* **61**, 2472–2475 (1988).
- [5] G. Binasch et al., “Enhanced magnetoresistance in layered magnetic structures with antiferromagnetic interlayer exchange”, *Phys. Rev. B* **39**, 4828–4830 (1989).
- [6] J. Fowlie, “Electronic and structural properties of LaNiO_3 -based heterostructures”, PhD thesis (University of Geneva, 2018).
- [7] D. Staedler et al., “Deep UV generation and direct DNA photo-interaction by harmonic nanoparticles in labelled samples”, *Nanoscale* **6**, 2929–2936 (2014).
- [8] H. Xu et al., “High-performance all-solid-state batteries enabled by salt bonding to perovskite in poly(ethylene oxide)”, *Proc. Natl. Acad. Sci. USA* **116**, 18815–18821 (2019).
- [9] C. Kalaiselvi et al., “Importance of Halide Perovskites for next generation solar cells- A Review”, *Materials Letters* **219**, 198–200 (2018).

BIBLIOGRAPHY

- [10] D. Thakur et al., “A Review on Immersion System to increase the efficiency of Solar Panels”, *International Journal of Advanced Research* **4**, 312–325 (2016).
- [11] M. A. Green et al., “Very high efficiency silicon solar cells-science and technology”, *IEEE Transactions on Electron Devices* **46**, 1940–1947 (1999).
- [12] J. Zhao, A. Wang, and M. Green, “24.5% efficiency PERT silicon solar cells on SEH MCZ substrates and cell performance on other SEH CZ and FZ substrates”, *Solar Energy Materials and Solar Cells - SOLAR ENERG MATER SOLAR CELLS* **66**, 27–36 (2001).
- [13] A. Blakers et al., “High Efficiency Silicon Solar Cells”, *Energy Procedia* **33**, 1–10 (2013).
- [14] N. Zin et al., “Continued Development of All-Back-Contact Silicon Wafer Solar Cells at ANU”, *Energy Procedia* **33**, 50–63 (2013).
- [15] J. Y. Kim et al., “High-Efficiency Perovskite Solar Cells”, *Chemical Reviews* **120**, 7867–7918 (2020).
- [16] A. Jena, A. Kulkarni, and T. Miyasaka, “Halide Perovskite Photovoltaics: Background, Status, and Future Prospects”, *Chemical Reviews* **119**, 3036–3103 (2019).
- [17] T. Duong et al., “High Efficiency Perovskite-Silicon Tandem Solar Cells: Effect of Surface Coating versus Bulk Incorporation of 2D Perovskite”, *Advanced Energy Materials* **10**, 1903553 (2020).
- [18] “<https://rethinkresearch.biz/articles/perovskites-poised-to-disrupt-solar-supply-chains-everywhere/>”,
- [19] L. Chang et al., “Band gap tuning of nickelates for photovoltaic applications”, *Journal of Physics D: Applied Physics* **49**, 44LT02 (2016).
- [20] Q. Shang et al., “Enhanced Charge Transport in Conventional Polymer Solar Cells with a Perovskite-Type LaNiO_3 Layer”, *ACS Applied Materials and Interfaces* **12**, 13051–13060 (2020).
- [21] L. Chang et al., “Tuning Photovoltaic Performance of Perovskite Nickelates Heterostructures by Changing the A-Site Rare-Earth Element”, *ACS Applied Materials and Interfaces* **11**, 16191–16197 (2019).
- [22] G. Amow and S. Skinner, “Recent developments in Ruddlesden-Popper nickelate systems for solid oxide fuel cell cathodes”, *Journal of Solid State Electrochemistry* **10**, 538–546 (2006).
- [23] C. Ferchaud et al., “High performance praseodymium nickelate oxide cathode for low temperature solid oxide fuel cell”, *Journal of Power Sources* **196**, 1872–1879 (2011).

- [24] M. Garali et al., “Synthesis, characterization and electrochemical properties of $\text{La}_{2-x}\text{Eu}_x\text{NiO}_{4+\delta}$ Ruddlesden-Popper-type layered nickelates as cathode materials for SOFC applications”, *International Journal of Hydrogen Energy* **44**, 11020–11032 (2019).
- [25] A. Tarutin et al., “Recent advances in layered $\text{Ln}_2\text{NiO}_{4+\delta}$ nickelates: fundamentals and prospects of their applications in protonic ceramic fuel and electrolysis cells”, *Journal of Materials Chemistry A* **9**, 154–195 (2021).
- [26] J. Chen et al., “A d-Band Electron Correlated Thermoelectric Thermistor Established in Metastable Perovskite Family of Rare-Earth Nickelates”, *ACS Applied Materials and Interfaces* **11**, 34128–34134 (2019).
- [27] X.-Q. Liu et al., “Giant Dielectric Response in Two Dimensional Charge-Ordered Nickelate Ceramics”, *Journal of Applied Physics* **104**, 054114 (2008).
- [28] E.-J. Guo et al., “Oxygen Diode Formed in Nickelate Heterostructures by Chemical Potential Mismatch”, *Advanced Materials* **30**, 1705904 (2018).
- [29] C. Dominguez et al., “Length-scales of interfacial coupling between metal-insulator phases in oxides”, **19**, 1182–1187 (2020).
- [30] C. Jikun et al., “Overcoming synthetic metastabilities and revealing metal-to-insulator transition and thermistor bi-functionalities for d-band correlation perovskite nickelates”, *Materials Horizons* **6**, 788–795 (2019).
- [31] J. Park et al., “Rapid Fabrication of Chemical Solution-Deposited Lanthanum Nickelate Thin Films via Intense Pulsed-Light Process”, *Coatings* **9**, 372 (2019).
- [32] M. Li et al., “Strontium-doped Lanthanum Iron Nickelate Oxide as Highly Efficient Electrocatalysts for Oxygen Evolution Reaction”, *Journal of Colloid and Interface Science* **553**, 813–819 (2019).
- [33] L. A. HASKIN et al., “Relative and Absolute Terrestrial Abundances of the Rare Earths”, in *Origin and distribution of the elements*, edited by L. AHRENS, International Series of Monographs in Earth Sciences (Pergamon, 1968), pp. 889–912.
- [34] P. Henderson, “Chapter 1 - General Geochemical Properties and Abundances of the Rare Earth Elements”, in *Rare earth element geochemistry*, Vol. 2, Developments in Geochemistry (Elsevier, 1984), pp. 1–32.

BIBLIOGRAPHY

- [35] G. Demazeau et al., “Sur une serie de composes oxygenes du nickel trivalent derives de la perovskite”, *Journal of Solid State Chemistry* **3**, 582–589 (1971).
- [36] J. L. Garcia-Munoz et al., “Neutron-diffraction study of RNiO_3 ($\text{R}=\text{La,Pr,Nd,Sm}$): Electronically induced structural changes across the metal-insulator transition”, *Physical Review B* **46**, 4414–4425 (1992).
- [37] J. A. Alonso et al., “Metal-Insulator Transitions, Structural and Microstructural Evolution of RNiO_3 ($\text{R} = \text{Sm, Eu, Gd, Dy, Ho, Y}$) Perovskites: Evidence for Room-Temperature Charge Disproportionation in Monoclinic HoNiO_3 and YNiO_3 ”, *Journal of the American Chemical Society* **121**, 4754–4762 (1999).
- [38] J. A. Alonso et al., “Room-temperature monoclinic distortion due to charge disproportionation in RNiO_3 perovskites with small rare-earth cations ($\text{R} = \text{Ho, Y, Er, Tm, Yb, and Lu}$): A neutron diffraction study”, *Physical Review B* **61**, 1756–1763 (2000).
- [39] J. A. Alonso et al., “High-temperature structural evolution of RNiO_3 ($\text{R} = \text{Ho, Y, Er, Lu}$) perovskites: Charge disproportionation and electronic localization”, *Physical Review B* **64**, 094102 (2001).
- [40] C. Piamonteze et al., “Short-range charge order in RNiO_3 perovskites ($\text{R}=\text{Pr, Nd, Eu, Y}$) probed by x-ray-absorption spectroscopy”, *Physical Review B* **71**, 012104 (2005).
- [41] J. Alonso et al., “On the evolution of the DyNiO_3 perovskite across the metal-insulator transition through neutron diffraction and Mossbauer spectroscopy studies”, *Dalton transactions (Cambridge, England : 2003)* **16**, 6584–6592 (2009).
- [42] J. L. Garcia-Munoz, J. Rodriguez-Carvajal, and P. Lacorre, “Sudden Appearance of an Unusual Spin Density Wave At the Metal-Insulator Transition in the Perovskites RNiO_3 ($\text{R} = \text{Pr, Nd}$)”, *Europhysics Letters (EPL)* **20**, 241 (1992).
- [43] J. Rodriguez-Carvajal et al., “Neutron-diffraction study of the magnetic and orbital ordering in $^{154}\text{SmNiO}_3$ and $^{153}\text{EuNiO}_3$ ”, *Phys. Rev. B* **57**, 456 (1998).
- [44] M. L. Medarde, “Structural, magnetic and electronic properties of perovskites ($\text{R} = \text{rare earth}$)”, *Journal of Physics: Condensed Matter* **9**, 1679 (1997).
- [45] N. A. Hill, “Why Are There so Few Magnetic Ferroelectrics”, *The Journal of Physical Chemistry B* **104**, 6694–6709 (2000).
- [46] J. van den Brink and D. I. Khomskii, “Multiferroicity due to charge ordering”, *Journal of Physics: Condensed Matter* **20**, 434217 (2008).

-
- [47] G. Catalan, “Progress in perovskite nickelate research”, *Phase Transitions* **81**, 729–749 (2008).
- [48] G. Giovannetti et al., “Multiferroicity in Rare-Earth Nickelates RNiO_3 ”, *Phys. Rev. Letters* **103**, 156401 (2009).
- [49] X. F. Hao et al., “Structural and ferroelectric transitions in magnetic nickelate PbNiO_3 ”, *New Journal of Physics* **16**, 015030 (2014).
- [50] C. Xin et al., “Electronic, magnetic and ferroelectric properties of multiferroic TlNiO_3 : A first principles study”, *Computational Materials Science* **82**, 191–196 (2014).
- [51] J. M. Perez-Mato et al., “Symmetry conditions for type II multiferroicity in commensurate magnetic structures”, *Journal of Physics: Condensed Matter* **28**, 286001 (2016).
- [52] D. I. Khomskii, “Coupled electric and magnetism in solids: multiferroics and beyond”, in, *Series in Materials Science and Engineering* (Taylor and Francis, CRC Press, 2017) Chap. 1, pp. 1–31.
- [53] C. Xin et al., “Insight into the effect of high pressure on multiferroic properties of TmNiO_3 ”, *Journal of Alloys and Compounds* **815**, 152351 (2020).
- [54] D. G. Ouellette et al., “Optical conductivity of LaNiO_3 : Coherent transport and correlation driven mass enhancement”, *Phys. Rev. B* **82**, 165112 (2010).
- [55] J. Liu et al., “Strain-mediated metal-insulator transition in epitaxial ultrathin films of NdNiO_3 ”, *Applied Physics Letters* **96**, 233110 (2010).
- [56] M. K. Stewart et al., “Optical study of strained ultrathin films of strongly correlated LaNiO_3 ”, *Phys. Rev. B* **83**, 075125 (2011).
- [57] Y. Kumar et al., “Strain dependent stabilization of metallic paramagnetic state in epitaxial NdNiO_3 thin films”, *Applied Physics Letters* **101**, 132101 (2012).
- [58] R. Scherwitzl, “Metal-insulator transitions in nickelate heterostructures”, PhD thesis (University of Geneva, 2012).
- [59] J. Liu et al., “Heterointerface engineered electronic and magnetic phases of NdNiO_3 thin films”, *Nature communications* **4**, 2714 (2013).
- [60] P. Xiang et al., “Strain controlled metal-insulator transition in epitaxial NdNiO_3 thin films”, *Journal of Applied Physics* **114**, 243713–243713 (2013).
- [61] O. E. Peil, M. Ferrero, and A. Georges, “Orbital polarization in strained LaNiO_3 : Structural distortions and correlation effects”, *Phys. Rev. B* **90**, 045128 (2014).

BIBLIOGRAPHY

- [62] J. Ruppen et al., “Optical spectroscopy and the nature of the insulating state of rare-earth nickelates”, *Phys. Rev. B* **92**, 155145 (2015).
- [63] E. Mikheev et al., “Tuning bad metal and non-Fermi liquid behavior in a Mott material: Rare-earth nickelate thin films”, *Science Advances* **1**, 10 (2015).
- [64] J. Zhang et al., “Key role of lattice symmetry in the metal-insulator transition of NdNiO₃ films”, *Scientific reports* **6**, 23652 (2016).
- [65] L. Wang et al., “Competition between strain and dimensionality effects on the electronic phase transitions in NdNiO₃ films”, *Scientific Reports* **5**, 18707 (2015).
- [66] S. Catalano et al., “Rare-Earth Nickelates RNiO₃: Thin films and heterostructures”, *Reports on Progress in Physics* **81**, 046501 (2017).
- [67] B. Torriss, J. Margot, and M. Chaker, “Metal-Insulator Transition of strained SmNiO₃ Thin Films: Structural, Electrical and Optical Properties”, *Scientific Reports* **7**, 40915 (2017).
- [68] J. Fowlie et al., “Conductivity and Local Structure of LaNiO₃ Thin Films”, *Advanced Materials* **29**, 1605197 (2017).
- [69] M. Chandra et al., “Induced metal-insulator transition and temperature independent charge transport in NdNiO_{3-δ} thin films”, **696**, 423–427 (2017).
- [70] J. Ruppen et al., “Impact of antiferromagnetism on the optical properties of rare earth nickelates”, *Physical Review B* **96**, 045120 (2017).
- [71] E. Cappelli et al., “A laser-ARPES study of LaNiO₃ thin films grown by sputter deposition”, *APL Materials* **8**, 051102 (2020).
- [72] B. Berini et al., “Reversible Phase Transformation of LaNiO_{3-x} thin films studied in-situ by spectroscopic ellipsometry”, *Physical Review B* **76**, 205417 (2007).
- [73] E. Breckenfeld et al., “Effects of Nonequilibrium Growth, Nonstoichiometry, and Film Orientation on the Metal-to-Insulator Transition in NdNiO₃ Thin Films”, *ACS Applied Materials and Interfaces* **6**, 22436–22444 (2014).
- [74] L. Wang et al., “Oxygen Vacancy Induced Room-Temperature Metal-Insulator Transition in Nickelate Films and Its Potential Application in Photovoltaics”, *ACS Applied Materials and Interfaces* **8**, 9769–9776 (2016).
- [75] A. S. Disa et al., “Phase diagram of compressively strained nickelate thin films”, *APL Materials* **1**, 032110 (2013).

- [76] D. Li et al., “Superconductivity in an infinite-layer nickelate”, *Nature* **572**, 624–627 (2019).
- [77] E. Talantsev, “Classifying superconductivity in an infinite-layer nickelate $\text{Nd}_{0.8}\text{Sr}_{0.2}\text{NiO}_2$ ”, *Results in Physics* **17**, 103118 (2020).
- [78] J. Chaloupka and G. Khaliullin, “Orbital Order and Possible Superconductivity in LaNiO_3 / LaMO_3 Superlattices”, *Physical review letters* **100**, 016404 (2008).
- [79] P. Hansmann et al., “Turning a Nickelate Fermi Surface into a Cuprate-like One through Heterostructuring”, *Physical review letters* **103**, 016401 (2009).
- [80] T. Saito et al., “Monoclinic distortion in the insulating phase of PrNiO_3 ”, *Physica B: Condensed Matter* **329-333**, 866–867 (2003).
- [81] J. A. Alonso et al., “Crystal growth of NdNiO_3 perovskite under high oxygen pressure”, *Journal of Physics: Condensed Matter* **16**, S1277 (2004).
- [82] I. Ardizzone et al., “Optical properties of LaNiO_3 films tuned from compressive to tensile strain”, *Phys. Rev. B* **102**, 155148 (2020).
- [83] I. Ardizzone et al., “Raman spectroscopic evidence for multiferroicity in rare earth nickelate single crystals”, *Phys. Rev. Research* **3**, 033007 (2021).
- [84] H. Rietveld, “A Profile Refinement Method for Nuclear and Magnetic Structures”, *Journal of Applied Crystallography* **2**, 65–71 (1969).
- [85] J. A. Alonso et al., “High-Pressure Preparation, Crystal Structure, Magnetic Properties, and Phase Transitions in GdNiO_3 and DyNiO_3 Perovskites”, *Chemistry of Materials* **11**, 2463–2469 (1999).
- [86] F. P. de la Cruz et al., “Possible common ground for the metal-insulator phase transition in the rare-earth nickelates RNiO_3 (R= Eu, Ho, Y)”, *Physical Review B* **66**, 153104 (2002).
- [87] J. K. Vassiliou et al., “Synthesis and properties of NdNiO_3 prepared by low-temperature methods”, *Journal of Solid State Chemistry* **81**, 208–216 (1989).
- [88] X. Granados et al., “Metallic state and the metal-insulator transition of NdNiO_3 ”, *Phys. Rev. B* **48**, 11666–11672 (1993).
- [89] P. Canfield et al., “Extraordinary pressure dependence of the metal-to-insulator transition in the charge-transfer compounds NdNiO_3 and PrNiO_3 ”, *Phys. Rev. B* **47**, 12357–12360 (1993).
- [90] M. A. Mroginiski et al., “Metal-insulator phase transitions of SmNiO_3 and PrNiO_3 : Electrons in a polaronic medium”, *Physical Review B* **60**, 5304–5311 (1999).

BIBLIOGRAPHY

- [91] J.-S. Zhou, J. Goodenough, and B. Dabrowski, “Pressure-Induced Non-Fermi-Liquid Behavior of PrNiO_3 ”, *Physical review letters* **94**, 226602 (2005).
- [92] J.-G. Cheng et al., “Pressure dependence of metal-insulator transition in perovskites RNiO_3 (R= Eu, Y, Lu)”, *Phys. Rev. B* **82**, 085107 (2010).
- [93] N. E. Massa et al., “Reflectivity, transmission, and photoinduced infrared spectra of NdNiO_3 ”, *Phys. Rev. B* **56**, 986–989 (1997).
- [94] N. E. Massa et al., “Infrared reflectivity of the solid solutions $\text{LaNi}_{1-x}\text{Fe}_x\text{O}_3$ ”, *Physical Review B* **56**, 10178–10191 (1997).
- [95] L. Chen et al., “Edge Effect on Crack Patterns in Thermally Sprayed Ceramic Splats”, *Journal of Thermal Spray Technology* **26**, 302–314 (2016).
- [96] S. J. May et al., “Quantifying octahedral rotations in strained perovskite oxide films”, *Phys. Rev. B* **82**, 014110 (2010).
- [97] D. Preziosi et al., “Reproducibility and off-stoichiometry issues in nickelate thin films grown by pulsed laser deposition”, *AIP Advances* **7**, 015210 (2017).
- [98] Y. Kumar, R. J. Choudhary, and R. Kumar, “Disappearance of metal-insulator transition in $\text{NdNiO}_3/\text{LaAlO}_3$ films by ion irradiation controlled stress”, *Journal of Applied Physics* **120**, 115306 (2016).
- [99] E. Sakai et al., “Gradual localization of Ni 3d states in LaNiO_3 ultrathin films induced by dimensional crossover”, *Physical Review B* **87**, 075132 (2013).
- [100] E. Sakai et al., “Bandwidth-controlled metal-insulator transition in epitaxial PrNiO_3 ultrathin films induced by dimensional crossover”, *Applied Physics Letters* **104**, 171609 (2014).
- [101] R. Mortimer, M. T. Weller, and P. Henry, “Pressure-induced change of electronic state in samarium nickelate, SmNiO_3 , around 1.1 GPa: an infrared spectroscopic study”, *Physica B: Condensed Matter* **271**, 173–179 (1999).
- [102] J. L. Garcia-Munoz et al., “Pressure-induced melting of charge-order in the self-doped Mott insulator YNiO_3 ”, *Phys. Rev. B* **69**, 094106 (2004).
- [103] R. Lengsdorf et al., “The observation of the insulator-metal transition in EuNiO_3 under high pressure”, *Journal of Physics: Condensed Matter* **16**, 3355 (2004).
- [104] M. Amboage et al., “High pressure structural study of SmNiO_3 ”, *Journal of Physics: Condensed Matter* **17**, S783 (2005).

- [105] N. Massa et al., “Temperature and high-pressure dependent X-ray absorption of SmNiO_3 at the Ni K- and Sm L3- edges”, *Materials Research Express* **2**, 126301 (2015).
- [106] H. Kobayashi et al., “Pressure-induced unusual metallic state in EuNiO_3 ”, *Physical Review B* **91**, 195148 (2015).
- [107] M. Medarde et al., “High-Pressure Neutron-Diffraction Study of the Metallization Process in PrNiO_3 ”, *Physical review. B, Condensed matter* **52**, 9248–9258 (1995).
- [108] X. Obradors et al., “Pressure dependence of the metal-insulator transition in the charge-transfer oxides RNiO_3 ($\text{R}=\text{Pr}, \text{Nd}, \text{Nd}_{0.7}\text{La}_{0.3}$ ”, *Phys. Rev. B* **47**, 12353–12356 (1993).
- [109] J.-S. Zhou et al., “Probing the metal-insulator transition in Ni(III)-oxide perovskites”, *Phys. Rev. B* **61**, 4401–4404 (2000).
- [110] J.-S. Zhou, J. Goodenough, and B. Dabrowski, “Exchange Interaction in the Insulating Phase of RNiO_3 ”, *Physical review letters* **95**, 127204 (2005).
- [111] J.-S. Zhou, J. B. Goodenough, and B. Dabrowski, “Structure anomaly and electronic transition in RNiO_3 ($\text{R}=\text{La}, \text{Pr}, \text{Gd}$)” *Phys. Rev. B* **70**, 081102 (2004).
- [112] M. Medarde et al., “Pressure-induced orthorhombic-rhombohedral phase transition in NdNiO_3 ”, *Physica B: Condensed Matter* **234-236**, 15–17 (1997).
- [113] D. B. Litvin, *Magnetic Group Tables: 1-, 2- and 3-Dimensional Magnetic Subperiodic Groups and Magnetic Space Groups*, Vol. 1–2 (International Union of Crystallography, 2013).
- [114] C. Collignon et al., “Metallicity and Superconductivity in Doped Strontium Titanate”, *Annual Review of Condensed Matter Physics* **10**, 25–44 (2019).
- [115] T. Huang et al., “High-temperature crystal structures of orthorhombic and rhombohedral PrNiO_3 ”, *Materials Research Bulletin* **25**, 1091–1098 (1990).
- [116] C. Sara, “Electronic properties of NdNiO_3 and SmNiO_3 thin films”, PhD thesis (2017).
- [117] A. Herklotz and K. Dorr, “Characterization of tetragonal phases of SrRuO_3 under epitaxial strain by density functional theory”, *The European Physical Journal B* **88**, 60 (2015).
- [118] T. Hahn, *International Tables for Crystallography Volume A: Space-group symmetry*, Vol. A (International Union of Crystallography, 2002).

BIBLIOGRAPHY

- [119] M. Medarde, M. Fernandez-Diaz, and P. Lacorre, “Long-range charge order in the low-temperature insulating phase of PrNiO_3 ”, *Phys. Rev. B* **78**, 212101 (2008).
- [120] J. A. Alonso et al., “Charge Disproportionation in RNiO_3 Perovskites: Simultaneous Metal-Insulator and Structural Transition in YNiO_3 ”, *Phys. Rev. Lett.* **82**, 3871–3874 (1999).
- [121] T. Mizokawa, D. I. Khomskii, and G. A. Sawatzky, “Spin and charge ordering in self-doped Mott insulators”, *Phys. Rev. B* **61**, 11263–11266 (2000).
- [122] H. Park, A. J. Millis, and C. A. Marianetti, “Site-Selective Mott Transition in Rare-Earth-Element Nickelates”, *Phys. Rev. Lett.* **109**, 156402 (2012).
- [123] B. Lau and A. J. Millis, “Theory of the Magnetic and Metal-Insulator Transitions in RNiO_3 Bulk and Layered Structures”, *Phys. Rev. Lett.* **110**, 126404 (2013).
- [124] S. Johnston et al., “Charge Disproportionation without Charge Transfer in the Rare-Earth-Element Nickelates as a Possible Mechanism for the Metal-Insulator Transition”, *Phys. Rev. Lett.* **112**, 106404 (2014).
- [125] A. Subedi, O. E. Peil, and A. Georges, “Low-energy description of the metal-insulator transition in the rare-earth nickelates”, *Phys. Rev. B* **91**, 075128 (2015).
- [126] N. Hamada, “Electronic band structure of LaNiO_3 ”, *Journal of Physics and Chemistry of Solids* **54**, 1157–1160 (1993).
- [127] X. Xu et al., “Charge Disproportionation in YNiO_3 Perovskite: An ab Initio Calculation”, *Journal of Physical Chemistry B - J PHYS CHEM B* **108**, 1165–1167 (2004).
- [128] J. He and C. Franchini, “Screened hybrid functional applied to $3d^0 \rightarrow 3d^8$ transition-metal perovskites LaMO_3 ($M = \text{Sc-Cu}$): Influence of the exchange mixing parameter on the structural, electronic, and magnetic properties”, *Physical Review B* **86**, 235117 (2012).
- [129] E. A. Nowadnick et al., “Quantifying electronic correlation strength in a complex oxide: A combined DMFT and ARPES study of LaNiO_3 ”, *Phys. Rev. B* **92**, 245109 (2015).
- [130] P. Seth et al., “Renormalization of effective interactions in a negative charge-transfer insulator”, *Physical Review B* **96**, 205139 (2017).
- [131] A. Subedi, “Breathing distortions in the metallic, antiferromagnetic phase of LaNiO_3 ”, *SciPost Physics* **5**, 020 (2017).

- [132] S. Wang et al., “Tuning the magnetic properties of DyNiO₃ by high-pressures”, *Computational Materials Science* **146**, 213–219 (2018).
- [133] J. Bieder et al., “Optical spectra of rare-earth nickelates”, *Physical Review B* **102**, 081111 (2020).
- [134] D. D. Sarma, N. Shanthi, and P. Mahadevan, “Electronic structure and the metal-insulator transition in LnNiO₃ (Ln=La, Pr, Nd, Sm and Ho): bandstructure results”, *Journal of Physics: Condensed Matter* **6**, 10467 (1994).
- [135] H. Park, A. Millis, and C. Marianetti, “Total energy calculations using DFT+DMFT: Computing the pressure phase diagram of the rare earth nickelates”, *Physical Review B* **89**, 245133 (2014).
- [136] O. Peil et al., “Mechanism and control parameters of the coupled structural and metal-insulator transition in nickelates”, *Physical Review B* **99**, 245127 (2019).
- [137] G. A. Sawatzky and J. W. Allen, “Magnitude and Origin of the Band Gap in NiO”, *Phys. Rev. Lett.* **53**, 2339–2342 (1984).
- [138] P. G. Etchegoin, E. C. Le Ru, and M. Meyer, “An analytic model for the optical properties of gold”, *The Journal of Chemical Physics* **125**, 164705 (2006).
- [139] M. Dressel and M. Scheffler, “Verifying the Drude response”, *Annalen der Physik* **15**, 535–544 (2006).
- [140] W. Gotze and P. Wolfle, “Homogeneous Dynamical Conductivity of Simple Metals”, *Phys. Rev. B* **6**, 1226–1238 (1972).
- [141] C. Berthod et al., “Non-Drude universal scaling laws for the optical response of local Fermi liquids”, *Physical Review B* **87**, 115109 (2012).
- [142] R. Scherwitzl et al., “Metal-Insulator Transition in Ultrathin LaNiO₃ Films”, *Phys. Rev. Lett.* **106**, 246403 (2011).
- [143] I. I. Mazin et al., “Charge Ordering as Alternative to Jahn-Teller Distortion”, *Phys. Rev. Lett.* **98**, 176406 (2007).
- [144] J. Zaanen, G. A. Sawatzky, and J. W. Allen, “Band gaps and electronic structure of transition-metal compounds”, *Phys. Rev. Lett.* **55**, 418–421 (1985).
- [145] T. Mizokawa et al., “Origin of the band gap in the negative charge-transfer-energy compound NaCuO₂”, *Phys. Rev. Lett.* **67**, 1638–1641 (1991).
- [146] V. Bisogni et al., “Ground state oxygen holes and the metal-insulator transition in the negative charge transfer rare-earth nickelates”, *Nature Communications* **7**, 13017 (2016).

BIBLIOGRAPHY

- [147] U. Staub et al., “Direct Observation of Charge Order in an Epitaxial NdNiO₃ Film”, *Physical review letters* **88**, 126402 (2002).
- [148] A. Caytuero et al., “Evidence for charge disproportionation in monoclinic EuNiO₃ from Fe Mossbauer spectroscopy”, *Phys. Rev. B* **76**, 193105 (2007).
- [149] J. Shamblin et al., “Experimental evidence for bipolaron condensation as a mechanism for the metal-insulator transition in rare-earth nickelates”, *Nature Communications* **9**, 86 (2018).
- [150] H. K. Yoo et al., “Latent instabilities in metallic LaNiO₃ films by strain control of Fermi-surface topology”, *Sci. Rep.* **5**, 8746 (2015).
- [151] D. N. Basov et al., “Electrodynamics of correlated electron materials”, *Rev. Mod. Phys.* **83**, 471–541 (2011).
- [152] J. B. Torrance et al., “Systematic study of insulator-metal transitions in perovskites RNiO₃ (R = Pr, Nd, Sm, Eu) due to closing of charge-transfer gap”, *Phys. Rev. B* **45**, 8209–8212 (1992).
- [153] J. L. Garcia-Munoz, J. Rodriguez-Carvajal, and P. Lacorre, “Neutron-diffraction study of the magnetic ordering in the insulating regime of the perovskites RNiO₃ (R=Pr and Nd)”, *Phys. Rev. B* **50**, 978–992 (1994).
- [154] M. T. Fernandez-Diaz et al., “Magnetic structure of the HoNiO₃ perovskite”, *Phys. Rev. B* **64**, 144417 (2001).
- [155] A. Munoz et al., “On the magnetic structure of DyNiO₃”, *journal of Solid State Chemistry* **182**, 1982–1989 (2009).
- [156] H. Guo et al., “Antiferromagnetic correlations in the metallic strongly correlated transition metal oxide LaNiO₃”, *Nat. Commun.* **9**, 43 (2018).
- [157] J. A. Alonso et al., “A structural and magnetic study of the defect perovskite LaNiO_{2.5} from high-resolution neutron diffraction data”, *J. Phys. Condens. Matter* **9**, 6417 (1997).
- [158] B.-X. Wang et al., “Antiferromagnetic defect structure in LaNiO_{3-δ} single crystals”, *Phys. Rev. Materials* **2**, 064404 (2018).
- [159] V. Scagnoli et al., “Induced noncollinear magnetic order of Nd³⁺ in NdNiO₃ observed by resonant soft x-ray diffraction”, *Phys. Rev. B* **77**, 115138 (2008).
- [160] D. Meyers et al., “Charge order and antiferromagnetism in epitaxial ultrathin films of EuNiO₃”, *Phys. Rev. B* **92**, 235126 (2015).
- [161] Y. Lu et al., “Site-Selective Probe of Magnetic Excitations in Rare-Earth Nickelates Using Resonant Inelastic X-ray Scattering”, *Phys. Rev. X* **8**, 031014 (2018).

- [162] S.-W. Cheong and M. Mostovoy, “Multiferroics: a magnetic twist for ferroelectricity”, *Nature Materials* **6**, 13–20 (2007).
- [163] L. notes of Dirk van der Marel, “Introduction to Correlated Matter”, <https://dirkvandermarel.ch/enseignement/> (2019).
- [164] D. Paul, “Zur Elektronentheorie der Metalle”, *Annalen der Physik* **306**, 566–613 (1900).
- [165] J. Teyssier et al., “Optical study of electronic structure and electron-phonon coupling in ZrB_{12} ”, *Phys. Rev. B* **75**, 134503 (2007).
- [166] E. van Heumen et al., “Optical determination of the relation between the electron-boson coupling function and the critical temperature in high- T_c cuprates”, *Phys. Rev. B* **79**, 184512 (2009).
- [167] M. Nakajima et al., “Evolution of the optical spectrum with doping in $\text{Ba}(\text{Fe}_{1-x}\text{Co}_x)_2\text{As}_2$ ”, *Phys. Rev. B* **81**, 104528 (2010).
- [168] B. Cheng et al., “Electronic properties of 3d transitional metal pnictides: A comparative study by optical spectroscopy”, *Phys. Rev. B* **86**, 134503 (2012).
- [169] A. Kuzmenko, “Kramers-Kronig constrained variational analysis of optical spectra”, *Rev. Sci. Instrum.* **76**, 083108 (2005).
- [170] A. Fresnel, “Premier mémoire sur la double réfraction”, *OFC*, 261–308 (1821).
- [171] M. Dressel and G. Gruner, *Electrodynamics of Solids: Optical Properties of Electrons in Matter* (Cambridge University Press, 2002).
- [172] R. Julien, “The color of electronic correlation in rare-earth nickelates”, PhD thesis (Apr. 2018).
- [173] H. Fujiwara, *Spectroscopic Ellipsometry: Principles and Applications* (Wiley, 2007).
- [174] K. Sreedhar et al., “Electronic properties of the metallic perovskite LaNiO_3 : Correlated behavior of 3d electrons”, *Phys. Rev. B* **46**, 6382–6386 (1992).
- [175] J. Son et al., “Low-dimensional Mott material: Transport in ultrathin epitaxial LaNiO_3 films”, *Applied Phys. Lett.* **96**, 062114 (2010).
- [176] A. Tiwari and K. Rajeev, “Effect of oxygen stoichiometry on the electrical resistivity behaviour of $\text{NdNiO}_{3-\delta}$ ”, *Solid State Communications* **109**, 119–124 (1998).
- [177] N. Bachar, “Spin-flip Scattering in Superconducting Granular Aluminum Films”, PhD thesis (2014).
- [178] N. Ievgeniia, “Infrared magneto-optical spectroscopy of boron nitride encapsulated graphene”, PhD thesis (Oct. 2018).

BIBLIOGRAPHY

- [179] C. Berthod et al., “Non-Drude universal scaling laws for the optical response of local Fermi liquids”, *Phys. Rev. B* **87**, 115109 (2013).
- [180] C. Liu et al., “Observation of an antiferromagnetic quantum critical point in high-purity LaNiO_3 ”, *Nature Communications* **11**, 1402 (2020).
- [181] A. M. Glazer, “The classification of tilted octahedra in perovskites”, *Acta Cryst. B* **28**, 3384–3392 (1972).
- [182] J. P. Perdew, K. Burke, and M. Ernzerhof, “Generalized Gradient Approximation Made Simple”, *prl* **77**, 3865–3868 (1996).
- [183] P. E. Blochl, “Projector augmented-wave method”, *Phys. Rev. B* **50**, 17953–17979 (1994).
- [184] G. Kresse and D. Joubert, “From ultrasoft pseudopotentials to the projector augmented-wave method”, *prb* **59**, 1758–1775 (1999).
- [185] G. Kresse and J. Hafner, “Ab initio molecular dynamics for liquid metals”, *prb* **47**, 558–561 (1993).
- [186] G. Kresse and J. Furthmuller, “Efficient iterative schemes for ab initio total-energy calculations using a plane-wave basis set”, *prb* **54**, 11169–11186 (1996).
- [187] B. Amadon et al., “Plane-wave based electronic structure calculations for correlated materials using dynamical mean-field theory and projected local orbitals”, *prb* **77**, 205112 (2008).
- [188] M. Schuler et al., “Charge self-consistent many-body corrections using optimized projected localized orbitals”, *J. Phys. Condens. Matter* **30**, 475901 (2018).
- [189] P. Blaha et al., *WIEN2k, An Augmented Plane Wave + Local Orbitals Program for Calculating Crystal Properties* (K. Schwarz, Techn. Univ. Wien, Austria, 2018).
- [190] M. Aichhorn et al., “TRIQS/DFTTools: A TRIQS application for ab initio calculations of correlated materials”, *Comput. Phys. Commun.* **204**, 200–208 (2016).
- [191] O. Parcollet et al., “TRIQS: A toolbox for research on interacting quantum systems”, *Comput. Phys. Commun.* **196**, 398–415 (2015).
- [192] P. D. C. King et al., “Atomic-scale control of competing electronic phases in ultrathin LaNiO_3 ”, *Nat. Nanotechnol.* **9**, 443–447 (2014).
- [193] X. Deng et al., “Hallmark of strong electronic correlations in LaNiO_3 : Photoemission kink and broadening of fully occupied bands”, *Phys. Rev. B* **85**, 125137 (2012).
- [194] J. Fowlie et al., “Thickness-Dependent Perovskite Octahedral Distortions at Heterointerfaces”, *Nano Letters* **19**, 4188–4194 (2019).

- [195] N. Marzari and D. Vanderbilt, “Maximally localized generalized Wannier functions for composite energy bands”, *Phys. Rev. B* **56**, 12847–12865 (1997).
- [196] I. Souza, N. Marzari, and D. Vanderbilt, “Maximally localized Wannier functions for entangled energy bands”, *Phys. Rev. B* **65**, 035109 (2001).
- [197] G. Pizzi et al., “Wannier90 as a community code: new features and applications”, *J. Phys. Condens. Matter* **32**, 165902 (2019).
- [198] “Online Interactive Fermi Surface Applet”, <https://lnostrain.page.link/applet> ; It will take a few minutes until the application is loaded and built if it has not been used by anyone recently. Once loaded, click on *RUN_ME.ipynb* and follow the instructions therein.
- [199] G. K. Madsen, J. Carrete, and M. J. Verstraete, “BoltzTraP2, a program for interpolating band structures and calculating semi-classical transport coefficients”, *CompAppendixut. Phys. Commun.* **231**, 140–145 (2018).
- [200] S. Catalano et al., “Rare-earth nickelates RNiO₃: thin films and heterostructures”, *Rep. Prog. Phys* **81**, 046501 (2018).
- [201] X. Hao et al., “Structural and ferroelectric transitions in magnetic nickelate PbNiO₃”, *New journal of Physics* **16**, 015030 (2013).
- [202] N. A. Spaldin and R. Ramesh, “Advances in magnetoelectric multiferroics”, *Nature Materials* **18**, 203–212 (2019).
- [203] I. P. Kaminow and T. C. Damen, “Temperature Dependence of the Ferroelectric Mode in KH₂PO₄”, *Phys. Rev. Lett.* **20**, 1105–1108 (1968).
- [204] M. Takesada, M. Itoh, and T. Yagi, “Perfect Softening of the Ferroelectric Mode in the Isotope-Exchanged Strontium Titanate of SrTi¹⁸O₃”, *Phys. Rev. Lett.* **96**, 227602 (2006).
- [205] R. Kajimoto et al., “Unconventional Ferroelectric Transition in the Multiferroic Compound TbMnO₃ Revealed by the Absence of an Anomaly in *c*-Polarized Phonon Dispersion”, *Phys. Rev. Lett.* **102**, 247602 (2009).
- [206] D. V. Efremov, J. van den Brink, and D. I. Khomskii, “Bond centered vs. site-centered charge ordering: ferroelectricity in oxides”, *Physica B: Condensed Matter* **359-361**, Proceedings of the International Conference on Strongly Correlated Electron Systems, 1433–1435 (2005).
- [207] C. Girardot et al., “Raman scattering investigation across the magnetic and metal-insulator transition in rare earth nickelate RNiO₃ (R= Sm, Nd) thin films”, *Phys. Rev. B* **78**, 104101 (2008).

BIBLIOGRAPHY

- [208] M. Zaghrioui et al., “Electron diffraction and Raman scattering evidence of a symmetry breaking at the metal-insulator transition of NdNiO_3 ”, *Phys. Rev. B* **64**, 081102 (2001).
- [209] Y. Klein et al., “ Renio_3 single crystals (re = nd, sm, gd, dy, y, ho, er, lu) grown from molten salts under 2000 bar oxygen-gas pressure”, arXiv:2104.09873 and DOI:10.1021/acs.cgd.1c00474 (2021).
- [210] C. Toulouse, “Materiaux multiferroiques : structure, ordres et couplages. Une etude par spectroscopie Raman”, PhD thesis (2016).
- [211] Y. Gallais, “La diffusion Raman”, <https://docplayer.fr/17072890-La-diffusion-raman-yann-gallais-mpq-universite-paris-diderot.html> (2016).
- [212] S. A. Michael, “Advanced Raman spectroscopy of ultrathin RNiO_3 films”, PhD thesis (2018).
- [213] G. et al., “QUANTUM ESPRESSO: a modular and open-source software project for quantum simulations of materials”, *Journal of Physics: Condensed Matter* **21**, 395502 (2009).
- [214] J. P. Perdew, K. Burke, and M. Ernzerhof, “Generalized Gradient Approximation Made Simple”, *Phys. Rev. Lett.* **77**, 3865–3868 (1996).
- [215] J. L. Garcia-Munoz, J. Rodriguez-Carvajal, and P. Lacorre, “Neutron-diffraction study of the magnetic ordering in the insulating regime of the perovskites RNiO_3 (R =Pr and Nd)”, *Phys. Rev. B* **50**, 978–992 (1994).
- [216] D. J. Gawryluk et al., “Distortion mode anomalies in bulk PrNiO_3 : Illustrating the potential of symmetry-adapted distortion mode analysis for the study of phase transitions”, *Phys. Rev. B* **100**, 205137 (2019).
- [217] N. Mironova-Ulmane et al., “Polarisation dependent raman study of single-crystal nickel oxide”, *Central European Journal of Physics* **9**, 1096–1099 (2011).
- [218] N. Dilawar et al., “A raman spectroscopic study of c-type rare earth sesquioxides”, *Materials Characterization* **59**, 462–467 (2008).
- [219] M. Tran, “Possible phase transitions probed by infrared spectroscopy under high pressure: BiTeI and $\text{Li}_{0.9}\text{Mo}_6\text{O}_{17}$ ”, PhD thesis (2014).